# Structure-Function Analysis of Motor Proteins: Insights from Conventional and Unconventional Myosins

A Thesis

SUBMITTED TO THE FACULTY OF

UNIVERSITY OF MINNESOTA

BY

Karl J. Petersen

IN PARTIAL FULFILLMENT OF THE REQUIREMENTS

FOR THE DEGREE OF

DOCTOR OF PHILOSOPHY

Margaret A. Titus, Advisor

David D. Thomas, Co-Advisor

December 2016

# Acknowledgements

This thesis would not exist without the patient support of my advisors, ***Meg Titus*** and ***Dave Thomas.*** Any shortcomings are my own. Collaborators ***Holly Goodson, Anne Houdusse***, and ***Gant Luxton*** also provided invaluable training and support.

I am also grateful for essential services provided by departmental staff: ***Sarah Blakely Anderson, Octavian Cornea, Sarah Dittrich, Karen Hawkinson***, ***Michelle Lewis, Mary Muwahid, Laurie O'Neill, Darlene Toedter,*** with apologies to others not listed.

Thanks to friends and colleagues at the University of Minnesota: ***Ashley Arthur, Kelly Bower, Brett Colson, Sinziana Cornea, Chi Meng Fong, Greg Gillispie, Piyali Guhathakurta, Tejas Gupte, Tom Hays, Norma Jiménez Ramírez, Dawn Lowe, Allison MacLean, Santiago Martínez Cifuentes, Jared Matzke, Megan McCarthy, Joachim Mueller, Joe Muretta, Kurt Peterson, Mary Porter, Ewa Prochniewicz, Mike Ritt, Cosmo Saunders, Shiv Sivaramakrishnan, Ruth Sommese, Doug Tritschler, Brian Woolums.***

# Abstract

Myosin motor proteins play fundamental roles in a multitude of cellular processes. Myosin generates force on cytoskeletal actin filaments to control cell shape, most dramatically during cytokinesis, and has a conserved role in defining cell polarity. Myosin contracts the actin cytoskeleton, ensuring prompt turnover of cellular adhesion sites, retracting the cell body during migration and development, and contracting muscle among diverse other functions. How myosins work, and why force generation is essential for their function, is in many cases an open question.

Chapter 2 presents a structure-function analysis of the amoebozoan myosin 7 (DdMyo7) in live *Dictyostelium discoideum* cells. DdMyo7 bears structural resemblance to human Myosin 7 (a protein involved in maintenance of the retina, stereocilia of the ear, and gut microvilli) but has functional similarity to human Myosin 10, a regulator of cell adhesion that is also essential in formation of actin-based structures called filopodia. Phylogenetic analysis of these related proteins shows that DdMyo7 is not directly related to any human myosin but rather represents a molecular ancestor of several vertebrate myosins (Myo7, Myo10 and Myo15). Functional analysis focused on rescue of *myo7*$^{-}$ cells. The two MyTH4-FERM domains were fully redundant in rescuing formation of filopodia. A conserved Myo7 regulatory motif in the C-terminal FERM domain was found to stimulate filopodia formation when mutated, establishing DdMyo7 as a filopodial motor with features of Myo7 and Myo10. A molecular chimera of DdMyo7 motor/lever arm region fused to the MF domain of human Myo10 partially rescued filopodia formation,

suggesting the MF domain plays a similar role in filopodia in divergent organisms.

Structural information must be combined with physiological data to understand the mechanism of myosin motor function. Structural studies have long focused on conventional myosin 2 as a model due to ease of protein expression and purification. This approach has yielded considerable data regarding the static structures and *in vitro* kinetics of the myosin mechanochemical cycle; however, high-resolution methods to observe the dynamics of myosin activation in cells have been lacking. Chapter 4 introduces methods and instrumentation for rapid, precise measurement of fluorescence lifetime. This is a necessary step toward Myo2-based live cell FRET sensors described in Chapter 5. Implications of this work for future studies of myosin physiological function are discussed in Chapter 6.

# Table of Contents

# List of Tables

# List of Figures

# Abbreviations[1]

| | |
|---|---|
| Abi: | Abelson-interacting protein |
| ADP: | Adenosine Diphosphate |
| ANOVA: | Analysis of Variance |
| Arf: | ADP ribosylation factor |
| Arp: | Actin-related protein |
| ATP: | Adenosine Triphosphate |
| ATWD: | Analog Transient Waveform Digitizer |
| BAR: | Bin-Amphiphysin-Rvs (InterPro: IPR004148) |
| BFP: | Blue Fluorescent Protein |
| CA: | Constitutively Active (i.e., favoring the GDP holoenzyme) |
| cAMP: | 3′,5′-cyclic Adenosine Monophosphate |
| CC: | Coiled Coil |
| CCD: | Charge Coupled Device |
| CH: | Calponin Homology (InterPro: IPR001715) |
| CI: | Constitutively Inactive (i.e., favoring the GTP holoenzyme) |
| CRIB: | Cdc42/Rac interactive binding (InterPro: IPR000095) |
| CV: | Coefficient of Variation |

[1] Nomenclature references to HGNC (http://www.genenames.org/) or InterPro (http://www.ebi.ac.uk/interpro/) databases are supplied where applicable.

DdMhcA: *Dictyostelium discoideum* Myosin heavy chain A (=Myosin 2)

DdMyo7: *Dictyostelium discoideum* Myosin 7

DHR1: DOCK Homology Region 1 (InterPro: IPR027007)

DHR2: DOCK Homology Region 2 (InterPro: IPR027357)

Dia2: Diaphanous related formin-2 (HGNC: 2877)

DTT: Dithiothreitol

DWR: Direct Waveform Recording

EDTA: Ethylenediaminetetraacetic Acid

EDANS: 5-((2-aminoethyl) amino) naphthalene-1-sulfonic acid

eGFP: enhanced Green Fluorescent Protein

ELC: Myosin Essential Light Chain

EMCCD: Electron Multiplication-Charge Coupled Device

ENA: European Nucleotide Archive

ER: Endoplasmic Reticulum

EVH1: Ena/VASP Homology 1 (InterPro: IPR033927)

EVH2: Ena/VASP Homology 2 (=WH2, see.)

F-BAR: FCH-BAR (InterPro: IPR031160)

FCH: fps/fes-related & Cdc42-interacting protein 4 Homology (InterPro: IPR001060)

FERM: band Four point one, Ezrin, Radixin, Moesin (InterPro: IPR000299)

FH: Formin Homology (InterPro: IPR015425)

FRET: Förster Resonance Energy Transfer

| | |
|---|---|
| FWHM: | Full Width at Half Maximum |
| GAP: | GTPase Activating Protein |
| GEF: | Guanine nucleotide Exchange Factor |
| GTP: | Guanosine triphosphate |
| HEPES: | *N*-2-Hydroxyethylpiperazine-*N*′-2-Ethanesulfonic acid |
| HGNC: | Human genome organization Gene Nomenclature Committee |
| HTRF: | Homogeneous Time-Resolved Fluorescence |
| I-BAR: | Inverse BAR (InterPro: IPR031160) |
| IQ: | IQ calmodulin-binding motif (InterPro: IPR000048) |
| IQGAP: | IQ motif-containing GTPase Activating Protein |
| IRF: | Instrument Response Function |
| IRM: | Interference Reflection Microscopy |
| KKAA: | K2333A, K2336A (DdMyo7 mutant) |
| KO: | Knockout (null mutant) |
| LD: | Leucine-aspartate interaction motif of paxillin |
| LIM: | LIN-11/Isl1/MEC-3 (InterPro: IPR001781) |
| MF: | MyTH4-FERM |
| MGI: | Mouse Genome Informatics |
| MHCK: | Myosin Heavy Chain Kinase |
| MLCK: | Myosin Light Chain Kinase (HGNC:7590) |
| mRFP: | monomeric Red Fluorescent Protein |
| MRL: | MIG10/RIAM/Lamellipodin |

| | |
|---|---|
| MyTH4: | Myosin Tail Homology 4 (InterPro: IPR000857) |
| NA: | Numerical Aperture |
| Nck: | Non-catalytic region of tyrosine kinase adaptor (HGNC: 7664) |
| NowGFP: | Now Green Fluorescent Protein |
| PH: | Pleckstrin Homology (InterPro: IPR001849) |
| PI(3,4,5)P3: | Phosphatidyl inositol-3,4,5-trisphosphate |
| PMT: | Photo-Multiplier Tube |
| Pro1/Pro2: | Proline-rich region 1 & 2 |
| RasGAP: | Ras GTPase Activating Protein (InterPro: IPR001936) |
| ReAsH: | Resorufin Arsenical Hairpin |
| RLC: | Myosin Regulatory Light Chain |
| RMSD: | Root-Mean-Squared Deviation |
| SAH: | Single Alpha Helix |
| SAR: | Stramenopiles, Alveolates, Rhizaria |
| SATé: | Simultaneous Alignment and Tree éstimation |
| SCAR: | Suppressor of Cyclic AMP Receptor mutation |
| SD: | Standard Deviation |
| Sec7: | Secretion mutant 7 (InterPro: IPR000904) |
| SEM: | Standard Error of the Mean |
| SNR: | Signal-to-Noise Ratio |
| SPC: | Single Photon Counting |
| SH3: | Src Homology 3 (InterPro: IPR001452) |

| | |
|---|---|
| TCSPC: | Time-Correlated Single-Photon Counting |
| TIRF: | Total Internal Reflection Fluorescence |
| TORC2: | Target of Rapamycin Complex 2 |
| VASP: | Vasodilator-Stimulated Phosphoprotein (HGNC:12652) |
| VCA: | Verprolin homology, Cofilin homology, Acidic (InterPro: IPR011026) |
| WASP: | Wiskott-Aldrich Syndrome Protein (HGNC:12731) |
| WAVE: | WASP-family Verprolin homology protein |
| WCA: | WH2, Central, Acidic (=VCA, see.) |
| WH1: | WASP Homology 1 (InterPro: IPR000697) |
| WH2: | WASP Homology 2 (InterPro: IPR003124) |
| WRC: | WAVE Regulatory Complex |
| WT: | Wild Type |

# 1 Mechanical Control of Cell Shape and Motion by Actin and Myosin

## 1.1 Motor Proteins

Living organisms have a fundamental requirement to control mechanical forces in the cell. Direct control is provided by molecular motor proteins. Rotary motor proteins unwind chromosomal DNA for replication and transcription, interact with ribosomal RNA for ribosome assembly, and perform ATP synthesis to power basic metabolism in both prokaryotes and eukaryotes (1, 2). Prokaryotes also employ rotary flagellar motors in cell motility, unlike eukaryotes (3). The complex subcellular architecture of eukaryotic cells is maintained not only by rotary motors but by dynamin, a twisting motor that facilitates endocytosis (4), and the ***cytoskeletal molecular motors,*** myosin, dynein, and kinesin (5–10), that undergo linear motion to exert forces on polymeric tracks of cytoskeletal proteins while delivering cargo, producing cytoskeletal tension, and generating contractile forces. Myosin, dynein, kinesin, and dynamin are members of the P-loop NTPase superfamily, having conserved structural mechanisms for recognizing, binding, and hydrolyzing nucleotide triphosphate (11, 12). ATP is the preferred substrate for the cytoskeletal motors while GTP is used by dynamin and the distantly related Rho family of proteins (13–15)

Dynein and kinesin motor proteins interact with microtubules (cylindrical polymers of heterodimeric tubulin subunits). Dynein motors move exclusively toward the microtubule minus end to transport cargo or to generate contractile forces in motile cilia (8). Kinesins,

in contrast, are structurally and functionally diverse with various kinesins able to move in minus or plus end directions as monomers, dimers, or multimeric teams. Kinesins play essential roles in microtubule-based transport and microtubule organization in mitosis and meiosis, as does cytoplasmic dynein (16–19).

Myosin interacts with filamentous actin (***F-actin)*** to generate motion toward the fast-growing ('barbed') end of the filament, or more rarely, toward the 'pointed' end (Fig. 1). Myosin consists of a conserved catalytic domain containing an upper and a lower actin binding site, a nucleotide binding site, a buried 7-stranded β-sheet ('transducer'), and a force-generating subdomain ('converter') that undergoes conformational change to rotate the light-chain binding domain ('lever arm') at a pivot adjoining the motor domain. Force is transmitted through the converter, lever arm, and C-terminal region ('tail') to the myosin ***cargo***. Depending on specific interactions of the tail, the cargo may be a protein or lipid molecule that interacts with the tail, a signaling domain in the tail, or a myosin filament.

Myosin binds and hydrolyzes ATP when detached from actin, but does not release reaction products until after the initial contact, a primarily electrostatic interaction with the lower actin binding site ('weak binding'). Following release of inorganic phosphate, the upper site also binds actin in a stereospecific attachment ('strong binding'). Myosin interacts most strongly with actin in the ADP-bound or nucleotide-free (apoenzyme) form. These states are highly populated when ATP stores are depleted following cell death (*rigor mortis*); thus, conditions favoring strongly bound myosin are termed ***rigor*** conditions. In contrast the high-ATP environment of a typical cell creates a condition of ***relaxation*** in

which myosin only briefly experiences strong binding to actin; nucleotide hydrolysis takes place primarily when myosin is detached from actin, and actin binding accelerates release of the hydrolysis products (20, 21). Curiously kinesin performs these events in the opposite order; ATP hydrolysis occurs while the motor is attached to its microtubule track, despite extensive structural homology of the core motor domains of myosin and kinesin (22).

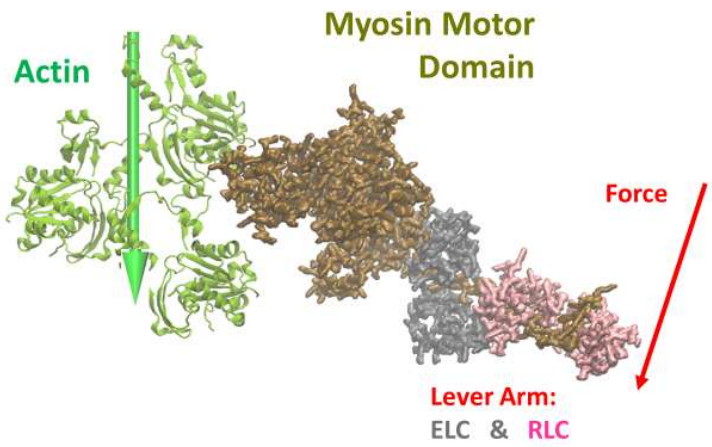


**Fig. 1. Force Generation by Actin-Myosin Interaction.**
Myosin is shown in the post-powerstroke conformation, strongly bound to an actin filament (left). Rotation of the light-chain binding domain ("Lever Arm") in the downward direction (red arrow) results in movement of the motor domain toward the actin filament barbed end (green arrow). The lever arm is stabilized by two bound calmodulin-like proteins, the essential and regulatory light chains (ELC & RLC) Model from **(23)**.

Myosin and actin are highly conserved across eukaryotic kingdoms. Actin is ubiquitous in eukaryotes where it is essential for control of cell shape and mechanical stiffness (cell motility) and for establishing cell polarity (24). Recent discovery of multiple actin homologs in Archaea suggests a molecular ancestor of actin predates the emergence of eukaryotes (25, 26). Myosin is widespread among all known branches of the eukaryotic tree of life but lacks the extreme structural conservation of its partner actin. Functional diversification appears to have occurred early

in eukaryotic evolution and continues to the present. Several ancient myosin classes are conserved between Amoebozoa, Fungi and animals including Myosin 1 (monomeric motors involved in actin-membrane interactions), Myosin 2 (dimeric filament-forming motors producing contractile forces), and Myosin 5 (dimeric transport motors) (27–29). These myosin classes are not universal as, for example, plants possess divergent myosin classes 8 and 11 (30–32). Some single-celled parasitic organisms such as *Trichomonas vaginalis* and *Giardia intestinalis* lack myosins but whether the loss is only possible for obligate parasites is unclear (33)[1]. Nevertheless, the widespread distribution of myosin classes 1, 2, and 5 suggests they descend from myosin genes present in the last eukaryotic common ancestor.

## 1.2 Actin-based Cell Motility

Actin is abundant in cells. The monomeric form of actin readily polymerizes at physiological concentrations of mono- or divalent cations. A key aspect of actin regulation is the prevention of spontaneous polymerization so that the chemical potential energy of actin assembly may be harnessed for force generation. Control of actin polymerization is achieved by limiting the free monomeric pool with G-actin binding proteins (binding to 'globular' or monomeric actin) such as profilin and cofilin (conserved in animals, Fungi, amoebae, and plants) (34) as well as thymosin β4 (conserved in animals, and in amoebae

[1] See also http://cymobase.org/cymobase for myosin sequences from a diverse range of organisms.

as actobindin (35)). Other proteins bind to F-actin ('filamentous' actin) either severing the filaments (cofilin, gelsolin and fragmin (36)) or sterically 'capping' their growing ends (37). Both types of F-actin binding protein are extensively conserved.

Growth of actin filaments and larger actin-based structures is accomplished by actin nucleation factors, principally formins and the Arp2/3 complex. Although actin polymerization is thermodynamically favorable, nucleation of actin filaments requires a ternary collision complex that occurs quite slowly at physiological concentrations of free G-actin. Formins can accelerate formation of filaments *de novo* by recruitment and dissociation of the profilin-actin complex although the precise mechanism is obscure (38). The seven-membered Arp2/3 complex is a structural mimic of the ternary actin complex that is competent for polymerization when bound to the side of a pre-existing filament (24, 39). The Arp2/3 complex generates branched or 'dendritic' actin filament arrays because Arp2/3 makes a 70° branch angle at the array nodes. Actin filament elongation takes place at a much faster rate than filament nucleation. The rate of actin polymerization in the cell is accordingly proportional to the number of uncapped (growing) filament ends. Thus, actin polymerization is under both thermodynamic control (limiting the concentration of free G-actin) and kinetic control (limiting the concentration of free F-actin barbed ends).

Growth of dendritic actin networks via Arp2/3 provides the driving force for cell migration through expansion of lamellipodia and pseudopodia. The Arp2/3 complex is regulated by two proteins, WASP and WAVE, that use a common mechanism yet operate in distinct pathways (40–42). The VCA motif of WASP/WAVE binds and activates the

Arp2/3 complex. WASP is regulated by direct binding to the Cdc42 GTPase while WAVE functions as part of the five-membered complex (WRC) regulated by interaction of the Sra1 subunit with Rac GTPases (42, 43)[1]. These small GTPases act as molecular switches that activate actin polymerization in response to upstream signaling receptors, mediated by physical association of WASP and/or WAVE with Nck family signal adaptors (44, 45).

## 1.3 Conventional Myosins: Continuous Contraction

Class 2 myosins are known as "conventional" myosins because early studies of actin and myosin concentrated on skeletal muscle preparations containing Myosin 2 protein. Conventional myosins generate the contractile forces of cell migration, cytokinesis and muscle contraction. A long (~ 100 nm) coiled coil region, adjacent to the lever arm, promotes dimerization followed by oligomerization of antiparallel filaments. This antiparallel configuration orients the myosin motor domains such that the working stroke is directed inward, toward the center of the filament. The average motion contracts the actin network since the geometry of the actin-myosin bond only permits motion in one direction. The opposite configuration, where myosin filaments generate expansive forces, does not occur presumably because the actin network itself generates sufficient expansion[2].

---

[1] Consisting of SCAR/WAVE (*WAVE1* or *WAVE2*), Sra1/PIR121 (*CYFIP2*), Abi (*ABI1* or *ABI2*), Nap1/Nap125/Hem-2/Kette (*NCKAP1*), and HSPC300/HSPC3000/Brick-1 (*BRK1*). Standard HGNC symbols *italic*, see: http://www.genenames.org/.

[2] Non-filamentous myosins, however, can generate expansive forces within actin networks (46).

**Table 1. Human Conventional Myosin Genes**

| Gene[1] | Myosin class | HGNC | CyMoBase | Location | Accession No. | UniProt |
|---|---|---|---|---|---|---|
| *MYH1* | Skeletal IIx | 7567 | Mhc1 | 17p13.1 | NM_005963 | P12882 |
| *MYH2* | Skeletal IIa | 7572 | Mhc2 | | NM_017534 | Q9UKX2 |
| *MYH3* | Skeletal embryonic | 7573 | Mhc3 | | NM_002470 | P11055 |
| *MYH4* | Skeletal IIb | 7574 | Mhc4 | | NM_017533 | Q9Y623 |
| *MYH8* | Skeletal perinatal | 7578 | Mhc8 | | NM_002472 | P13535 |
| *MYH10* | Non-muscle IIb | 7568 | Mhc10 | | NM_001256012 | P35580 |
| *MYH13* | Skeletal extraocular | 7571 | Mhc13 | | NM_003802 | Q9UKX3 |
| *MYH6* | Atrial cardiac | 7576 | Mhc6 | 14q11.2 | NM_002471 | P13533 |
| *MYH7* | Skeletal slow & Ventricular cardiac | 7577 | Mhc7 | | NM_000257 | P12883 |
| *MYH9* | Non-muscle IIa | 7579 | Mhc9 | 22q12.3 | NM_002473 | P35579 |
| *MYH11* | Smooth muscle | 7569 | Mhc11 | 16p13.11 | NM_001040113 | P35749 |
| *MYH14*; *MYH17*, formerly | Non-muscle IIc | 23212 | Mhc16 | 19q13.33 | NM_024729 | Q7Z406 |
| *MYH7B*; *MYH14*, formerly | Embryonic/perinatal myosin of unknown function (47–51) | 15906 | Mhc14 | 20q11.22 | NM_020884 | A7E2Y1 |
| *MYH15* | Skeletal extraocular perinatal (47, 48) | 31073 | Mhc15 | 3q13.13 | XM_036988 | Q9Y2K3 |
| *MYH16*; *MYH5*, formerly | Pseudogene relative of invertebrate muscle myosin (47) | 31038 | Mhc20 | 7q22.1 | NR_002147 | |

[1] The following gene names are retired: *MYH5* (=*MYH16*), *MYO12* (=*MYO5A*), and *MYH17* (=*MYH14*)

[2] CyMoBase v 2.0.0 accessed 19 Nov 2016, see http://cymobase.org/cymobase

Conventional myosin genes are extensively duplicated in bilaterian animals supporting increasingly specialized muscle tissue types (52, 53). Mammals have three muscle types: smooth muscle of the uterus, gastrointestinal and circulatory systems, and two striated types, skeletal muscle and cardiac muscle. Striated muscles are named for their regular

striations formed by sarcomeric arrays of actin and myosin filaments. Smooth muscle myosin is divergent from the striated muscle myosins, being more closely related to non-muscle myosins employed in cytokinesis and cell migration (28, 54, 55). Humans possess 1 smooth, 3 non-muscle, and 10 striated muscle myosin genes (Table 1), each with kinetic and regulatory adaptations in many cases accompanied by tissue-specific ELC and RLC gene expression (56). Intracellular calcium is the primary regulator of conventional myosin, either by direct binding of the ELC (invertebrate muscle myosins and *Physarum* myosin 2); indirectly by calmodulin-mediated activation of myosin light chain kinase (smooth muscle myosins, non-muscle myosin and vertebrate striated muscle myosins); or through the troponin-tropomyosin complex (a unique adaptation of vertebrate striated muscle).

## 1.4 Unconventional Myosins: Tension and Transport

Non-class 2 ('unconventional') myosins exhibit diverse, principally cytosolic functions including building and maintaining actin-based protrusions, recognizing and delivering subcellular cargo molecules, regulating the formation of cell-substrate adhesion complexes, and acting as mechanically sensitive signaling molecules (Table 2).

Myosin 1 is the largest unconventional myosin class with 8 representatives in humans. Myosin 1 motors generate tension across actin filaments and lipid membranes, either promoting membrane tension, fission and fusion, or providing mechanical feedback.

**Table 2. Human Unconventional Myosin Genes**

| Gene[1] | Primary Function | Specialization | HGNC | Accession No. | UniProt |
|---|---|---|---|---|---|
| *MYO1A* | Generate and sense tension at actin-membrane interfaces (57) | Vesicle transport | 7595 | NM_005379 | Q9UBC5 |
| *MYO1B* | | Vesicle transport | 7596 | NM_012223 | O43795 |
| *MYO1C* | | Force-sensing | 7597 | NM_001080779 | O00159 |
| *MYO1D* | | Vesicle fusion | 7598 | NM_001303279 | O94832 |
| *MYO1E* | | Endocytosis | 7599 | NM_004998 | Q12965 |
| *MYO1F* | | Decreased adhesion | 7600 | NM_012335 | O00160 |
| *MYO1G* | | Lymphocytes | 13880 | NM_033054 | B0I1T2 |
| *MYO1H* | | Unknown | 13879 | NM_173597 | Q8N1T3 |
| *MYO3A* | Transport (58, 59) | Stereocilia elongation | 7601 | NM_017433 | Q8NEV4 |
| *MYO3B* | | | 15576 | NM_001083615 | Q8WXR4 |
| *MYO5A* | Transport (60–62) | Vesicle secretion | 7602 | NM_000259 | Q9Y4I1 |
| *MYO5C* | | Vesicle secretion | 7604 | NM_018728 | Q9NQX4 |
| *MYO5B* | | Receptor trafficking | 7603 | NM_001080467 | Q9ULV0 |
| *MYO6* | Transport (63) | Retrograde | 7605 | NM_004999 | Q9UM54 |
| *MYO7A* | Cargo Transport & Scaffold (64–66) | Stereocilia & retina | 7606 | NM_000260 | Q13402 |
| *MYO7B* | | Microvilli | 7607 | XM_291001 | Q6PIF6 |
| *MYO9A* | RhoGAP (regulator of F-actin) (67, 68) | Cell-cell adhesion | 7608 | NM_006901 | B2RTY4 |
| *MYO9B* | | Decreased invasion | 7609 | NM_001130065 | Q13459 |
| *MYO10* | Transport (69–72) | Filopodia formation | 7593 | NM_012334 | Q9HD67 |
| *MYO15A* | Transport (73) | Stereocilia elongation | 7594 | NM_016239 | Q9UKN7 |
| *MYO15B* | Pseudogene (74) | | 14083 | NR_003587 | |
| *MYO16* | Scaffold (75, 76) | Cell migration | 29822 | NM_015011 | Q9Y6X6 |
| *MYO18A* | Scaffold; may be inactive (77) | Non-muscle myosin filament assembly | 31104 | NM_078471 | Q92614 |
| *MYO18B* | Unknown (78–81) | Tumor suppressor | 18150 | NM_032608 | Q8IUG5 |
| *MYO19* | Transport (82) | Mitochondrial outer membrane-associated | 26234 | NM_025109 | Q96H55 |

Myosin 5 and Myosin 6 function primarily as cargo delivery molecules, particularly

in vesicle transport. Myosins 3, 7, 10, 15, and 19 function as cargo transporters although these motors may have additional roles in generating local tension or acting as mechanically sensitive signal adaptors. Myosin 9 is unusual in that its 'cargo', a RhoGAP signaling domain, is part of the tail. Myosins 16 and 18 are incompletely characterized but may function as signal adaptors or scaffolds in cell migration (Myo16) and non-muscle myosin assembly (Myo18A).

The diversity of myosin genes in the human genome reveals not only a high degree of tissue-specific adaptation, in many cases conserved in vertebrates, but also the wide range of mechanical and biochemical functions that myosins have adopted. To better understand the origins of myosin diversity in animals, it is helpful to turn to a model organism.

## 1.5 *Dictyostelium* is a Developmental Model Organism

*Dictyostelium discoideum* is an amoebozoan model organism for understanding cell migration, cytokinesis, and the origins of multicellular development (83, 84). The Amoebozoa are the closest living relatives of Opisthokonta (Fig. 2), a phylogenetic supergroup that includes Fungi, Metazoa (animals), and their unicellular relatives.

*Dictyostelium* amoebae are aerobic migratory cells that lead a foraging lifestyle in temperate habitats such as the leaf litter and surface soil of deciduous forests. The amoeboid cells are protected by a thick glycoprotein coat that permits nonspecific adhesion to objects encountered during migration. The cells subsist primarily by phagocytosis of bacteria that are recognized upon contact. The processes of migration and phagocytosis are

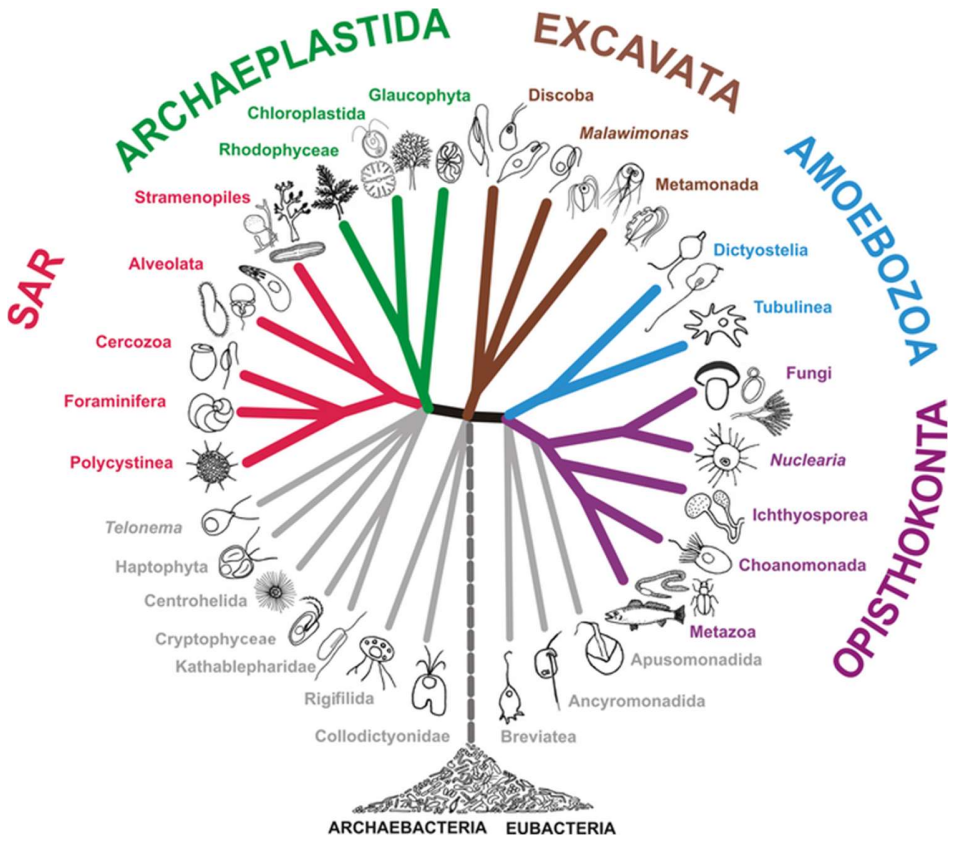


**Fig. 2. Phylogenetic Classification of Eukaryotes.**

The Ameobozoa share a common ancestor with Fungi and animals (Metazoa). The SAR group shares a common ancestor with plants (Archaeplastida = Viridiplantae). Figure reprinted with permission and amended **(85, 86)**; © 2012 International Society of Protistologists.

driven by actin-based cell motility with essential roles for myosin motors, pathways that are largely conserved in humans and most closely resemble the phagocytic behavior of human macrophages.

When food becomes scarce, a developmental program initiates secretion of cAMP-producing exosomes accompanied by a cAMP-degrading phosphodiesterase (87–90). These two enzymes establish a reaction-diffusion mechanism that generates [cAMP] waves propagating in the moist environment (91, 92). The amoebae direct their migration toward

increasing [cAMP] leading them to meet and form multicellular aggregates.

In the later phases of development, cell-cell cohesion organizes the cell mass into a pseudoplasmodium or 'slug' (93–95). The slug is strongly phototactic and may make a second migration to find a better environment for dissemination of spores. During the final phase the slug becomes a fruiting body (sorus) differentiating into somatic cells that form a rigid cellulose stalk several millimeters tall supporting a spherical mass of spore cells. The stalk cells experience autophagy-mediated death while the spore cells, themselves encased in a cellulose coat, germinate when environmental conditions are favorable. Myosins are critically involved in tension generation to support migration of individual cells, as well as generating forces used to sort differentiating cells by type within the slug and to elevate the spores and stalk cells within the sorus.

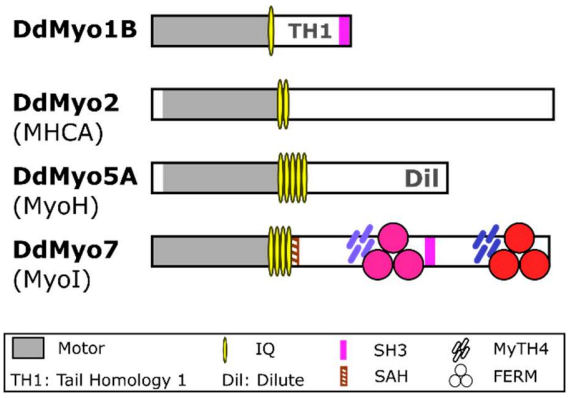


**Fig. 3. Principal Myosin Classes in *Dictyostelium*.**
*Dictyostelium discoideum* possesses Myosin 1 (represented by Myo1B), Myosin 2 (MHCA), Myosin 5 (represented by MyoH), and Myosin 7 (MyoI). See also Table 3.

Myosins have conserved physiological functions in *Dictyostelium,* represented by seven Myosin 1, one Myosin 2, and two Myosin 5 (Fig. 3, Table 3). The *Dictyostelium* Myosin 2 (DdMhcA) is structurally and functionally homologous to human non-muscle myosins, with additional essential roles in development of the slug and fruiting body, and has been used as a model in numerous structural and kinetic studies. Myosins 1, 2, and 5

are ubiquitous in Amoebozoa as they are in animals and many Fungi.

**Table 3. Amoebozoan Myosin Genes**

| Myosin class | Primary Function | Gene in *Dictyostelium discoideum* | ENA Accession | UniProt ID | Gene in *Acanthamoeba castellanii* | UniProt ID |
|---|---|---|---|---|---|---|
| Myo1 | Generate and sense tension at actin-membrane interfaces | *myoA* | EAL67246 | P22467 | ACA1_362570 | L8GGA4 |
| | | *myoB* | EAL62866 | P34092 | MIB | P19706 |
| | | *myoC* | EAL69121 | P42522 | MIC<br>MICHC | P10569<br>O61080 |
| | | *myoD* | EAL69474 | P34109 | ACA1_173680 | L8HHR2 |
| | | *myoE* | EAL63071 | Q03479 | - | - |
| | | *myoF* | EAL62822 | P54695 | - | - |
| | | *myoK* | EAL70180 | Q9XXV8 | AcMyo1G[1] | - |
| Myo2 | Contraction | *mhcA* | EAL64202 | P08799 | ACA1_326740 | L8HMU1 |
| Myo4 | Unknown (96) | - | - | - | HMWMI | P47808 |
| Myo5 | Cargo transport | *myoH* | EDR41040 | P54696 | ACA1_224860 | L8GSY9 |
| | | *myoJ* | EAL71208 | P54697 | ACA1_322090 | L8GN06 |
| Myo7 | Filopodia formation and cell-substrate adhesion | *myoI* | EAL70120 | Q9U1M8 | ACA1_066150<br>ACA1_084860<br>ACA1_108600<br>ACA1_175100<br>ACA1_264090<br>ACA1_265440 | L8GX00<br>L8HKE9<br>L8GF39<br>L8HK97<br>L8H3E7<br>L8H1F4 |
| Myo44 | Chemotaxis in social amoebae (97, 98) | *myoG* | EAL69262 | Q86AC8 | - | - |
| Myo45 | Unknown (99); RhoGEF activity | *myoM* | EAL61255 | Q9TW28 | - | - |

[1] CyMoBase v 2.0.0 accessed 19 Nov 2016, see http://cymobase.org/cymobase

*Dictyostelium* possess a Myosin 7 (DdMyo7) that has critical roles in phagocytosis, calcium-dependent cell-cell cohesion, spore morphogenesis and filopodia formation.

DdMyo7 has similarities to human Myosin 10 as well as Myosin 7, a relationship that is the focus of the next chapter. This myosin is well-represented throughout Amoebozoa, with representatives in *Physarum polycephalum* and the solitary amoeba *Acanthamoeba castellanii.*

Two myosin classes unique to Amoebozoa are represented by *Dictyostelium* Myosin 44 and Myosin 45. Myo44 is essential for cAMP-dependent chemotaxis and development. Myo44, a paralog of Myosin 7, is present only in the social amoebae (Dictyostelia). Although it is possible that this myosin was lost in other lineages, the critical function of Myo44 in multicellular development argues that it arose by duplication of Myosin 7 during evolution of the social amoebae. Myo45 is a myosin of unknown function that contains a RhoGEF domain affecting local actin dynamics under conditions of hyperosmotic stress. Myo45 is common in social amoebae and has also been identified in the solitary amoeba *Balamuthia mandrillaris*[1], suggesting that the class arose early in amoebozoan evolution.

Comparison of the myosin gene family in humans with the myosins in *Dictyostelium* shows broad structural and functional conservation of Myosin 1, 2, and 5. While considerable specialization is seen within these classes, Myosin 1 is essential for actin-membrane interactions in both organisms, while non-muscle Myosin 2 is involved in contraction and Myosin 5 plays essential roles in intracellular transport. However, the

[1] CyMoBase v 2.0.0 accessed 19 Nov 2016, see http://cymobase.org/cymobase

function of *Dictyostelium* Myosin 7, and how it relates to human Myosin 7, is less clear.

## 1.6 MyTH4-FERM Myosins

Myosins of class 4, 7, 10, 15, 22, 32, 44 and 55 contain MyTH4-FERM domains in their tail regions. It is not known whether these myosins evolved from a single ancestral myosin or whether the MF domain has been introduced on independent occasions, but the roles of MF domain in regulating cytoskeletal proteins suggests common adaptive pressures at work. The MyTH4 domain is a bundle of six helices that possesses microtubule-binding activity (100–102). FERM domains contain 3 closely packed globular subdomains that can bind diverse specific targets and often have F-actin binding activity (102–104). MyTH4-FERM domains form a compact supramodule in myosins, the conserved plant kinesin *zwichel* (105), and the conserved holozoan gene *max-1/PLEKHH* (106).

The physiological functions of several classes of MF myosin are unknown. These include Myo4 (found in solitary amoebae and the SAR group), Myo22 (arthropods, choanoflagellates, and some Fungi), Myo32 (SAR group), and Myo55 (apicomplexans such as the malarial parasite *Plasmodium falciparum*). Uncertainty persists in part because of the narrow phylogenetic distribution of these myosins and lack of genetic model systems to investigate their function.

MF myosins in mammals have been described in a rich literature identifying roles in growth and maintenance of actin-based structures such as stereocilia (Myo7A & Myo15),

retinal microvilli/calyceal processes (Myo7A), gut microvilli (Myo7B), filopodia, invadopodia, and podosomes (Myo10)[1]. Each of these structures is characterized by tight bundles of actin filaments with barbed ends aligned at their distal tip. Loss of the specific MF myosin causes defects ranging from severe disorganization (stereocilia, microvilli) to complete loss (filopodia). These MF myosins thus appear to have similar functions in organization of actin-based structures despite vast differences in the time scale of these structures, ranging from decades (stereocilia) to as short as a few seconds (filopodia).

A central question concerning MF myosins is whether cargo transport is an essential physiological function. Myosin 7A & 7B appear to have complementary, but distinct, roles as transporters and as signal scaffolds. Myo7 forms a multiprotein complex, including a cadherin adhesion receptor. The motor activity of Myo7 appears to drive the complex to the barbed end while ensuring the complex assembles in the correct location (107, 108). Myosin 10 appears to have separated cargo transport from filopodia formation functions, as it traffics the BMP receptor (109), netrin receptor (110), and V/E cadherin (111) at the tips of filopodia independently of filopodia formation. However the Myosin 10 tail is essential in both cases as expression of Myosin 10 lacking the MF domain cannot rescue the dorsal filopodia of HeLa cells (112, 113). This raises the question of how the MF domain participates in filopodia formation, whether by helping to generate local tension through binding F-actin filaments or by some other interaction. This has been difficult to

[1] See Table 2 for references.

address in human cells due to the lack of Myo10-null cell lines. Furthermore, the *Dictyostelium* Myosin 7 (DdMyo7) has an essential role in filopodia formation and *Dictyostelium* cells express a broadly homologous complement of proteins involved in actin-based motility, and deletion of many of these proteins alters filopodia number, length and/or cell adhesion (Table 4). This functional conservation suggests that the mechanism(s) of filopodia formation have been conserved, but the role of MF myosins in this process remains mysterious.

Understanding the physiological function of myosins will require both a molecular understanding of how these motors are localized and activated in the cell and a biophysical understanding of how myosin activation and force generation are involved in the physiological mechanism (e.g., filopodia formation). To begin to understand how MF myosins function *in vivo*, DdMyo7 was used as a molecular genetic model to investigate questions of how filopodial myosins function.

**Table 4. Filopodial Proteins in Amoebozoa.**

| Protein | Gene | Architecture | Activity | Localization | Null and Other Phenotypes | Interaction | Notes | Ref. |
|---|---|---|---|---|---|---|---|---|
| Motors | | | | | | | | |
| DdMyo7 | *myoI* | Myosin; IQ (×4); SAH; MyTH4-FERM (×2); SH3 | Phagocytosis, Filopod formation, cell-cell adhesion | Filopodia tip, leading edge, cytosol, cell-cell contacts | No filopodia, decreased cell-substrate adhesion, loss of Ca-dependent cell-cell adhesion, decreased particle adhesion and phagocytosis, decreases in cell size and spore germination | Talin A | Post-lever arm region required for filopodia tip localization; MF required for filopod formation | (114–116) |
| MhcA (Myosin 2) | *mhcA* | Myosin; IQ (×2); Coiled coil | Cortical tension, contraction, cytokinesis | Actin cortex, cytosol, cleavage furrow | No-phos (3xAla): decreased filopodia<br>Pseudo-phos (3xAsp): increased filopodia | ELC, RLC, MHCK | Pseudo-phos mutant unable to assemble as filaments | (117–119) |
| Myo1B | *myoB* | Myosin; IQ; MyTH1; MyTH2; SH3 | Membrane anchoring and tension sensing | Filopodia, actin cortex | Defects in phagocytosis and development, control of pseudopod formation, and endocytic recycling | CARMIL (120) | | (121–127) |
| Myo1D | *myoD* | Myosin; IQ; MyTH1; MyTH2; SH3 | Membrane anchoring | Filopodia, actin cortex | Unknown; compound phenotype with *myoE* and *myoF* | | | (123, 128–130) |

| Protein | Gene | Architecture | Activity | Localization | Null and Other Phenotypes | Interaction | Notes | Ref. |
|---|---|---|---|---|---|---|---|---|
| **Actin Polymerization Factors** | | | | | | | | |
| Dia2 | *forH* | FH3; FH1; FH2 (×2) | Actin filament anti-capping (barbed end) | Filopodia tip, cytosol | Decreased filopodia number and length, increased cell speed; *dia2*+: increased filopodia number and length | Profilin II (FH1); Rac1.GTP; VASP (FH1-FH2) | FH1-FH2 required for filopodia tip localization and VASP binding | (131) |
| VASP | *vasp* | EVH1 (incl. WH1); EVH2 (=WH2); Coiled coil | Actin filament bundling and nucleation | Filopodia tip, leading edge, cell-cell contacts, cytosol | No filopodia, decreased substrate & particle adhesion, cell size and speed *vasp*+: increased filopod number; *vaspΔEVH1*+: numerous short filopodia | Dia2; Profilin III; Unidentified kinase(s) | Pseudo-phos mutant: Decreases in filopodia and F-actin polymerization | (115, 132–134) |
| SCAR/ WAVE | *scrA* | Core member of a heteropentameric complex (WRC) | Actin nucleation at Arp2/3 branches | Filopodia tip, pseudopodia, cell-cell contacts | Not essential for filopodia | Arp2/3 | Similar localization for all complex components | (42, 135, 136) |
| WIP | *wipA* | WH2 | Actin protrusions | Actin cortex, cytosol | Knockdown has decreased filopodia number, decreased F-actin; *wipA*+ has increased filopodia number, increased F-actin at leading edge | WASP, VASP (via WH1) | WIP does not translocate to cortex in VASP-null cells | (132, 137, 138) |

| Protein | Gene | Architecture | Activity | Localization | Null and Other Phenotypes | Interaction | Notes | Ref. |
|---|---|---|---|---|---|---|---|---|
| WASP | *wasA* | WH1; CRIB; WH2 | Actin nucleation at Arp2/3 branches | Actin cortex, enriched at leading edge | *wasA*$^{TK}$*:* Chemotaxis defects, decreased actin leading edge; inhibition with wiskostatin does not alter filopodia | WIP (WH1); Arp2/3; RacC (CRIB) | Filopodia data not reported for *wasA*$^{TK}$ cells | (42, 139–141) |
| GTPases and Regulatory Proteins | | | | | | | | |
| Rac1 | *rac1a,b, c* | Rho GTPase | Regulation of actin | Plasma membrane anchored, also in cytosol | *rac1a*+: increased filopod number; CA mutant: no filopodia; CI mutant: numerous short filopodia | DGAP1, Dia2, PakA, Filamin | *rac1a*+ yields strongest phenotype; analogous to mammalian Rac | (142–144) |
| RacC | racC | Rho GTPase | Regulation of actin | Pseudopodia, filopodia; punctate | Defects in chemotactic signaling, speed and persistence | WASP | Analogous to Cdc42 | (145) |
| RacG | *racG* | Rho GTPase | Regulation of actin | Plasma membrane, cytosol | *racG*+: very numerous filopodia | | | (146) |

| Protein | Gene | Architecture | Activity | Localization | Null and Other Phenotypes | Interaction | Notes | Ref. |
|---|---|---|---|---|---|---|---|---|
| RacH | *racH* | Rho GTPase | Regulation of actin | ER and Golgi membranes | Defects in endocytosis and exocytosis | | Induces long filopodia when targeted to membrane with RacG motif | (147) |
| Zizimin | *zizB* | DHR1 (binds PIP3); DHR2 (GEF) | RhoGEF (Dock family) | Filopodia (not enriched at tip), membrane | Small decreases in cell speed and time to develop; Defective fruiting bodies *zizB+:* Doubled number of filopodia, defect in cytokinesis | Rac1; formin A; Arp2/3 | Upregulated in chemotactic cells | (148) |
| MEGAP1 | *mgp1-4* | F-BAR RhoGAP | Tubulation, curvature in vacuole network | Cytosol, transiently to contractile vacuole | More numerous & slowly contracting vacuoles; increased filopodia number; motility & development defects | | Unclear if GAP is active; protein function attributed to F-BAR | (149) |
| RasG | *rasG* | Ras GTPase | Regulation of growth and development | Plasma membrane, actin cortex, cytosol | Numerous long filopodia (compare *acapA+*); CA mutant: reduced filopodia number | | | (150, 151) |
| DGAP1 | *rgaA* | IQ (×5 or ×6); RasGAP; Coiled coil | RasGAP | Cytosol, actin cortex, leading & trailing | Increased filopodia number, cell speed *rgaA+*: decreased filopod | Binds Rac1 but inactive; GAP active | IQGAP homolog but light chains | (144, 152) |

| Protein | Gene | Architecture | Activity | Localization | Null and Other Phenotypes | Interaction | Notes | Ref. |
|---|---|---|---|---|---|---|---|---|
| | | | | edges | number, cell speed | for RasD | unidentified; lacks CH domain | |
| Arf | *arfA* | Arf GTPase | Regulation of vesicle transport, endocytosis | Membrane, cytosol | CA mutant: decreased filopod number and/or length | | Localizes to centrosomes during mitosis | (153) |
| ArfGAP A | *acapA* | BAR; PH; ArfGAP; Ankyrin (×2) | ArfGAP | Membrane, cytosol, filopodia (not in tips) | Decreased filopodia number & length; slower cell speed *acapA+*: increased filopodia number & length | ArfA | | (153, 154) |
| SecG | *secG* | Ankyrin (×15); Sec7; PH | ArfGEF | n.d. | *secG+*: high basal F-actin in polarized cells, 'spiky' appearance | | | (155) |
| Rap1 | *rapA* | Rap GTPase | Regulation of adhesion proteins | Plasma membrane, ER and Golgi | CA mutant: increased cell-substrate adhesion; CI mutant: Decreased adhesion | TalB Phg2 | | (156–159) |
| RapGAP9 | *rapgap9* | | RapGAP | Unclear | Increased filopodia number and F-actin, increased cell-substrate adhesion | Rap1 | | (160) |

| Protein | Gene | Architecture | Activity | Localization | Null and Other Phenotypes | Interaction | Notes | Ref. |
|---|---|---|---|---|---|---|---|---|
| **Cell Adhesion Proteins** | | | | | | | | |
| Talin A | *talA* | FERM | Links cell-substrate adhesions to actin | Filopodia tip, actin cortex, cytosol | Decreased cell-substrate adhesion, decreased particle adhesion and phagocytosis, cytokinesis defect, wt filopod number | DdMyo7 | Myo7 binds and stabilizes in cell lysates; large decrease in *myo7*$^{-}$ cells | (161–164) |
| Paxillin B | *paxB* | LD (×4)<br>LIM (×4) | Maturation of cell-substrate adhesions | Filopodia; adhesion sites; cytosol | Decreased cell-substrate adhesion, morphogenesis and development defects | Phospho-lipase D | | (165–167) |
| FrmA | *frmA* | FERM (×2) | Turnover / detachment of adhesions | Filopodia tip; adhesion sites; cytosol | Increased cell spreading, failure to detach from substrate | | | (168) |
| **Actin-Binding Proteins** | | | | | | | | |
| ABP-34 | *abpB* | EF-Hand; unique actin binding domain | Actin cross-linking | Filopodia, pseudopodia, phagocytic cups, cell-cell contacts | Numerous short filopodia (DH1 KO) or long, branched filopodia (Ax2 KO) with defects in detachment; increased migration persistence | | Ca2+-sensitive; Short filopodia in *fimA*$^{-}$/*abpB*$^{-}$; normal phagocytosis | (169–173) |

| Protein | Gene | Architecture | Activity | Localization | Null and Other Phenotypes | Interaction | Notes | Ref. |
|---|---|---|---|---|---|---|---|---|
| EF-1α | *efaA1* | | Actin bundling; protein translation | Filopodia, actin cortex, cytosol | | | Known as ABP-50 in older literature | (174–176) |
| Actobindin | *abnA-C* | WH2-WH2 | Actin binding | Actin cortex, enriched at base of filopodia in *A. castellanii* | Unknown | | *abnC* is a duplicate of *abnB* | (177, 178) |
| Capping protein | *acpA,B* | | Barbed-end actin capping | | Hypomorph: numerous short filopodia; cells stationary in mounds | | Heterodimeric complex | (37, 179) |
| Profilin I/II | *proA, B* | | G-actin binding | | Decreased filopod number and length | Dia2 (Profilin II) | | (131) |

| Protein | Gene | Architecture | Activity | Localization | Null and Other Phenotypes | Interaction | Notes | Ref. |
|---|---|---|---|---|---|---|---|---|
| Kinases | | | | | | | | |
| PakD | *pakD* | CH; CRIB; Ser/Thr kinase | Ser/Thr Kinase | Actin cortex, plasma membrane | Decreased filopodia number, decreased cAMP-stimulated F-actin response | | | (180) |
| Phg2 | *phg2* | Ras-binding domain; Ser/Thr kinase | Ser/Thr kinase | Actin cortex, plasma membrane | KAx3 KO: Increased filopod number, F-actin, increased adhesion; DH1 KO: loss of filopodia but not adhesion | Rap1; Ras-binding required to rescue filopodia | KAx3 KO: *increased* adhesion; DH1 KO: *decreased* adhesion (glass) | (156, 159, 181, 182) |

# 2 MyTH4-FERM Myosins Have an Ancient and Conserved Role in Filopodia Formation[1]

## 2.1 Chapter Summary

The formation of filopodia in Metazoa and Amoebozoa requires the activity of Myo10 in mammalian cells and DdMyo7 in the social amoeba *Dictyostelium*. However, the exact role(s) of these MyTH4-FERM myosins (MF; **m**yosin **t**ail **h**omology 4 - band **4**.1, **e**zrin, **r**adixin, **m**oesin) in initiation and elongation of filopodia are not well defined and may reflect conserved functions among phylogenetically diverse MF myosins. Phylogenetic analysis of myosin MF domains suggests a single ancestral MF myosin existed with a structure similar to DdMyo7, that has two MF domains, and subsequent duplications in the Metazoan lineage produced its functional homologue Myo10. The essential functional features of the DdMyo7 myosin were identified using quantitative live cell imaging to characterize the ability of various mutants to rescue filopod formation in *myo7* null cells. The two MF domains were found to function redundantly in filopod formation with the C-terminal FERM domain regulating both the number of filopodia and their elongation

[1] Reprinted from: K.J. Petersen, H.V. Goodson, A.L. Arthur, G.W.G. Luxton, A. Houdusse, M.A. Titus, MyTH4-FERM myosins have an ancient and conserved role in filopod formation, PNAS. (2016) 201615392. doi:10.1073/pnas.1615392113.

velocity. DdMyo7 mutants consisting solely of the motor plus a single MyTH4 domain were found to be capable of rescuing formation of filopodia, establishing the minimal elements necessary for the function of this myosin. Interestingly, a chimeric myosin with the Myo10 MF domain fused to the DdMyo7 motor was also capable of rescuing filopod formation in the *myo7* null, supporting fundamental functional conservation between these two distant myosins. Together, these findings reveal that MF myosins have an ancient and conserved role in filopod formation.

## 2.2 Introduction

Cells interact with their environment through protrusions such as filopodia that form in response to extracellular cues and mediate initial contact with the substrate. Filopodia are slender actin-filled membrane projections that are highly dynamic, growing and shrinking from peripheral regions of cells, such as lamellipodia and the dorsal surface (183). A wide variety of cell types including amoebae such as *Dictyostelium discoideum* (114) and *Acanthamoeba* (184), as well as mammalian vascular endothelial cells (185), and developing neurons (186) extend filopodia. These are typically 1 – 10 μm long and 0.1 – 0.3 μm in diameter, are made of a core of 10 – 30 parallel actin filaments with a protein-rich complex at their tip (183, 187, 188). Modified forms of filopodia such as dendritic spines, cytonemes, and tunneling nanotubes promote intercellular communication during multicellular development (189–191). Defects in filopod formation alter cell spreading and adhesion (114, 115, 192), whereas overproduction of filopodia or filopodia-like protrusions is associated with increased invasiveness of metastatic cancer cells (193–195).

Filopod elongation is triggered by small GTPase activity (142, 183) and driven by the activity of actin elongation factors including VASP and formins, while the actin core is stabilized by actin cross-linking proteins (183). A MyTH4-FERM (MF; myosin **t**ail **h**omology **4** - band **4**.1, **e**zrin, **r**adixin, **m**oesin) myosin motor is also required. A broad survey of genomes reveals that these essential filopodial proteins are evolutionarily conserved between Holozoa (a group that includes Metazoa and their closest single-cell relatives such as the choanoflagellate *Monosiga brevicollis*) as well as Amoebozoa (196). The existence of a shared, core filopodial machinery suggests that diverse organisms may employ fundamentally conserved means of generating filopodia.

Organisms in a range of species have been reported to make filopodia or filopodia-like protrusions, but little is known about how these structures are generated by non-Metazoan eukaryotes (196). Amoebozoa share a common ancestor with animals and fungi (197), thus making *Dictyostelium* an excellent model system to test mechanistic conservation and diversity of these structures over evolutionary time (nearly a billion years of independent evolution). Several proteins important for filopod formation in Metazoa are conserved with similar roles in *Dictyostelium*. The widely conserved actin regulator VASP and the MF myosin DdMyo7 have critical roles in filopod initiation and the formin Dia2 is required for filopod elongation (114, 115, 131). While *Dictyostelium* lack the key Metazoan small GTPase Cdc42, the related GTPase Rac1a plays an analogous role in stimulating filopod formation (142). Instead of the Metazoan actin cross-linking protein fascin (198) the actin binding proteins ABP-34 and EF-1α are believed to play a role in actin cross-linking in

*Dictyostelium* filopodia (199). The different actin cross-linking proteins used in *Dictyostelium* likely give rise to the less organized, shorter actin filaments in their filopodia (187). Despite these differences, the abundance of structural and genetic similarities argues that filopod formation is a conserved cell biological process in Metazoa and Amoebozoa.

Two different MF myosins have been found to be essential for filopodia formation in widely divergent organisms, Myo10 in vertebrates and DdMyo7 in the social amoeba *Dictyostelium* (112, 114). These two phylogenetically distant MF myosins have several features in common (Fig. 4B). They both have a number of light-chain binding sites (IQ motifs), an SAH domain (single α-helix) (200) and a C-terminal MF domain. Like several MF myosins, such as the Myo7 from humans or flies, DdMyo7 differs from Myo10 in having a second MF domain and an SH3 (src homology 3) domain inserted before the C-terminal MF domain that is characteristic of this group of myosins. In contrast to DdMyo7, the tail of Myo10 (Fig. 4B) has PH (pleckstrin homology) domains in place of the internal MF and SH3 domains (201). Despite these differences in overall structure, the *myo7* null *Dictyostelium* and HeLa or breast cancer cells with reduced Myo10 expression both exhibit a striking lack of filopodia (112, 114). The findings suggest that these two distinct MF myosins have functionally equivalent roles in filopod formation, one that has been conserved through almost a billion years of independent evolution. However, the phylogenetic relationship between Myo10 and DdMyo7 is unresolved and it is unclear how these two motors cooperate with their respective cohorts of filopodial proteins to build filopodia. DdMyo7 has been classified as either a Myo7, a Myo22, a Myo25, or could not

be classified (28, 29, 114, 202) (see also cymobase.org). The uncertainty about the relationship between the Metazoan and Amoebozoan MF myosins and the differences in actin organization seen between *Dictyostelium* and mammalian filopodia raises the question whether Metazoan Myo10 and Amoebozoan DdMyo7 myosins contribute to filopod formation in a similar way, and whether their activities are conserved or specific to each organism. In other words, do the filopodial MF myosins DdMyo7 and Myo10 possess convergent yet distinct functions in filopodia or do they share a conserved role in filopod formation despite their structural and phylogenetic differences? A functional dissection of the *Dictyostelium* MF myosin, DdMyo7, has been undertaken to begin to address this question.

## 2.3 Results

Deeper understanding of the role of DdMyo7 during filopod formation is needed to uncover functionally conserved and specific roles of MF myosins, particularly in comparison to Myo10's role in filopod formation. Thus, a detailed characterization of DdMyo7 function *in vivo* was undertaken. A phylogenetic reassessment of MF myosins was also conducted to determine if the Amoebozoan Myo7s are indeed direct orthologs of any of the Metazoan MF myosins, or if they are a functionally distinct class of MF myosins that arose from a common ancestor.

### 2.3.1 Phylogenetic Relationship Between DdMyo7 and Metazoan Myosins

The evolutionary time (~600 million years; (203)) between Amoebozoa and Metazoa raises the question of how DdMyo7 differs from Metazoan Myo10 given their common role in filopod formation. The relationship between these MF myosins was unclear in previous studies of myosin diversity based on a comparison of motor domain sequences (29, 202) (see also cymobase.org). A phylogenetic analysis of the MF myosins using their defining feature, the C-terminal MyTH4-FERM domain, was thus conducted to better resolve their relationships. Full-length MF myosin sequences were gathered from representative organisms across all eukaryotes known to possess MF myosins. A total of 162 sequences from 58 distinct species were used for this analysis, including the Metazoan MF myosins (Myo7, 10, 15, and 22), fungal and choanoflagellate Myo22, and the Amoebozoan MF myosins. Sequences for additional MF myosins including Myo32 were

gathered from the SAR clade (Stramenopiles, Alveolates and Rhizaria), a branch of unicellular eukaryotes which includes ciliates such as *Tetrahymena* and oomycetes such as the pathogenic water mold *Phytophthora* (85). Phylogenetic relationships between the 162 C-terminal MF domain sequences were derived using SATé (204).

The resulting phylogenetic tree (Fig. 4A) shows that the Amoebozoan MF myosins form a single family with two myosin classes. The Amoebozoan Myo7 (named for its structural resemblance to the animal Myo7) is found in social amoebae as well as solitary species such as *Acanthamoeba.* DdMyo7 (also known as MyoI) is the best-characterized example of this class. A second class of myosin present in social amoebae, Myo44 (*Dictyostelium* MyoG), does not play a role in filopodia but has novel functions in chemotactic signaling (97). The Amoebozoan MF myosins are distinguished with high confidence from the Holozoan Myo7, Myo10 and Myo22 protein families and branch in a poorly defined region near the center of the tree, close to the presumptive root in the SAR group (Fig. 4A). The topology of the tree suggests that the common ancestor of these organisms contained a single MF myosin. Comparison of the domain organization of the myosins on each branch (Fig. 4B, C) reveals a common structure for the DdMyo7, Myo22, and Holozoan Myo7 proteins, each possessing a motor domain and tail region that contains three domains (two MF and one SH3 domains), but lacking PH domains. The tree suggests that the ancestral MF myosin underwent duplication after the emergence of the Amoebozoa, resulting in the proteins that established the Myo10/22 and Myo7/15 branches (Fig. 4A). The striking similarity in tail structure between DdMyo7, Myo22 and Myo7

suggests that these proteins have the ancestral tail structure. Amoebozoan MF myosins are exemplified by DdMyo7, which is structurally dissimilar to Myo10 yet similar in function, suggesting that core molecular features needed for filopod formation will be present in both DdMyo7 and Myo10.

### 2.3.2 DdMyo7 is Present in Filopodia and Required for Their Formation

Filopodia are a common feature of *Dictyostelium* cells from the vegetative phase through early development (114). Wild type *Dictyostelium* frequently display multiple filopodia (Fig. 5A), which appear as slender membrane projections that actively extend from the cell body close to the substrate, while *myo7* null cells display virtually none (Fig. 5A). Filopod formation was rescued by expression of full-length GFP-tagged DdMyo7 (Fig. 6; referred to as DdMyo7 hereafter). Spinning disk confocal microscopy showed DdMyo7 localized to the actin cortex of an active leading edge (Fig. 5B), in filopodia tips, and in the cytosol, as previously reported (114, 161).

Filopod initiation events were monitored in cells co-expressing DdMyo7 and RFP-LifeAct to visualize actin filaments (122). DdMyo7 is present in the cytosol and in a typical initiation event, it was seen to become concentrated at the cortex (Fig. 5C). Then, a bright spot of myosin appeared, projecting from an actin-rich pseudopod. Filopodia elongated several micrometers within seven seconds, with actin present along the length and DdMyo7 concentrated close to the filopod tip all throughout the elongation process (Fig. 5C). These results show that filopod initiation is a highly dynamic and rapid process.

Filopod formation activity was measured in a live cell assay by counting the number of filopodia per cell following 1 hour of starvation, a condition that consistently stimulates production of filopodia in wild type *Dictyostelium.* Arbitrary fields of view were selected for imaging by DIC and confocal GFP fluorescence. Blinded manual analysis demonstrated there is a low frequency of filopodia-like protrusions in *myo7* null cells (Fig. 7; Table 5) and that expression of DdMyo7 rescues filopod formation. DdMyo7 fluorescence was distinctly observed at the tips of protrusions while GFP alone did not label protrusions (Fig. 8). Thus, although DIC imaging could not resolve filopodia from other types of protrusions such as ruffles or retraction fibers, DdMyo7 localization at the tip identified the protrusions as filopodia. Automated image analysis was used to measure the number and length of filopodia (Fig. 5D). Filopod number in cells expressing DdMyo7 was not significantly different in wild type compared with rescued *myo7* null cells (2.8 ± 0.4 filopodia/cell). The establishment of a quantitative assay for DdMyo7-based filopod formation allowed for an in-depth examination of the molecular requirements for this MF myosin in filopod formation.

### 2.3.3 Complementary Roles of the DdMyo7 Head and Tail in Filopod Initiation

The motor activity of Myo10 may be sufficient for filopod formation as expression of truncated dimeric Myo10 motors was reported to induce filopodia in mammalian cells (205). The question of whether the DdMyo7 motor domain is necessary or sufficient for filopod initiation was tested with a series of mutants. Expression plasmids encoding DdMyo7 mutant proteins were transformed into wild type cells as well as into *myo7* null

cells (to assay their effect on filopod formation). Transformants were screened for GFP fluorescence and expression was confirmed by western blot (Fig. 6). The role of the motor domain was tested with two tailless mutants encompassing the motor domain and a putative lever arm region consisting of 4 light-chain binding IQ motifs, SAH (single α-helix), and an uncharacterized sequence potentially extending the lever arm ("motor-SAH"; aa 1-1020) or this region plus the first proline-rich region ("motor-Pro1"; aa 1-1115) (Fig. 9A). Tailless mutants displayed diffuse cytosolic localization in both wild type and *myo7* null cells (Fig. 9A, B), did not associate with pseudopodia, and did not rescue filopod formation in *myo7* null cells. The longer motor-Pro1, in contrast to motor-SAH, did localize to filopod tips in wild type cells, suggesting that the Pro1 region may aid motor processivity necessary for DdMyo7 to reach filopod tips. A headless mutant comprised of the SAH and the full tail region was strongly enriched in pseudopodia of both wild type and *myo7* null cells, yet failed to rescue filopodia in *myo7* null cells (Fig. 9C). Localization of the headless mutant to filopod tips was variable in WT cells with DdMyo7 Tail either not reaching the tip (Fig. 9C) or being weakly enriched there (Fig. 10B). These observations establish that the tail region is required for localization of DdMyo7 to the cortical region, possibly through binding to a cortical or membrane associated partner, and that the motor domain is required to target DdMyo7 to filopod tips and/or retain DdMyo7 at the tip of an elongating filopod. Thus, both the motor and tail are required for filopod formation.

### 2.3.4 Functional Redundancy of DdMyo7 FERM Domains

The role of the dual MF domains in DdMyo7 was examined by analysis of the tail

region of this myosin. The MF domains form a compact supramodule and in the case of mammalian Myo7A MF1, the SH3 domain is coupled to the FERM domain (102, 206). FERM domains interact with MF myosin cargo proteins, including adhesion and signaling receptors, and can also mediate autoinhibition of the motor (201). Therefore, removal of an MF domain was predicted to affect DdMyo7 function. As with the headless and tailless mutants, DdMyo7 deletion mutants (Fig. 11A) were expressed in either wild type or *myo7* null cells. The number of filopodia per cell, their length, and elongation velocity were measured for those mutants that generate filopodia to determine which aspect of filopod formation was altered due to domain deletion.

The contribution of the internal MF domain was examined with a DdMyo7 ΔMF1-SH3 mutant that is stably expressed and rescues filopod formation in *myo7* null cells (Fig. 11A; Fig. 6). The ΔMF1-SH3 mutant localizes to both the leading edge and the tips of extending filopodia in wild type and *myo7* null cells (Fig. 11A, B). Wild type or *myo7* null cells expressing either the ΔMF1-SH3 mutant or full-length DdMyo7 produce similar numbers of filopodia (Fig. 12;

Table 6) although the average length of filopodia in *myo7* null cells expressing ΔMF1-SH3 was reduced by 20% (Fig. 13;

Table 6). Smaller deletions encompassing only the MF1 or FERM1 domains (ΔMF1 and ΔFERM1(f1, f2)) also did not affect the ability of DdMyo7 to promote filopod formation (Fig. 14). Similarly, a deletion mutant targeting MF2 also rescued filopod

formation in *myo7* null cells (Fig. 14). Thus, the MF domains appear to function redundantly with a single MF domain, either MF1 or MF2, being essential for the filopod formation activity of this myosin.

Loss of filopodia is correlated with reduction in cell substrate adhesion in the *myo7* null cells as well in HeLa cells that have reduced levels of Myo10 (112, 114). The ability of the DdMyo7 FERM deletion mutants to rescue the *myo7* null adhesion phenotype was assessed in polarized migrating cells by interference reflection microscopy (IRM) (207). Null cells expressing DdMyo7 exhibited improved adhesion to the substrate identical to wild type control cells, while the ΔMF1-SH3, ΔFERM2, and KKAA (see below) mutants also showed evidence of rescued adhesion (Fig. 15; Fig. 16). While there is a slight reduction of adhesion measured for the DdMyo7 mutants compared to the wild type rescue, the differences are not significant. These results are consistent with the finding that the two MF domains are functionally redundant.

### 2.3.4 DdMyo7 FERM2 Domain Regulates Filopod Formation and Elongation

MF myosins have been shown to be autoinhibited, with the C-terminal MF domain serving to regulate the *in vitro* and *in vivo* activities of fly and human Myo7A as well as mammalian Myo10 (208–211). In Myo10, PH domains and the FERM domain are required for autoinhibition that is relieved by phospholipid binding to PH domains (210). In Myo7A, a basic motif (K/RxxK/R) in FERM2 is critical for autoinhibition (208, 211), consistent with an intramolecular head-tail interaction. This regulatory basic motif is highly

conserved in Holozoan Myo7 and Myo22 and is also present in DdMyo7 (Fig. 11C), suggesting that DdMyo7 may also be subject to autoinhibition.

The potential role of the DdMyo7 C-terminal FERM domain in controlling *in vivo* filopod formation activity was tested with two mutants of DdMyo7. The first mutant, ΔFERM2, deleted the C-terminal FERM domain implicated in regulation of Myo7A and Myo10 and interaction with signaling and adhesion receptors (209, 210). The second mutant, KKAA, targeted two highly conserved basic residues in the FERM2 domain (Fig. 11C) implicated in autoinhibition of *Drosophila* and human Myo7A (208, 211). The GFP-tagged mutant DdMyo7 proteins were expressed in cells (Fig. 6) and analyzed by confocal microscopy. Both mutants localized to filopodia tips in wild type cells and rescued filopod formation in *myo7* null cells (Fig. 11A) with characteristic leading edge concentration preceding filopod elongation (Fig. 11B). In the rescued cells, the DdMyo7 protein was highly concentrated at the tip and on average uniformly distributed along the shaft of the filopod, though less abundant (about 20% relative to fluorescence at the tip) (Fig. 10C, D). Wild type and mutant DdMyo7 appeared locally enriched at the cortical actin/membrane interface visualized by the membrane stain FM 4-64 (Fig. 8), consistent with a subcellular fractionation study of DdMyo7 (164). Furthermore, cortical enrichment at nascent filopod tips during initiation appears similar among ΔFERM2 and KKAA mutants and the wild type DdMyo7.

Quantification of filopodia formation in wild type cells expressing the DdMyo7 ΔFERM2 mutant showed that the number of filopodia formed was not significantly

different than full-length DdMyo7 when expressed in wild type cells (Fig. 12;

Table 6). However, filopod number was increased by 35% ($p$ = .04) in *myo7* null cells expressing DdMyo7 ΔFERM2 (3.8 ± 0.4 filopodia/cell), suggesting that the FERM2 domain negatively regulates filopod formation.

Expression of the DdMyo7 KKAA mutant resulted in a large increase in the number of filopodia formed per cell in either wild type or *myo7* null cells, which had 4.4 ± 0.6 and 4.8 ± 0.3 filopodia/cell respectively (Fig. 12;

Table 6). Overall, the KKAA mutant significantly increased filopod number by 66% with respect to full-length DdMyo7 ($p$ = .00008) and 36% with respect to the ΔFERM2 mutant ($p$ = .003) with similar results for both WT and KO cells (

Table 6). The KKAA mutant exhibited localization similar to the wild type DdMyo7 (Fig. 11A), suggesting that the conserved basic motif is not essential for activation or recruitment of DdMyo7 at the membrane. These data are consistent with inhibition of DdMyo7 motor activity by the FERM2 domain whereas relief of autoinhibition in the KKAA and ΔFERM2 mutants results in increased filopod formation activity. The increased activity of the KKAA mutant compared with ΔFERM2 and ΔMF1-SH3 mutants may indicate that both MF domains are needed for maximal filopod formation activity. The membrane recruitment of DdMyo7 likely depends upon additional, as yet unknown factors.

Overexpression of Myo10 in mammalian endothelial cells increases both filopod

length as well as number (212) and it has been proposed that the Myo10 dimer plays a role in filopod initiation as well as elongation (201). To test whether the tail domains of DdMyo7 regulate filopod elongation, filopod length was measured in cells expressing DdMyo7 as described above (Fig. 5D). The average filopod length for wild type cells expressing DdMyo7 was 2.6 ± 0.3 μm, similar to the length observed for *myo7* null cells expressing the same protein, 2.9 ± 0.2 μm (Fig. 13). The average filopod length did not differ significantly between WT or *myo7* null cells expressing full-length DdMyo7 and those expressing ΔFERM2 or KKAA mutants (

Table 6). Time-lapse kymograph analysis was performed to further characterize filopod elongation in cells expressing these mutant DdMyo7 proteins. Filopod elongation events were analyzed using DdMyo7 fluorescence at the filopod tip to determine elongation velocity (Fig. 17). A nearly constant slope was found in the kymographs (Fig. 17B), allowing the velocity to be measured with linear regression. The average velocity for *myo7* null cells expressing DdMyo7 was 0.40 ± 0.03 μm $s^{-1}$ (Fig. 17C;

Table 6) and was not significantly altered in the ΔMF1-SH3 or KKAA mutants. Moreover, no apparent difference in filopod length was measured after expression of the KKAA mutant compared to DdMyo7 despite the observed increase in filopod number (Fig. 12B; Fig. 13B). In contrast, the velocity of filopod elongation in cells expressing the ΔFERM2 mutant decreased 28% relative to DdMyo7 to 0.28 ± 0.01 μm $s^{-1}$. The decrease in elongation velocity was significant compared to full-length DdMyo7 ($p$ = .002; Tukey test). Taken together, these data support a role for the DdMyo7 FERM2 domain in

promoting filopod elongation in a manner that is independent of the KKAA motif.

### 2.3.5 A Minimal Filopod Motor

The expression of a minimal DdMyo7 motor region (motor-Pro1) produces virtually no filopodia in *myo7* null cells, despite being localized at filopod tips in wild type cells (Fig. 9B; Fig. 7; Table 5). Thus, the motor-Pro1 was augmented with a MyTH4-FERM or MyTH4 domain added to the C-terminus (Fig. 18B). Initial attempts to express a motor-Pro1-MF1 protein were unsuccessful, perhaps due to disruption of the MF1-SH3 supramodule (206). Instead, a motor-Pro1-MF1-SH3 protein (i.e., GFP-DdMyo7 truncated at the C-terminus of the SH3 domain) was expressed in *myo7* null cells (Fig. 18B; Fig. 6C). Filopodia were observed in GFP-positive cells with characteristic tip localization of the GFP fusion protein. Filopod length was comparable to that seen for DdMyo7 (Fig. 18C;

Table 6) with an average of 2.8 ± 0.6 filopodia per cell observed during time lapse imaging. A fusion protein encoding motor-Pro1-MF2, with the MF2 domain taking the place of MF1-SH3, was tested with similar results (Fig. 18C). The large number of filopodia observed upon expression of motor-Pro1-MF1-SH3 and motor-Pro1-MF2 in *myo7* null cells suggests that both the SH3 and the second proline-rich domain (aa 1685-1830, Fig. 18A) are dispensable in filopod formation, while at least one MF domain is required.

The ability to rescue filopod initiation conferred by the single MF motors strongly implies that the MF domain plays roles in targeting of the DdMyo7 motor to the cortex and

in the initiation of filopodia. The requirement for a FERM domain was further tested with motor-Pro1-MyTH4a protein, where the tail contains solely the internal MyTH4 domain. Filopod formation was rescued by motor-Pro1-MyTH4a despite the lack of a FERM domain (Fig. 18B). However, the number of filopodia was notably reduced compared to motor-Pro1-MF2 (Fig. 18D) while the average filopod length (Fig. 18C; Table 7) was again similar to the DdMyo7 rescue. While myosin motor activity is critical for filopod initiation, the ability of motor-Pro1-MyTH4a to promote filopod formation could be explained by interactions of MyTH4a with yet unidentified target proteins and/or conformational stability provided by the globular MyTH4 domain, favoring recruitment, clustering of myosin motors or dimerization of the extended lever arm and post-lever arm region (213). Substitution of mCherry for MyTH4a did not support filopod formation (Fig. 18E), demonstrating that the mere presence of a globular domain (mCherry) at the C-terminus is not sufficient for the assembly or recruitment of an active motor to promote filopodia at the plasma membrane. This analysis of DdMyo7 establishes that the minimal elements required for filopodial activity are a motor domain, lever arm, and a MyTH4 domain. The supramodular MyTH4-FERM domain confers optimal function to the myosin, likely by allowing it to interact with partners that promote growth of filopodia.

### 2.3.6 Functional Conservation of MF Domains Across Kingdoms

MyTH4-FERM myosins are required for filopod formation in humans (112) and amoebae (114). The strong morphological and genetic parallels between these distantly related proteins suggest that divergent MF myosins have conserved roles in filopodia

formation. Several attempts to express GFP-tagged bovine Myo10 (212) in *Dictyostelium* to test this possibility were unsuccessful, most likely due to the difficulty of cross-kingdom gene expression. However, the identification of MF2 as a minimal tail domain supporting robust filopod formation raised the question of whether the common MF domain from the evolutionarily distant Myo10 might be able to functionally substitute for the DdMyo7 MF domain. This possibility was tested using a DdMyo7 motor-Pro1-HsMyo10 MF domain chimera (Fig. 18B) that localized to filopodia in wild type cells (Fig. 19). The Myo10MF chimera rescued filopodia formation in *myo7* null cells, averaging 2.2 ± 0.2 filopodia per cell (Fig. 18D; Table 8). However, the extent of rescue was less than with motor-Pro1-MF2 (4.0 ± 0.1), but was comparable to the motor-Pro1-MyTH4a (1.8 ± 0.2 filopodia per cell). A chimeric protein with a Myo10 MyTH4 tail (motor-Pro1-HsMyo10MyTH4) localized to filopodia in wild type cells (Fig. 19), but did not stimulate filopodia formation (Fig. 18D; Table 8). These results reveal that there is functional conservation between filopodial MF domains, most likely due to shared features of the FERM domains of the human Myo10 and DdMyo7 MF domains.

Only a subset of MF myosins have a role in filopodia formation. Others such as HsMyo7A and HsMyo7B function as transporters and anchors in stereocilia and microvilli, respectively (64, 208, 214), raising the question of whether there are features specific to filopodial MF domains or if an MF domain from a non-filopodial myosin can also functionally substitute for the DdMyo7 MF domain. *Dictyostelium* expresses a second MF myosin with two MF domains, Myo44 (MyoG), that is essential for chemotactic signaling

but not required for filopodia formation (97). The MF2 domain of Myo44 was fused to DdMyo7 motor-Pro1 and the resulting chimera expressed in wild type and *myo7* null cells. Interestingly, the motor-Pro1-Myo44MF2 chimera expressed in *myo7* null cells failed to rescue the filopodia defect (Table 8) and only weakly localized to filopodia in wild type cells (Fig. 19), revealing that there are intrinsic, conserved features of the filopodial MF domain required for its role in filopodia formation.

## 2.4 Discussion

Filopodia or filopodia-like protrusions are produced by a range of cell types in a diverse array of eukaryotic organisms, raising the question of whether these protrusions are formed by a core conserved mechanism or the emergence of independent pathways throughout phylogeny created multiple mechanisms of formation (196). Comparison of filopodia formation in Metazoa and Amoebozoa, groups that have been evolving independently for hundreds of millions of years (203), reveals that filopodia formation requires the same shared core set of filopodial proteins in these two branches of the phylogenetic tree. Specifically, several mammalian proteins essential for filopod formation either have direct orthologs (VASP (115) and Dia2 (131)) or functional homologs in *Dictyostelium* (e.g., Rac1a (142)); furthermore, mammalian cells and *Dictyostelium* both absolutely require the activity of a specialized MyTH4-FERM myosin (112, 114). Analysis of a series of DdMyo7 mutants and chimeras reveals that the important features of the DdMyo7 and Myo10 required for filopod formation are evolutionarily conserved. The results indicate that a functional filopodial MF myosin in Metazoa and Amoebozoa consists of its motor domain, an extended lever arm and short post-lever arm region that may be involved in dimerization, and an MF domain (Fig. 18).

### 2.4.1 Evolution of MF myosins

The MF myosin responsible for filopod formation in vertebrates, Myo10, is phylogenetically distinct from the *Dictyostelium* MF myosin DdMyo7 (Fig. 4). Attempts

to classify DdMyo7 in relation to other myosin motor domain sequences have yielded conflicting results (29, 202). The new molecular phylogenetic analysis focusing on the common MF domain (Fig. 4) reveals that Amoebozoan MF myosins are an evolutionarily distinct class of motor proteins. DdMyo7 fails to group with the animal MF myosin classes, most likely because the gene duplications that produced these proteins occurred after the split between the Amoebozoa and Holozoa, over 600 million years ago (203). The analysis suggests that the common ancestor of Amoebozoa, Fungi, and Holozoa contained a myosin that had two MF domains and a tail structure similar to that of DdMyo7. These myosins share many structural similarities (Fig. 4B), including a highly conserved basic motif at the C-terminus of Myo7, Myo22 and Amoebozoan Myo7 (Fig. 11C) essential for autoinhibition of *Drosophila* and human Myo7A (208, 211) and regulation of DdMyo7 activity (Fig. 12). These findings are consistent with DdMyo7 retaining core structural features of the last common ancestral MF myosin.

MF myosins play critical roles in the formation and organization of protrusions containing parallel actin bundles such as filopodia (64, 112, 114), microvilli (214), and stereocilia (215, 216). These myosins may plausibly be seen as conserving a core ancestral function (196). However, the origins of this functional conservation are unclear. Although it is commonly assumed that gene duplications lead to novel functions (i.e., duplicated genes are maintained because one evolves a new adaptive function), a more frequent outcome is that gene duplications lead to partitioning of ancestral functions between the duplicated genes (217, 218). This logic implies that the functions of the ancestral protein

have been partitioned among the various MF myosin classes in Metazoa, such as filopodial versus non-filopodial myosins. Amoebozoan MF myosins, exemplified by DdMyo7, represent a branch preceding the expansion of Holozoan MF myosins on the Myo7/15 and Myo10/22 branches (Fig. 4A). In this view DdMyo7 is not an ortholog of any single animal MF myosin, but potentially is a model for all animal MF myosins.

### 2.4.2 Basic requirements for MF myosin-based regulation of filopod formation.

Filopod formation in both animals and amoebae requires myosin motor activity as well as the MF tail (Fig. 9; (112)). A DdMyo7 motor-lever arm mutant lacking domains following the SAH fails to localize to filopod tips in wild type *Dictyostelium* (Fig. 9A), paralleling results with a Myo10 missing the tail region following the SAH domain that is also not observed in filopodia tips in COS7 cells (205). A longer DdMyo7 protein including a proline-rich domain (motor-Pro1; corresponding to ΔMF1-SH3-Pro2-MF2) localized to filopod tips in wild type without rescuing filopod formation in *myo7* null cells (Fig. 9B), again similar to results in COS7 cells where Myo10 ΔPH-MF or ΔMF mutants properly localized to basal filopodia yet failed to promote formation of dorsal filopodia (112). These results strongly imply that the ability of the motor to localize to filopodia is necessary but not sufficient for their formation. Although a tailless Myo10 was found to stimulate basal filopod formation in COS7 cells when long-lived Myo10 dimers were experimentally induced, these filopodia were short and unstable (205). The results seen with tailless DdMyo7 and Myo10 support the view that filopod initiation proceeds from mechanical re-organization of actin filaments by dimeric MF myosin motors targeted to the cortex, with

elongation requiring both motor activity and the MF tail (either for cargo transport to the tip or to localize myosin activity to the tip).

Functional analysis of the MF tail domain implicates the FERM2 domain in regulating DdMyo7 activity. Deletion of the FERM2 domain results in increased numbers of filopodia that extend at a slower velocity (Figs. 4, 5 & 7). Mutation of a conserved motif in FERM2 (KKAA) also leads to an increase in filopod formation (Fig. 12) but does not affect either filopod length or elongation velocity (Fig. 17; Fig. 13). The observed increase in the activity of the KKAA mutant is reminiscent of what is observed for human Myo7A that is activated both *in vitro* and *in vivo* when the equivalent residues are mutated (208). Furthermore, while ectopic expression of Myo10 in COS7 cells increases filopod length, cells expressing a ΔFERM mutant produce shorter filopodia (212) that extend faster (219). This faster elongation likely results from the release of autoinhibition. Together, these results could be explained in at least two ways. FERM2 could interact with actin polymerization factors such as VASP or Dia2, or regulators of these proteins, to control the velocity of filopod elongation and loss of this domain thus leads to a slower elongation. It might also control myosin activity *in vivo* by autoinhibition of the motor, as has been seen for the Metazoan Myo7A and Myo10 (209–211). This is consistent with a conserved mechanism of DdMyo7 activation by a binding partner, either in the cytosol as with Myo7A (220), or at the plasma membrane. The contrasting effects of deleting the C-terminal FERM domains of DdMyo7 and mammalian Myo10 on filopod length and elongation velocity may potentially be explained by differences in their binding partners

or by the redundancy of DdMyo7 FERM domains as opposed to the single FERM domain of Myo10. Together, these findings support conserved roles for the C-terminal FERM domain regulating MF myosin activity as well as promoting the filopod formation activity of DdMyo7 and Myo10.

### 2.4.2 Minimal and conserved features of MF myosin required for filopod formation.

DdMyo7 proved surprisingly robust to domain deletion, as it was able to rescue filopod formation with either one of the MyTH4-FERM domains (Fig. 11). The motor plus the post-lever arm region (motor-Pro1) itself is not sufficient to generate filopodia (Fig. 7; Table 5). However, addition of either the MF1-SH3 or MF2 domains to the motor imparted full functionality. Consistent with this finding, Myo10 lacking the MF domain does not promote the formation of dorsal filopodia in COS7 cells (112). A minimal DdMyo7 motor fused to the MyTH4 domain alone can promote filopodia formation, but this activity is significantly augmented by the presence of the adjacent FERM domain (Fig. 18D; Table 8). The apparent congruence of Amoebozoan and Metazoan MF myosins suggested a chimeric approach to testing their relationship. DdMyo7 motor-Pro1 fused to the human Myo10 MF domain (Fig. 18B-D) does rescue filopodia formation in the *myo7* null mutant, albeit with reduced efficiency, with localization and filopod length comparable to native DdMyo7 (Fig. 18; Table 7; Table 8). This suggests that the Myo10 MF domain retains enough homology with DdMyo7 to function as a tail domain for filopod formation and that the MF domains of human and amoeboid filopodial myosins interact with conserved or analogous binding partners that mediate their role in stimulating filopod formation. Failure

of the DdMyo7 motor-Pro1-Myo44 MF2 chimera to rescue filopodia formation establishes that MF domains are specific for the function of a particular MF myosin and that special features not found in Myo44 MF must be present in a MF domain for it to contribute to filopodia formation. In contrast, Myo10 and DdMyo7 MF must have conserved such features, although it is unclear whether this involves the ability to recognize a common partner; Myo10 and DdMyo7 are not known to have any binding partners in common. The MF domain itself may be important for activation of the myosin or dimerization, possibly through interaction with a conserved partner that is yet to be identified. The DdMyo7 MyTH4a alone is sufficient to promote some filopodia forming activity, but not as robustly as the full MF, and the Myo10 MyTH4 alone cannot substitute for this domain (Fig. 18B-D). This may be due to loss of stability of the MF domain when the supramodule is disrupted by deletion of the FERM. This supramodule is critical to coordinate how partners bind to the MF domain and the structures of the Myo10 and DdMyo7 MyTH4 (36, 56) establish how divergent their binding surfaces are, consistent with a lack of significant sequence conservation (only 24% identical and 40% similar). Thus, the absence of the FERM compromises the MyTH4 function and the Myo10 MyTH4 alone appears to be too divergent to even minimally substitute. Future studies of specific surface mutations and their impact on the interaction with partners will be required to elucidate the role(s) of the MF supramodule in filopodia formation activity.

### 2.4.3 Conclusions

Evolutionarily distant MF myosins with essential roles in filopod formation have

several core features in common, indicating that their activity is not an example of convergent evolution but rather reveals a high degree of functional conservation between these motor proteins. The motor domains and post-lever arm regions of the Amoebozoan DdMyo7 and Metazoan Myo10 are essential for *in vivo* activity, and the tail domains play critical roles in the activity of these myosins. Filopod formation activity minimally requires a MyTH4-FERM supramodule specific to filopodial MF myosins that imparts optimal activity as well as regulation of filopod elongation (Fig. 18); however, the exact role of the MF domain in filopod formation remains to be clarified. FERM domains interact variously with membrane receptors, actin filaments and other binding partners (102) that may work in concert with filopodial MF myosins to promote formation of filopodia, but the specific interactions have not been identified. Additionally, the exact contribution of the motor during the different stages of filopod formation, especially the initiation step, remains to be clarified. It appears that the length and flexibility of the lever arms is critical (205) but how the motor might organize actin at the cortex and/or support transport along cortical actin to promote filopod formation is still unclear. Another intriguing question is what specific features confer filopod formation activity on an MF myosin. While the Metazoan Myo7 and *Dictyostelium* Myo44 have all of the essential domains required for filopod formation, including a C-terminal MF domain, they do not support filopod formation (97, 220). Future studies using *Dictyostelium* as an ancestral MF myosin model system will address these fundamental questions and provide further insight into the evolutionary conservation of MF myosin function.

## 2.5 Methods

### Cell Culture

Wild type *Dictyostelium* Ax2 cells and wild type control (G1-21) and *myo7* null (HTD17-1) (2) Ax3 cells were grown at 21˚ C on bacteriological plastic plates in HL5 glucose medium (ForMedium) supplemented with 10 kU/mL penicillin G and 10 µg/mL streptomycin sulfate (Sigma). Null cells were periodically selected in 10 µg/mL blasticidin S (Calbiochem). Cells were transformed by electroporation then selected and maintained using 20 µg/mL G418 (for neomycin resistance) (Fisher Scientific) or 50 µg/mL hygromycin B (Gold Biotechnology).

### Plasmid Design and Expression

An integrating expression plasmid for the N-terminal GFP-tagged DdMyo7 full-length myosin, pDTi74, and the extrachromosomal GFP-Myo7 and GFP-Myo7 Tail plasmids have been described previously (114, 164). Standard molecular biological methods were used to generate mutant expression plasmids in the integrating pDTi74 background. Enzymes were obtained from New England Biolabs and the sequences of all PCR-generated DNAs were verified by sequencing (University of Minnesota Genomics Center). RFP-tagged Lifeact in pDM358 (122) was a gift from Hanna Brzeska (Laboratory of Cell Biology, NHLBI, NIH).

### Microscopy

Epifluorescence and IRM microscopy experiments were performed on a Zeiss Axiovert 200 equipped with a 63X Ph3 Plan Apo (NA 1.4) objective and Spot RT camera (SPOT Diagnostics). Confocal microscopy was performed with 63X and 100X Plan Apo oil immersion objectives (NA 1.4) on a Marianas Spinning Disk Confocal imaging system based on a Zeiss Axiovert equipped with a Yokogawa CSU-X1, a Photometrics Evolve 512 EMCCD camera, a Photometrics HQ2 CCD camera, an ASI MS-2000 stage controller, and laser lines at 488 and 561 nm all controlled by SlideBook 6.0 software (Intelligent Imaging Innovations, Denver, CO). TIRF microscopy was performed on a Zeiss Axiovert equipped with Photometrics QuantEM 512SC EMCCD camera, 100X Plan Apo (NA 1.46) objective and laser lines at 488 and 561 nm controlled by ZEN2 Blue software (Carl Zeiss).

**Live Cell Imaging**

Cells were plated in 35 mm glass observation dishes (MatTek or BiopTechs) at a density of ~$10^5$ $cm^{-2}$ and allowed to adhere for 10 minutes. Cells were rinsed twice in starvation buffer (SB) (16.8 mM sodium/potassium phosphate adjusted to pH 6.4) and placed in 1 - 2 ml of SB for imaging 45 – 75 min following the onset of starvation. Assays of vegetative cells used low fluorescence media (ForMedium) in place of SB. For IRM experiments, cells were rinsed in twice in starvation buffer and plated on bacteriological plastic at a density of 1.4 x $10^5$ $cm^{-2}$ overnight (12-15 hours) at 11 °C to induce polarization (122). Cells were then resuspended, plated in observation dishes at room temperature, and imaged by IRM from 10-30 min after plating.

**Data Analysis**

Statistical analyses were performed in Origin 9.0 (for ANOVA with Tukey post-hoc tests) or SPSS Statistics version 20 (for multiple ANOVA with contrasts). Significance was accepted at the $p < 0.05$ level.

**Plasmid Design and Expression**

An integrating expression plasmid for the N-terminal GFP-tagged DdMyo7 full-length myosin, pDTi74, and the extrachromosomal GFP-Myo7 and GFP-Myo7 Tail plasmids, pDTi112 and pDTi35 have been described previously (114, 164). Standard molecular biological methods were used to generate mutant expression plasmids in the integrating pDTi74 background. Enzymes were obtained from New England Biolabs and the sequences of all PCR-generated DNAs were verified by sequencing (University of Minnesota Genomics Center). RFP-tagged Lifeact in pDM358 (122) was a gift from Hannah Brzeska (Laboratory of Cell Biology, NHLBI, NIH). The ΔFERM2 deletion mutant was created using PCR-based methods to delete the C-terminal coding sequence from the *myoI* gene (accession number L35321.2) encoding the FERM domain (nts 6551 - 7453; ends at amino acid 2056). The ΔMF1-SH3 deletion mutant (nts 3725 – 5434; amino acids 1115-1684) and Motor-Pro1-MF1-SH3 mutant (ΔPro2-MF2 deletion at nts 5453 – 7453; ends at amino acid 1690) were generated similarly. The KKAA mutant (K2333A, K2336A) was generated using the Q5 mutagenesis kit (New England Biolabs) to change the corresponding codons to GCA. DdMyo7 motor-SAH (amino acids 1 - 1020) was

generated using PCR to obtain a genomic clone encoding the 5′ region of the *myoI* gene (nts 49 - 3442) and ligating this to the extrachromsomal vector pTX-GFP (221). DdMyo7 motor-Pro1 (amino acids 1-1115) was generated by PCR (nts 49 – 3727) followed by ligation into a pDXA-based GFP expression vector (222). Expression vectors for a motor-SAH construct (aa 1-879) in pTX-GFP or pDXA were also tested, but protein expression was poor and declined over time in culture. For tail domain fusions, the motor-Pro1 plasmid was digested with BstEII and XhoI yielding a linearized vector for Gibson assembly. The 5′ fragment from the BstEII site through aa 1115 was amplified by PCR (Fwd.: 5′-cattagaattagaaaattgg-GTTACCCAATCCGTCATAC-3′, Rev: 5′-tcgatcgg-TGAAACAGTTGGTTGTGG-3′). For motor-Pro1-MyTH4a, the 5′ fragment through aa 1316 was amplified (Rev: 5′-aatttttgttctaatgcatctcgagctagctta-ACGATTCTCTTTAATTGATTCTAATTC-3′). For motor-Pro1-MF2, the 5′ fragment through aa 1115 was amplified (Rev: 5′-ggtgatga-TGAAACAGTTGGTTGTGG-3′) along with a fragment encoding MF2 (aa 1811-2357; Fwd: 5′-ccaactgtttca-TCATCACCACCAAACTTTAG-3′, Rev: 5′-aatttttgttctaatgcatctcgagctagc-TTATTGAGAAGAATAAAATTGATAAACTG-3′). The motor-Pro1-HsMyo10 sequences were constructed as follows: the regions of the Myo10 gene (accession no. NP_036466) encoding either the MyTH4 (amino acids 1501-1699) or MF (amino acids 1501-2058, omitting residues 1871-1906 as previously described (100), were amplified by PCR (Fwd.: 5′-actgtttca-CCGATCGACACCCCCACC-3′, MyTH4 Rev: Rev: 5′-aatttttgttctaatgcatcgctagctta-TTCCTGCCTGTGGATCAGAG-3′; MF Rev: 5′-aatttttgttctaatgcatc-GCTAGCTCACCTGGAGCTG-3′). The linearized vector, 5′ DdMyo7

fragment and 3′ Myo10-MF or Myo10-MyTH4 tail fragment were assembled using HiFi Assembly Master Mix (NEB), transformed into *E. coli*, and verified by sequencing. DdMyo7 Motor-Pro1-Myo44 MF was generated in a similar fashion but instead the coding sequence for the DdMyo44 MF2 domain (aa 2906-3425) was amplified from a genomic clone (97); (accession number XM_638108.1) as was a linker region encoding the Pro1 region (Fwd: 5′-cattagaattagaaaattgg-GTTACCCAATCCGTCATAC-3′, Rev: 5′-ggttcacc-TGAAACAGTTGGTTGTGG-3′; Fwd: 5′-actgtttca-GGTGAACCACAATTTTCTAC-3′, Rev: 5′-aatttttgttctaatgcatctcgagtt-ATCTCTTTTCTTTTTCTTTTCTTTCTC-3′) and these were then assembled in frame into an integrating plasmid containing DdMyo7 motor-Pro1 coding sequence and verified by sequencing. DdMyo7 Motor-Pro1-mCherry was generated in a similar fashion but amplifying the mCherry coding sequence as a 3′ tail fragment (Fwd.: 5′-actgtttca-ATGGTGAGCAAGGGCGAG-3′, Rev: 5′-aatttttgttctaatgcatcgctagc-CTACTTGTACAGCTCGTCCATG-3′) and assembled in frame. The ΔFERM1 (nts 3734 - 5041; deleted for amino acids 1314 - 1553), ΔMF1 (nts 3734 - 5230; deleted for amino acids 1118 - 1616) and ΔMF2 (nts 5903 - 7453; ends at amino acid 1840) deletion mutant integrating expression plasmids were generated using PCR. (114). The clone encoding bovine Myo10 was a gift from Richard E. Cheney (UNC – Chapel Hill). The bovine Myo10 gene was amplified by PCR and cloned into the pTX-GFP expression plasmid.

**Molecular Phylogenetics**

The majority of MF myosin heavy chain sequences were downloaded from

http://www.cymobase.org/, a database of cytoskeletal protein sequences (223) curated by Dr. Martin Kollmar and the CyMoBase team at the Max-Planck-Institute for Biophysical Chemistry (Göttingen, Germany). Additional sequences were produced by the Joint Genome Institute (224) or the *Physarum polycephalum* Genome Resources server (225) (http://www.physarum-blast.ovgu.de). A total of 162 sequences from 58 taxa were gathered and an initial alignment of these sequences was performed using MUSCLE (226). Only sequences with intact motor and MF domains were retained, to exclude incomplete or pseudogenic sequences. Domain boundaries were set using the nominal position of human Myo7A MF2 (residues 1749 – 2206). When two MF domains were present only the C-terminal domain was used. Simultaneous alignment and tree estimation (SATé II) was performed using MAFFT/MUSCLE and FastTree (204). SATé performed an initial realignment followed by centroid decomposition and alignment using a WAG+gamma substitution model. Maximum subproblem size was set to 50% (81 sequences).

**Image Analysis**

Filopodia were imaged in the plane of contact between the cell and the coverslip where fluorescence of filopodia tips was greatest. The focal plane was located by DIC or by single frame confocal exposures. For counting assays, 3 - 6 planes were acquired at 63X magnification with a vertical step size of 0.3 µm repeated for 30 - 60 seconds. Assays of initiation and elongation used 100X magnification in 2 planes (1 µm step size) to increase the imaging rate. Automated image analysis generated a mask of the cell body and identified filopodia tips using GFP-DdMyo7 fluorescence. The use of DdMyo7 as a

filopodial marker was validated by blinded manual analysis of paired DIC and GFP images in which a single DIC image was acquired a few seconds prior to the start of GFP imaging (Fig. 7; Table 5). Membrane protrusions identified in DIC were strongly correlated in WT or rescue cells with GFP-DdMyo7 punctae at filopodia tips as previously reported (114, 227). The number and length of filopodia (distance between the DdMyo7 puncta and cell periphery) were then measured (Fig. 5D). Two populations of cells were observed, those expressing DdMyo7 (showing cytosolic GFP fluorescence) and those not expressing the fusion protein (no fluorescence). An accurate count of cells expressing the protein but showing zero filopodia was not feasible with this method due to the difficulty in differentiating between cells not expressing or only weakly expressing DdMyo7. Consequently, filopod number was defined as the number of filopodia divided by number of cells with one or more filopodia (Fig. 5D). Filopodia number was determined by counting filopodia tips marked with GFP. Briefly, regions corresponding to cell body were identified using a median filter and thresholding to create an image mask. Two thresholding methods were tried in Fiji/ImageJ (228): full frame thresholding with moments and local thresholding with the Bernsen method (229). The former had reliable results for filopodia number but unreliable results for filopodia length based on small-scale manual analysis. Local thresholding required manual correction of the mask file to remove fluorescent debris and autofluorescent cells with low GFP expression. However, local thresholding produced reliable results for both number and length, so was used for all analyses.

Rescue of filopod formation by DdMyo7 mutants was classified in two categories: First, mutant proteins that produced numerous filopodia at near-wild type frequency were analyzed by automated counting of filopod tips in the first frame of fluorescence imaging. The second category included mutant proteins with minimal tail domains (MF1-SH3, MF2, M4a, HsMyo10MF, HsMyo10M4, Myo44MF2) that produced filopodia more rarely and required manual analysis. For automated counting, filopodia tips were identified using the Find Maxima function in ImageJ. The radial intensity distribution around each candidate was analyzed in terms of the sample skewness $G_1$ (230). Candidates with skewness less than 1 were considered fluorescent debris and discarded. Remaining candidates were registered to the nearest cell center of area. Candidates >20 μm distant were discarded, while candidates >10 μm distant were manually reviewed for accuracy. Both the total number of cells and number of filopodia registered to each cell were recorded. Because the proportion of cells with filopodia varied, filopodia number was defined as number of filopodia divided by number of cells with one or more filopodia. Mutants with a low frequency of filopodia were manually reviewed to identify filopodia in each frame of the time lapse image stack (typically 10 – 30 s, no longer than 80 s). Image stacks were analyzed by an operator blinded to the identity of the DdMyo7 mutant protein in each image. Filopodia tips were identified as fluorescent puncta neighboring a GFP-positive cell that were observed in 2 or more frames and where the linear extent of the filopod was either clearly visible by GFP fluorescence, or not visible in the confocal section but inferred by the directed motion of the tip relative to the cell body. Regions of interest were acquired to indicate the locations of the filopodia identified by the first operator. For length analysis, a

second operator manually reviewed the position of the ROI in relation to the tip and the threshold mask of the cell body. For filopod number analysis, only filopodia appearing within 10±1 s of the onset of GFP excitation were included to establish a uniform counting procedure for these low frequency events.

Length of filopodia was estimated as the distance to the edge of the cell body on a line from the tip to the cell center. This estimate was validated by small-scale manual analysis. Kymographs and line scans were performed using manual tracing to define regions of interest. Filopod line scans used for fluorescence intensity analysis were aligned either automatically at the peak fluorescence intensity or, in the case of DdMyo7 tail, manually aligned at the distal ends of filopodia when tip enrichment was not observed. Kymographs used the maximum intensity from a 1.3 μm wide perpendicular region at each time point. The resulting image was processed with edge detection and thresholding to produce a plot of tip position where velocity was equal to the slope. Linear regression was performed (minimum of 5 pts, ≤ 0.8 s/pt, 133 nm pixel width) and an elongation velocity event was recorded using the regression slope of the longest segment where the squared correlation coefficient exceeded 0.98.

IRM images were processed by correction for flat-field illumination (using the averaged image intensity for each assay followed by a 2 μm median filter) and thresholding as before using the same filter radius. Average contact area was calculated using the ImageJ "Analyze Particles" function with a circularity range of 0.10-1.0 to remove thresholding artifacts and a size range of 1-50 $\mu m^2$ to exclude both small debris and cells with a large

contact area exclude non-migrating cells.

**Western blotting**

Expression of the DdMyo7 fusions was evaluated by western blotting (Fig. 6) using a mouse monoclonal anti-GFP antibody (MMS-118R, Covance Inc.) a rabbit polyclonal antibody specific for the DdMyo7 heavy chain (164), and the heavy chain of the class I myosin, MyoB, as a control (114, 161). Washed blots were incubated with Alexa Fluor 680– or 800–conjugated goat anti-rabbit or goat anti-mouse secondary antibodies (Molecular Probes, Invitrogen). Detection was performed using an Odyssey infrared imaging system (LI-COR Biosciences).

## 2.6 Acknowledgements

The authors thank Hilary Bauer, Zoé Henrot, Alex McQuown and Drs. Guillermo Marqués and Mark Sanders (University of Minnesota Imaging Centers) for expert technical assistance. We thank Drs. Naomi Courtemanche, Melissa Gardner, Sivaraj Sivaramakrishnan and Gaku Ashiba for many valuable discussions. We also thank Dr. Martin Kollmar for developing and maintaining CyMoBase (http://cymobase.org), Dr. Tandy Warnow (U. Illinois) for introducing us to SATé. Excellent computational resources were provided by the Minnesota Supercomputing Institute. KJP was supported by the NIH Training Program in Muscle Research (AR007612) and a University of Minnesota Doctoral Dissertation Fellowship, HVG by NSF award MCB-1244593 and GWGL by NIH awards R42DA037622 and R21NS095109-01. AH was supported by grants from the ANR-13-BSV8-0019-01, Ligue Nationale Contre le Cancer and ARC subvention fixe and MAT was supported by NSF MCB-124423.

**Table 5. Blinded Scoring of Filopodial Protrusions by GFP Fluorescence and DIC.**

| GFP-Tagged Protein in KO Cells | Total Cells | No. GFP+ Cells | Protrusions/ Cell (GFP) | No. Protrusions (GFP) | No. Protrusions (DIC) | No. Protrusions (GFP) | No. Protrusions (DIC) |
|---|---|---|---|---|---|---|---|
| NONE | 128 | - | - | - | 15 | - | 6.3% |
| RESCUE | | | | | | | |
| DdMyo7 | 113 | 83 | 1.51 | 125 | 116 | 51.8% | 48.2% |
| ΔMF1-SH3 | 137 | 82 | 1.27 | 104 | 86 | 43.9% | 36.3% |
| ΔFERM2 | 82 | 39 | 1.33 | 52 | 52 | 35.9% | 35.9% |
| KKAA | 81 | 32 | 5.03 | 161 | 91 | 81.3% | 62.5% |
| NO RESCUE | | | | | | | |
| Motor-SAH | 138 | 74 | 0.03 | 2 | 1 | 2.7% | 1.4% |
| Motor-Pro1 | 266 | 126 | 0.01 | 1 | 11 | 0.8% | 2.4% |
| Tail | 1028 | 58 | 0.00 | 0 | 0 | 0.0% | 0.0% |
| CHIMERAS | | | | | | | |
| Motor-Pro1-HsM10M4 | 691 | 400 | 0.05 | 18 | 15 | 3.5% | 2.3% |
| Motor-Pro1-HsM10MF | 542 | 255 | 0.09 | 22 | 71 | 5.9% | 11.8% |
| Motor-Pro1-M44MF2 | 318 | 152 | 0.06 | 9 | 15 | 3.9% | 4.6% |

Paired DIC and GFP still images were manually scored for filopodia in several *myo7* null cell lines expressing GFP-Myo7 fusions found to either rescue or not rescue filopod extension. DIC images were first analyzed for cells extending slender projections and the number of projections per cell scored. The corresponding fluorescence image was then analyzed for GFP-expressing cells and the number of GFP-tipped projections with a clear connection to the cell body was then counted for each cell. Shown above are the values obtained for filopodia per cell for the GFP-expressing cells as observed both by DIC and fluorescence and the % of GFP-expressing cells that are observed to extend protrusions in DIC. Note the strong correspondence between filopodia scored by GFP fluorescence and protrusions seen in DIC.

**Table 6. Filopodia Number, Length and Elongation Velocity in DdMyo7-expressing Cells.**

| Back-ground | Protein | Filopod Number ± SEM* | %Change [95% C.I.] | *p* | Filopod Length ± SEM* (µm) | %Change [95% C.I.] | *p* | Elongation Velocity ± SEM (*n*)** (µm/s) | %Change [95% C.I.] | *p* | N |
|---|---|---|---|---|---|---|---|---|---|---|---|
| WT | DdMyo7 | 2.7 ± 0.3 | - | - | 2.6 ± 0.3 | - | - | n.d. | - | - | 4 |
| | ΔMF1-SH3 | 3.1 ± 0.1 | 15% [-31, 61%] | .51 | 2.7 ± 0.2 | 5% [-21, 31%] | .70 | n.d. | - | - | 4 |
| | ΔFERM2 | 2.9 ± 0.4 | 6% [-40, 52%] | .78 | 2.9 ± 0.2 | 12% [-13, 39%] | .34 | n.d. | - | - | 4 |
| | KKAA | 4.4 ± 0.6 | 62% [16, 108%] | .01 | 2.8 ± 0.1 | 8% [-18, 35%] | .52 | n.d. | - | - | 4 |
| KO | DdMyo7 | 2.8 ± 0.4 | - | - | 2.9 ± 0.2 | - | - | 0.40 ± 0.03 (26) | - | - | 6 |
| | ΔMF1-SH3 | 3.3 ± 0.3 | 17% [-20, 53%] | .36 | 2.3 ± 0.1 | -20% [-2, -39%] | .02 | 0.37 ± 0.02 (48) | -7% [-28, 13%] | .77 | 6 |
| | ΔFERM2 | 3.8 ± 0.4 | 35% [1, 70%] | .04 | 3.3 ± 0.2 | 14% [-4, 32%] | .12 | 0.29 ± 0.01 (60) | -28% [-48, -8%] | .002 | 8 |
| | KKAA | 4.8 ± 0.3 | 69% [31, 108%] | .0008 | 2.7 ± 0.2 | -8% [-26, 11%] | .41 | 0.38 ± 0.03 (31) | -4% [-26, 18%] | .97 | 5 |

The indicated proteins were expressed in WT or KO Dicty cells and filopodia parameters were assayed. C.I. = confidence interval; SEM = standard error of the mean; %Change is relative to DdMyo7 in the same background (WT or KO).

* SEM of *N* independent assays; ** SEM of *n* elongation events.

**Table 7. Filopodia Length in Cells Expressing Minimal and Chimeric DdMyo7 Motors.**

| Protein | Filopod Length ± SEM (µm) | n | N | *p* (Myo10MF) |
|---|---|---|---|---|
| Motor-Pro1-MF1-SH3 | 2.5 ± 0.2 | 89 | 5 | .83 |
| Motor-Pro1-MF2 | 3.1 ± 0.6 | 64 | 3 | .12 |
| Motor-Pro1-MyTH4a | 3.2 ± 0.4 | 47 | 4 | .76 |
| Motor-Pro1-HsMyo10MF | 3.6 ± 0.4 | 55 | 8 | - |

Filopodia length in *myo7* null Dicty cells expressing the indicated proteins. Mean of *N* independent assays is shown. SEM = standard error of the mean. *Multiple ANOVA of *n* filopodia ($p = .34$) contrasted with HsMyo10MF.

**Table 8. Filopodia Number in Cells Expressing Minimal and Chimeric DdMyo7 Motors.**

| Protein | Filopod Number ± SEM | *n* (cells) | N | *p* (MyTH4a) * | p (Myo10MF) * |
|---|---|---|---|---|---|
| Motor-Pro1-MF1-SH3 | 2.8 ± 0.6 | 26 | 5 | n.d. | n.d. |
| Motor-Pro1-MF2 | 4.0 ± 0.1 | 42 | 3 | n.d. | n.d. |
| Motor-Pro1-MyTH4a | 1.8 ± 0.2 | 38 | 5 | - | .27 |
| Motor-Pro1-HsMyo10MF | 2.2 ± 0.2 | 18 | 7 | .27 | - |
| Motor-Pro1-HsMyo10MyTH4 | 1.3 ± 0.1 | 50 | 9 | .012 | .0012 |
| Motor-Pro1-Myo44MF2 | 1.1 ± 0.1 | 10 | 4 | .025 | .0044 |
| Motor-Pro1 | 1.2 ± 0.1 | 18 | 4 | .012 | .0016 |

Filopod number in *myo7* null Dicty cells expressing the indicated proteins. Weighted mean of *N* independent assays is shown. SEM = standard error of the mean.

*Multiple ANOVA of *n* cells ($p = .001$) with contrasts. n.d. = not determined.

## 2.7 Figures

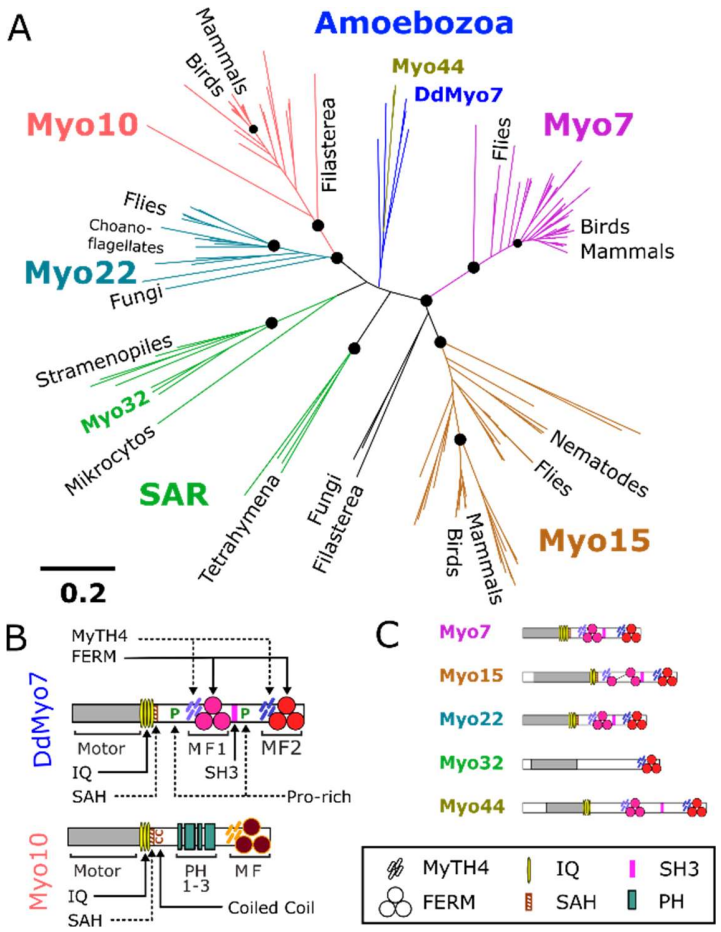


**Fig. 4. Evolutionary relationships of MyTH4-FERM Myosins.**

(A) Phylogenetic analysis of MyTH4-FERM (MF) domains of myosins from representative organisms as determined by SATé (204). Likelihood values at major branch points (>95%) are indicated by circles, and the scale is as defined by FastTree (231).

(B) Domain organization of DdMyo7 and Myo10, two MF myosins involved in filopod formation. See symbol legend at bottom for identification of domains. Domains of DdMyo7 include the Motor: myosin catalytic domain; IQ: light-chain binding motifs 1-4; SAH: single α-helix; Proline-rich regions; MyTH4: myosin tail homology 4; FERM: band 4.1, ezrin, radixin, moesin; and SH3: Src Homology 3. Myo10 contains three PH (Pleckstrin Homology) domains.

(C) Domain organization of other major MF myosin families.

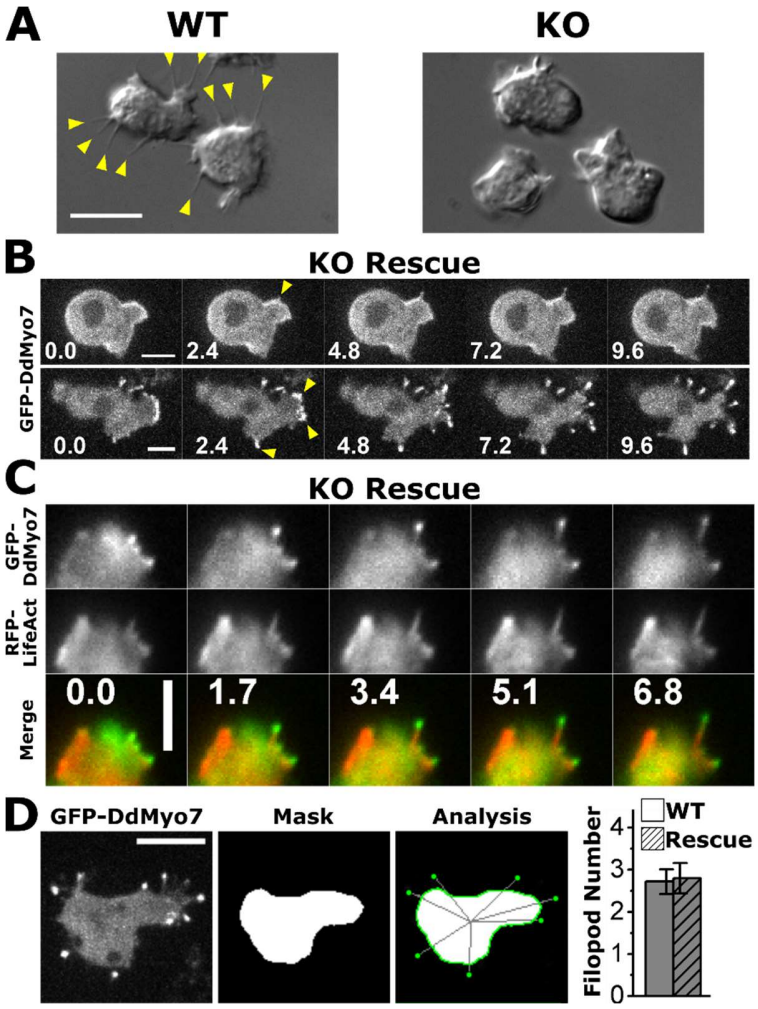


**Fig. 5. DdMyo7 is present in filopodia from their initiation and at filopod tips during elongation.**

(A) DIC images of wild type (WT) and *myo7* null cells (KO) illustrating the absence of filopodia in cells lacking DdMyo7. Scale 10 µm.

(B) Filopod initiation in two KO cells expressing GFP-DdMyo7 over 10 s. The arrowheads point to emerging and extending filopodia that show the myosin concentrating near the distal tips. Scale 5 µm.

(C) Time series showing formation of a filopodium at the edge of an actin-rich pseudopod in a *myo7* null cell expressing GFP-DdMyo7 and RFP-LifeAct over time (seconds). Scale 4 µm.

(D) Automated analysis of filopod number in maximum intensity projection confocal images. Shown is a representative cell expressing GFP-DdMyo7 (scale 10 µm). The cell body is masked (Mask) and filopod tips are located by GFP intensity before registering them to the cell (Analysis). Quantification of multiple images from either wild type (WT) or *myo7* null cells (KO) expressing GFP-DdMyo7 yields an average of 2.8 filopodia per cell, a baseline for further assays (see also

Table **6**).

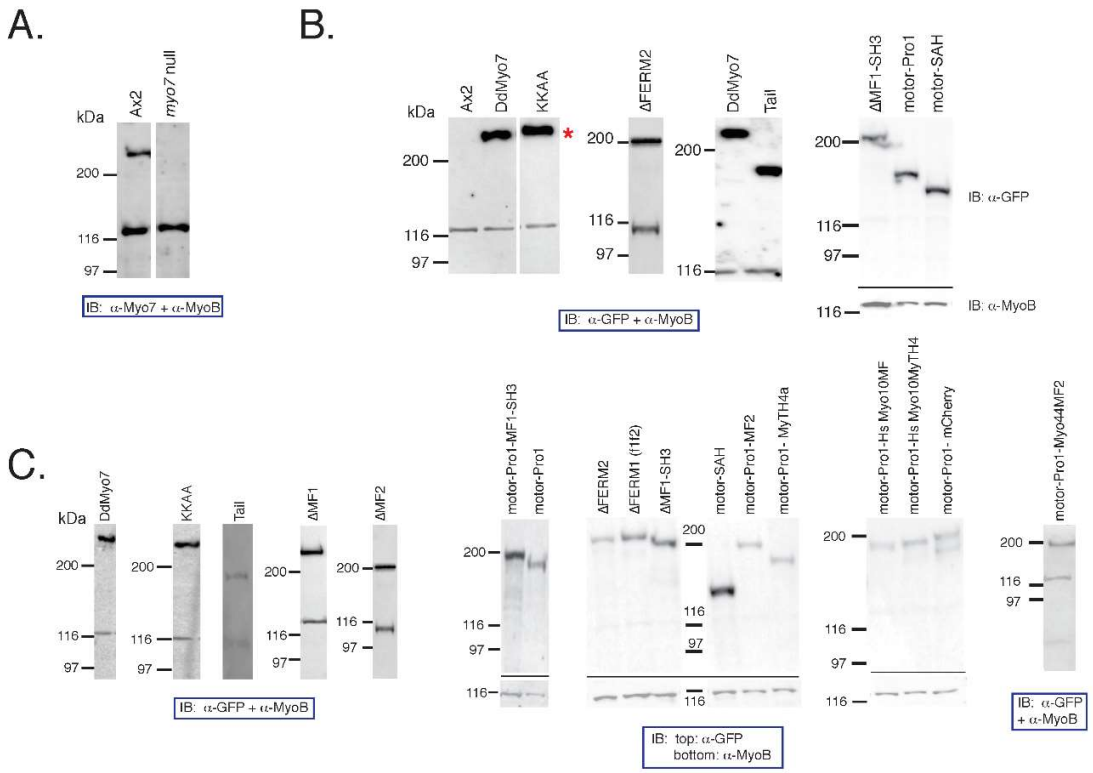


**Fig. 6. Western analysis of GFP-DdMyo7 fusions.**

Western blotting of total cell lysates to validate expression of GFP fusions.

(A) wild type and *myo7* null lysates probed with anti-Myo7 antibody showing the presence of the ~270 kDa heavy chain in wild type cells (Ax2) that is missing from the *myo7* null.

(B) Wild type or (C) *myo7* null cells expressing the DdMyo7 fusions analyzed probed with anti-GFP to detect the expressed heavy chain. The position of the full-length GFP fusion is indicated (*). All samples shown were also blotted for the 135 kDa MyoB (myosin 1B) heavy chain that is used as a loading control. Note that lanes from several independent blots are shown.

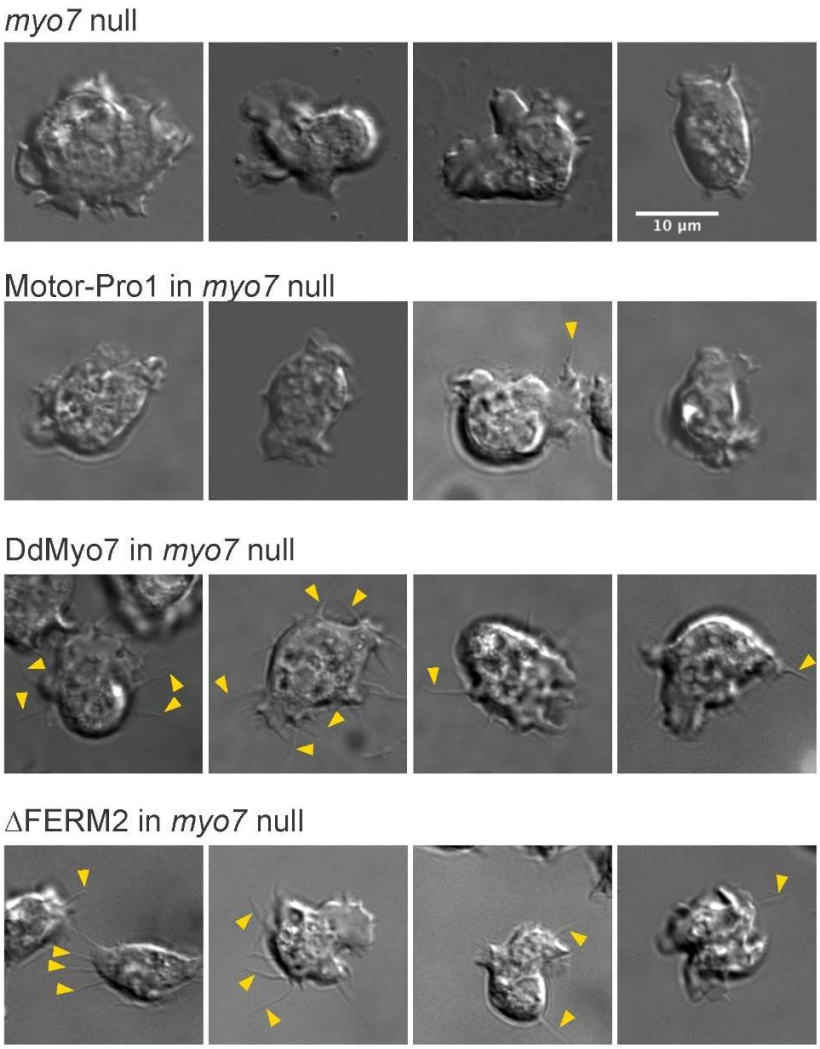


**Fig. 7. DIC Images of *Dictyostelium* cells under optimal conditions for filopodia formation.**

Randomly selected images of cells imaged by DIC microscopy illustrating scoring of filopodia for comparison with scoring by filopodial tip GFP fluorescence. Shown are the *myo7* null cell line that does not extend filopodia, a non-rescued cell line (motor-Pro1) and two rescued lines (DdMyo7 and ΔFERM2). Examples of filopodial extensions are indicated by arrowheads. Non-rescued cell lines show very rare protrusions compared to rescued cell lines (see also Table 5). Scale = 10 µm.

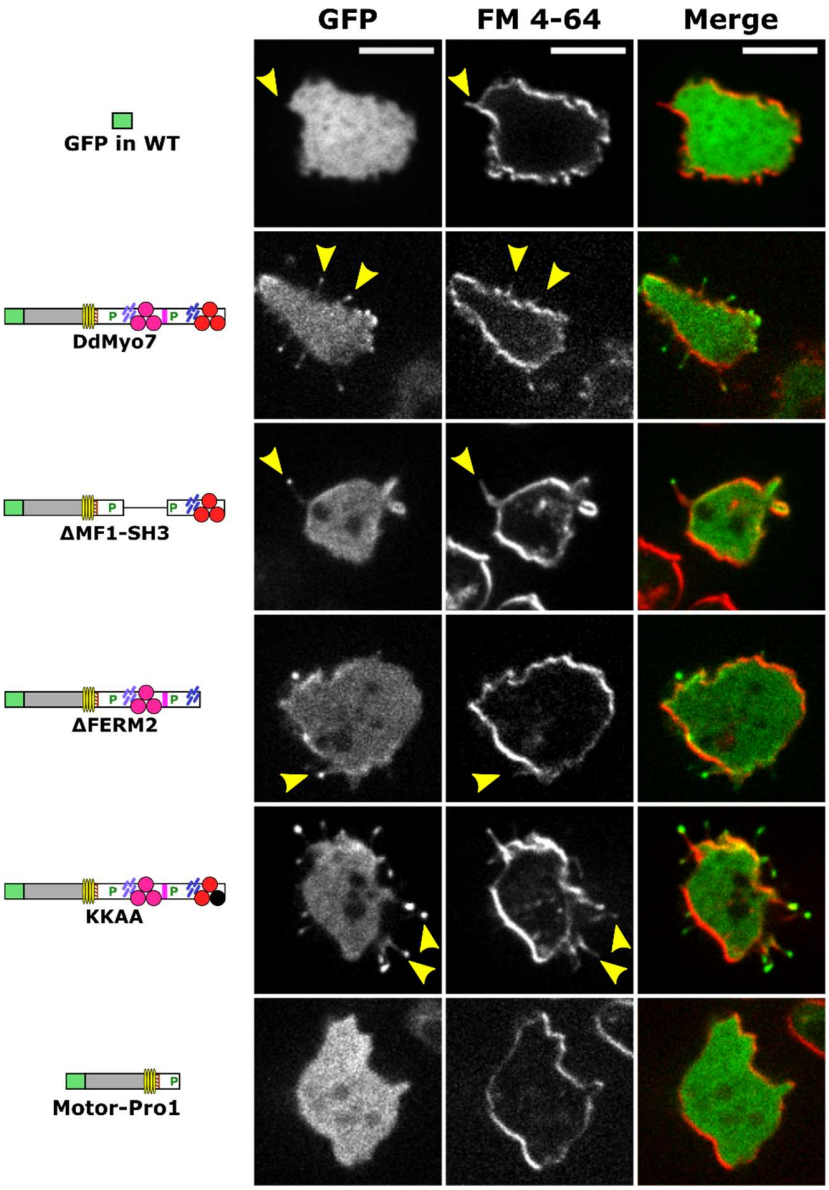


**Fig. 8. Filopodia visualized by GFP-DdMyo7 and fluorescent membrane marker FM 4-64.**

Dicty *myo7* null cells (KO) expressing full-length and mutant DdMyo7 proteins, or GFP alone, were starved 1 hour and incubated with 0.25 µg/ml FM 4-64 membrane dye for 1-5 minutes before confocal imaging. A single image plane is shown for the GFP (left) and red FM 4-64 (center) channels, the merge of the two channels is shown in the right. DdMyo7 is enriched in filopod tips and the filopodia are visible with FM 4-64 as well as GFP staining along their length (yellow arrows). Note the cytosolic localization of GFP expressed in WT cells (top) contrasted with filopod tip localization of GFP-DdMyo7 in KO cells.

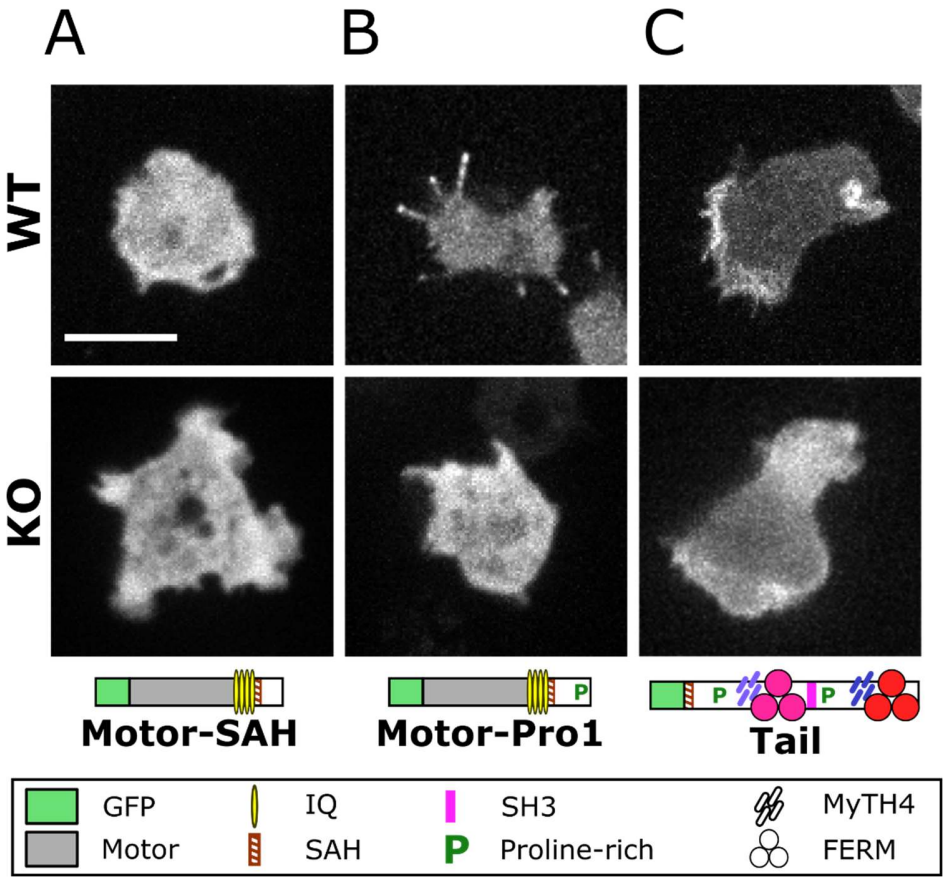


**Fig. 9. The head and tail of DdMyo7 are required for filopod formation.**

(A) DdMyo7 motor-SAH does not localize to filopodia when expressed in wild type (WT) cells and does not rescue filopod formation in the *myo7* null (KO) cells. Scale = 10 µm.

(B) Motor-Pro1 localizes to filopodia in WT but does not rescue filopod formation in KO.

(C) DdMyo7 Tail localizes to the cell leading edge in both WT and KO cells, and weakly localizes to filopodia in WT cells but does not rescue filopod formation in KO. Symbol legend with domain identification (same as in Fig. **4**) below.

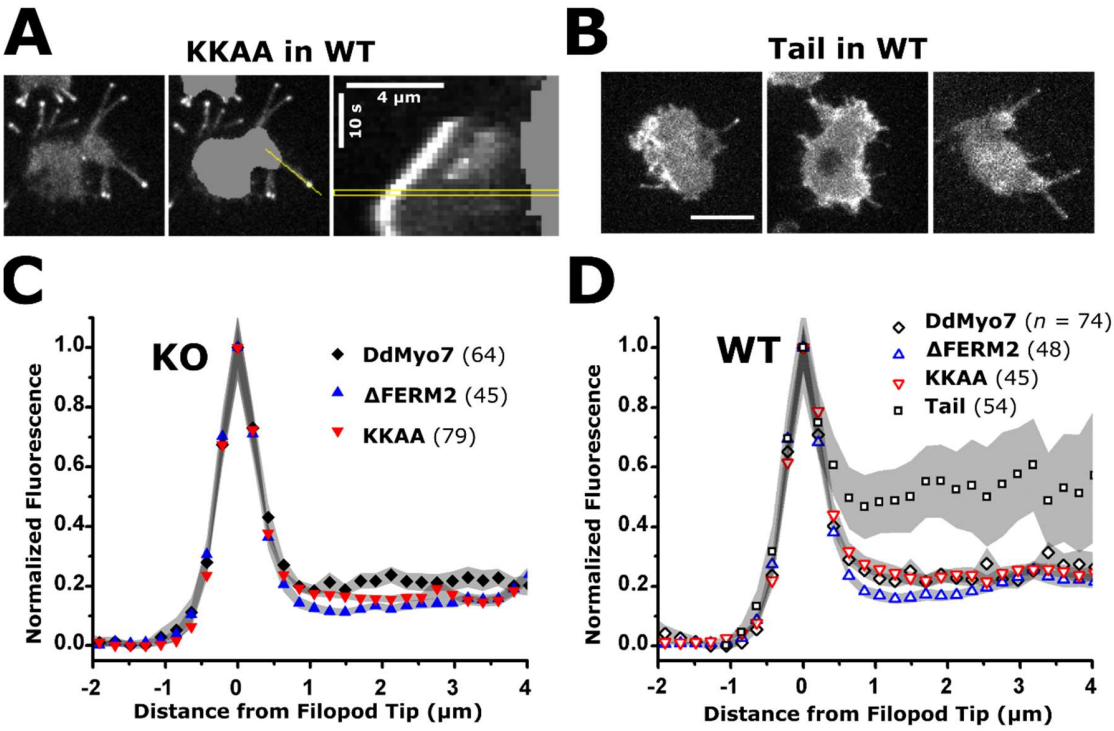


**Fig. 10. Deletion or mutation of the C-terminal FERM2 domain does not alter the distribution of GFP-DdMyo7 along the length of the filopodium.**

Fluorescence intensity of GFP-DdMyo7 was measured using the peak intensity in filopodia tips to align filopodia on the x-axis (positive values are toward cell body) and localize DdMyo7 mutants in filopodia using the mean intensity along the length.

(A) Shown at left is a representative WT cell expressing KKAA mutant protein (scale 10 µm). Images were processed by segmentation of the cell body (shown in center) followed by an intensity line scan when the filopod was near its maximum length. Kymograph shown at right with time point used for the line scan outlined in yellow. Scale is 4 µm × 10 s.

(B) The tail expressed in wild type cells is occasionally seen to be localized to filopodia tips and along the length of the filopodium. Scale 10 µm.

(C) Mean GFP intensity along the length of filopodia extended by *myo7* null cells (KO) expressing full-length DdMyo7, the C-terminal FERM2 deletion (ΔFERM2), or point mutant (KKAA). (D) Mean GFP intensity along the length of filopodia extended by wild type cells (WT) expressing full-length or mutant DdMyo7 or DdMyo7 tail. Note that a small portion of DdMyo7 is located uniformly along the actin-rich shaft in cells expressing the wild type or deletion mutants. In contrast, higher levels of the tail are observed along the shaft. The tail does not rescue filopod formation and is therefore not shown in KO. Peak value (x = 0) is normalized mean intensity of *n* filopodia (indicated for each condition). Shading indicates SEM of the number of filopodia averaged at each x value.

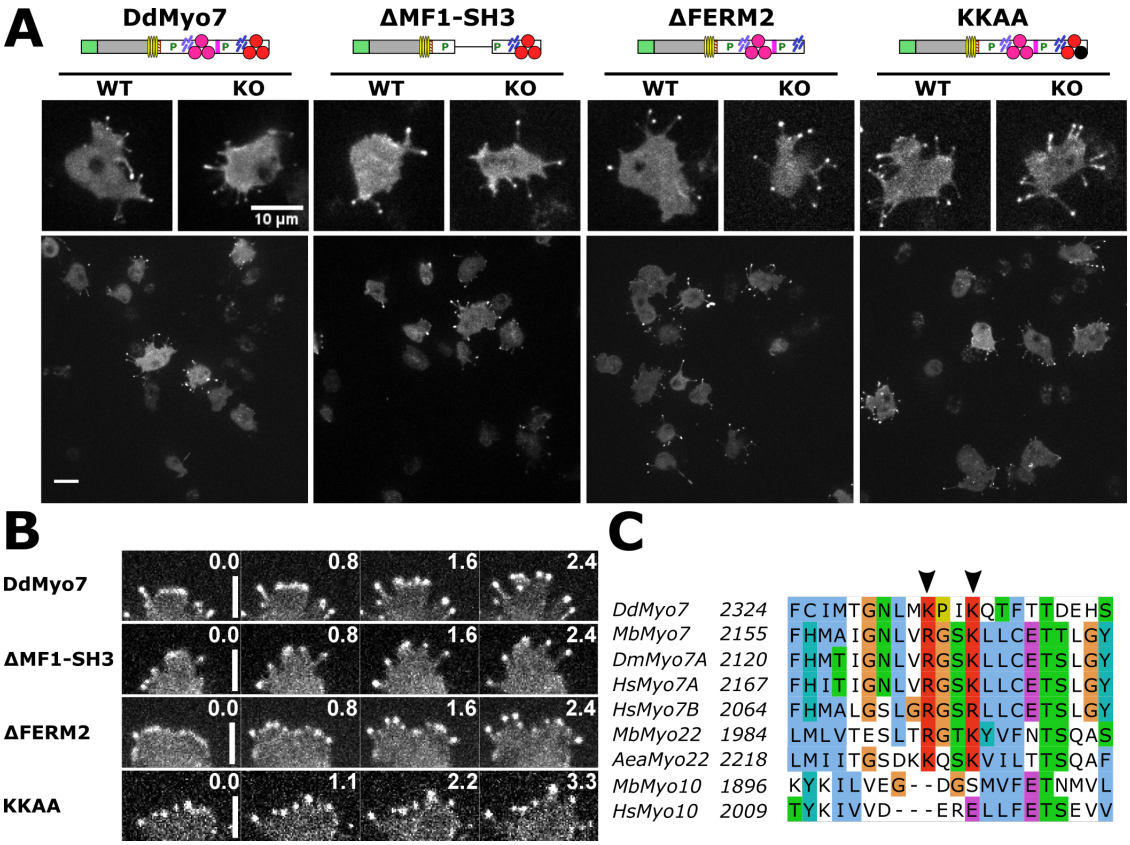


**Fig. 11. Rescue of Filopod Formation by Mutant DdMyo7.**

(A) Domain organization of DdMyo7 mutants, with GFP fused to the N-termini, is shown (same legend as Fig. **4**) with representative confocal fluorescence images of full-length DdMyo7, deletion mutants lacking the MF1-SH3 or C-terminal FERM2 domain, and a mutant with changes in conserved basic residues in the FERM2 domain (KKAA: K2333A, K2336A). The large panels show representative fields used in analysis of each DdMyo7 expressed in *myo7* null cells. Scale 10 µm.

(B) Detail of filopodia in extending pseudopods of KO cells expressing wild type and mutant DdMyo7 proteins. Note the localization of DdMyo7 to leading edge and subsequently to filopod tips during elongation. Time lapse indicated in seconds; scale bar is 4 µm.

(C) Sequence alignment showing a motif (K/RxxK/R) that is conserved in the FERM2 domain of MF myosins including DdMyo7, animal and choanoflagellate Myo7, and Myo22 but excluding Myo10. (arrows - conserved basic residues). Aea, *Aedes aegyptii*; Dd, *Dictyostelium discoideum*; *Dm*, *Drosophila melanogaster*; Hs, *Homo sapiens*; Mb, *Monosiga brevicollis*. Sequence positions are indicated on the left with conserved residues highlighted (blue = hydrophobic; red = basic; magenta = acidic; green = Asn/Thr/Ser; cyan = His/Tyr; orange = Gly; yellow = Pro).

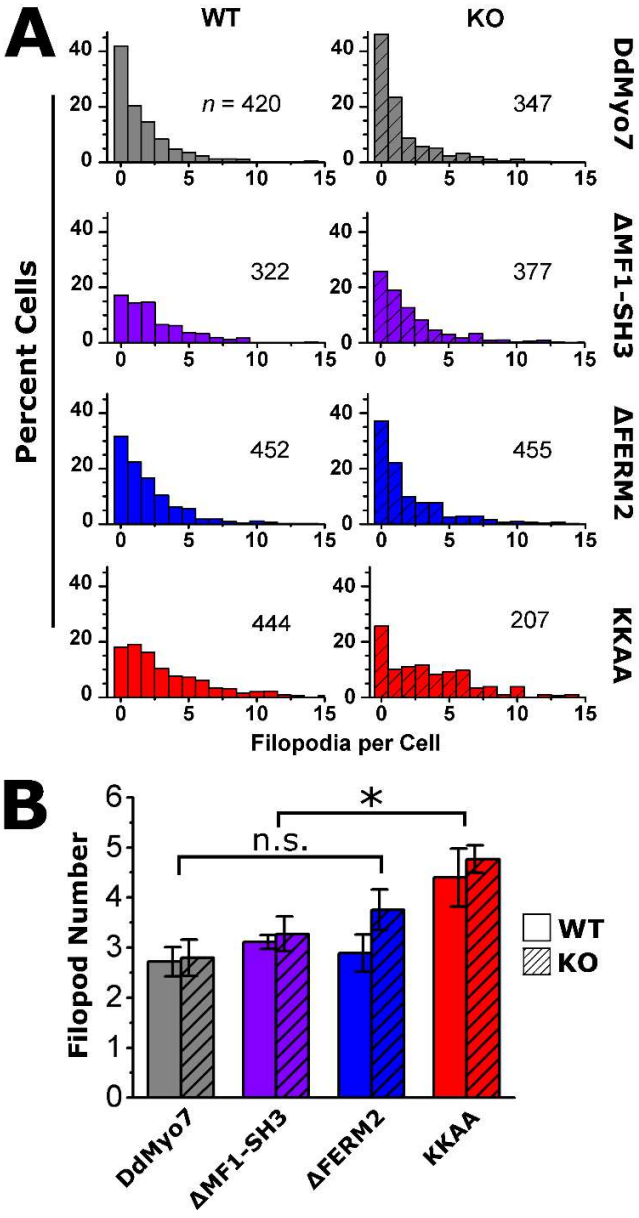


**Fig. 12. Filopod formation by DdMyo7 is regulated by the C-terminal FERM2 domain.**

Filopodia were counted in *Dictyostelium* cells expressing DdMyo7.

(A) Filopod number in cells expressing full-length DdMyo7, DdMyo7 with MF1-SH3 or FERM2 domain deletions (ΔMF1-SH3, ΔFERM2), and DdMyo7 with double point mutation in the FERM2 domain (KKAA). Data shown for wild type (WT, open bars) and *myo7* null cells (KO, shaded bars). Number of GFP-positive cells *n* includes cells with and without filopodia.

(B) Average filopod number per cell. Filopod number was defined as total filopodia divided by the number of cells with filopodia. Cells expressing the KKAA mutant (*) significantly increased filopod number by 66% compared with DdMyo7 ($p$ = .00008), 43% relative to ΔMF1-SH3 ($p$ = .002), and 36% relative to ΔFERM2 ($p$ = .003, multiple ANOVA with contrasts). Differences among other mutants were not significant (n.s.). Error bars are SEM; see

Table **6**.

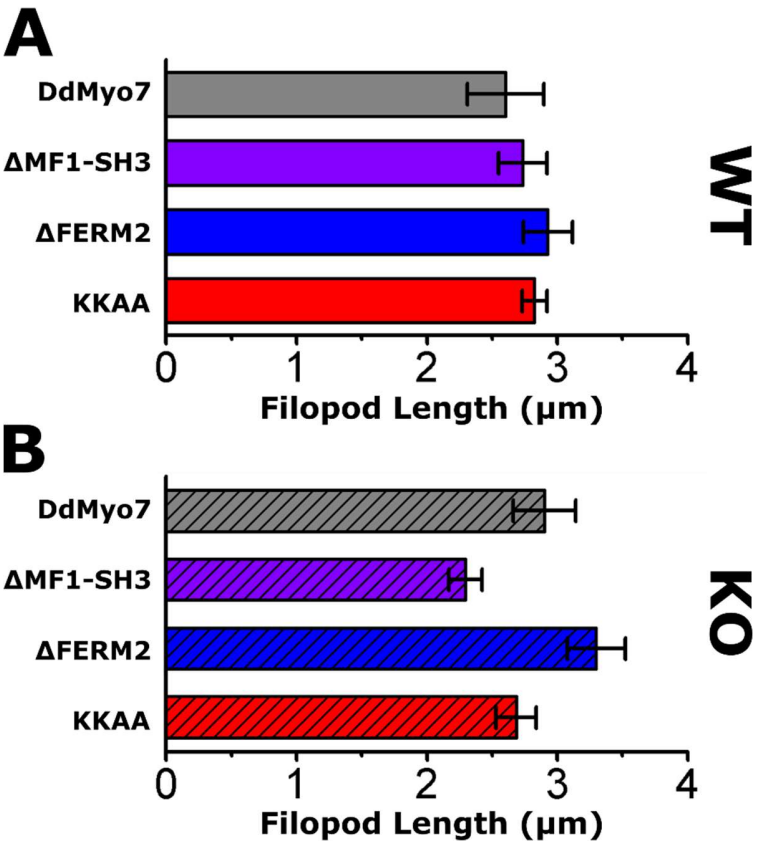


**Fig. 13. Filopodia length in *myo7* null cells expressing DdMyo7 is decreased with deletion of the MF1-SH3, but not the FERM2 domain.** Filopodia length was measured in cells expressing full-length or mutant (ΔMF1-SH3, ΔFERM2, KKAA) DdMyo7. Average filopodia length is shown for (A) wild type (solid bars) and (B) *myo7* null cells (shaded bars). Error bars are SEM; see also

Table **6**.

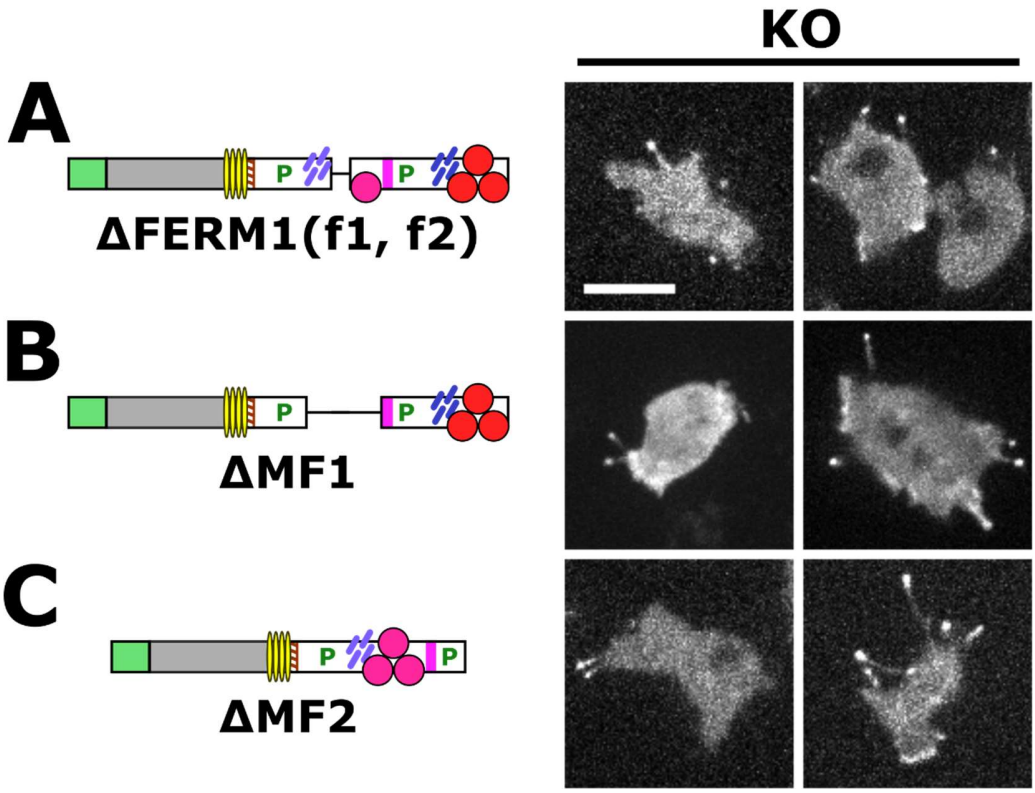


**Fig. 14. Deletion of the MyTH4-FERM domains does not impair filopod formation by DdMyo7.** DdMyo7 mutants expressed in *myo7* null cells (KO) were imaged by confocal microscopy. The domain organization of DdMyo7 mutants is shown on the left and fluorescence images on the right. (A) The ΔFERM1(f1, f2) mutant lacks the f1 and f2 subdomains of the internal FERM domain, but not f3 or the associated MyTH4 domain. Additional deletions remove the
(B) MF1 (located in the proximal tail region) or (C) MF2 (the common MF domain at the C-terminus). All mutants shown here localize to tips of filopodia and rescue filopod formation. Scale bar, 10 μm.

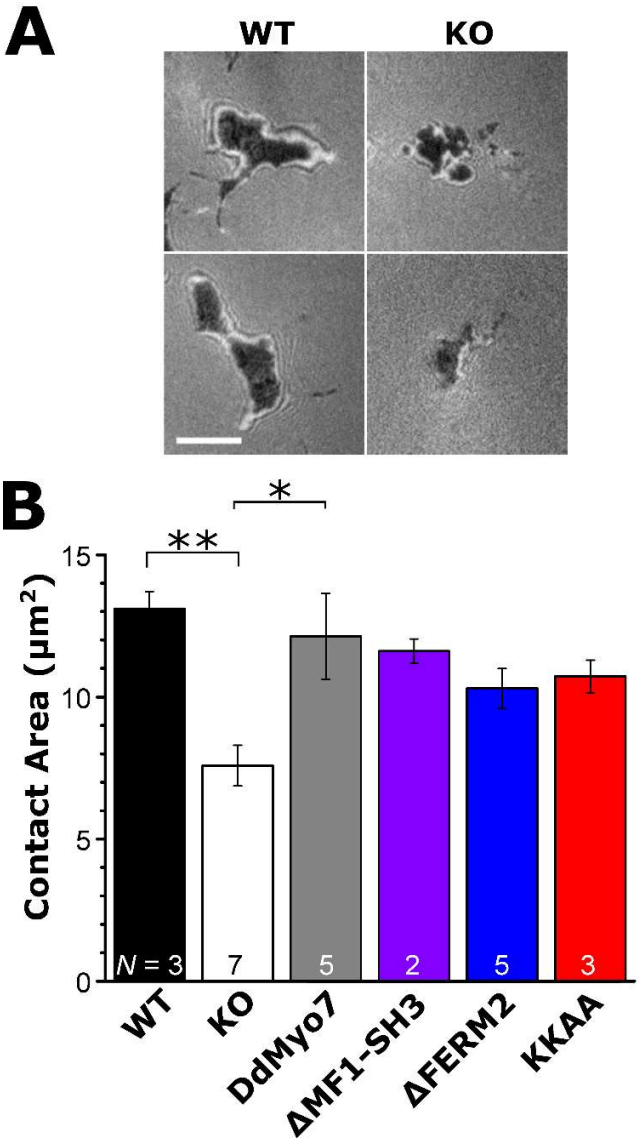


**Fig. 15. Rescue of the *myo7* null substrate adhesion defect in polarized cells.**
Cell-substrate contact area was measured by interference reflection microscopy (IRM).
(A) Shown are IRM images of cell contact area for polarized *myo7* null (KO) and wild type control cells. Scale 5 $\mu$m.
(B) Average contact area in *myo7* null *Dictyostelium* is significantly decreased relative to WT control (**, $p$ = .008) and DdMyo7 KO rescue (*, $p$ = .01) cells. Error bars are SEM of $N$ independent assays (shown). See also Fig. 16.

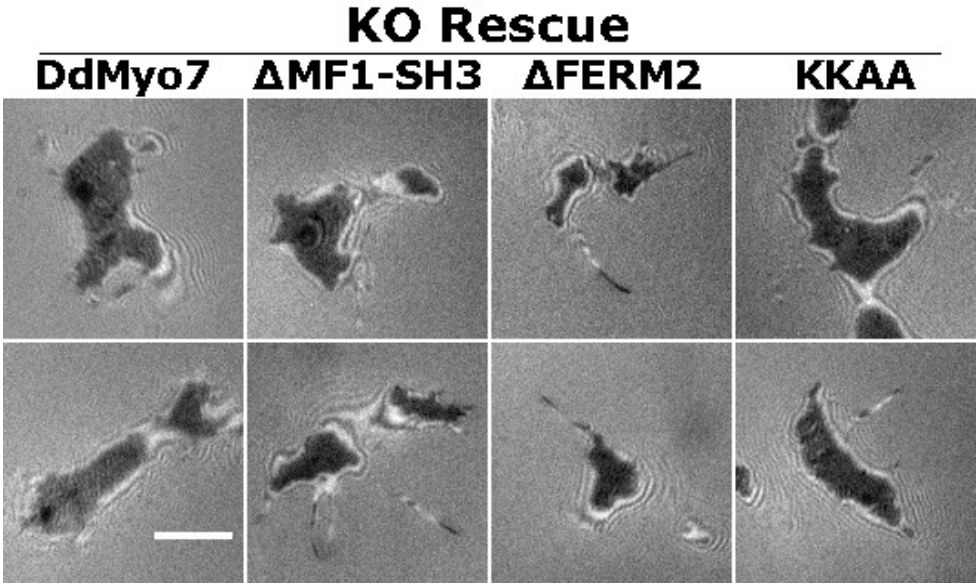


**Fig. 16. Substrate adhesion in polarized *myo7* null cells expressing DdMyo7 mutants.** Cell-substrate contact area was imaged using interference reflection microscopy (IRM). Shown above are IRM images of cell contact area for *myo7* null cells expressing full-length DdMyo7, ΔMF1-SH3, ΔFERM2 and KKAA mutant proteins. Scale 5 μm. See also Fig. 15.

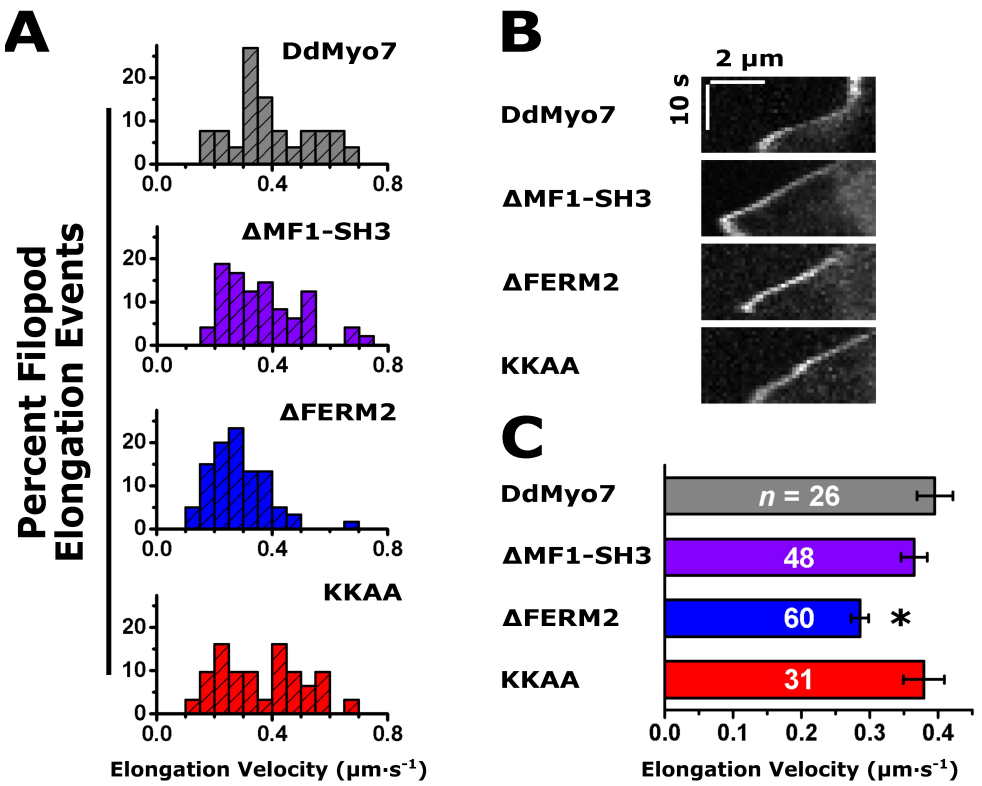


**Fig. 17. Filopod elongation velocity is reduced by deletion of the FERM2 domain.**

(A) Histograms of elongation velocity during filopod formation events are shown for full-length DdMyo7 and mutants (ΔMF1-SH3, ΔFERM2, KKAA). Y-axis is percent of total.

(B) Representative kymographs of filopod elongation in *myo7* null cells expressing DdMyo7 mutant proteins. Scale is 2 μm × 10 s.

(C) Filopod elongation velocity is significantly decreased 28% in the ΔFERM2 mutant (*, $p$ = .002) compared with full-length DdMyo7. The ΔMF1-SH3 and KKAA mutants do not differ significantly from full-length DdMyo7. Error bars are the SEM of the number of events $n$ (shown; see also

Table **6**).

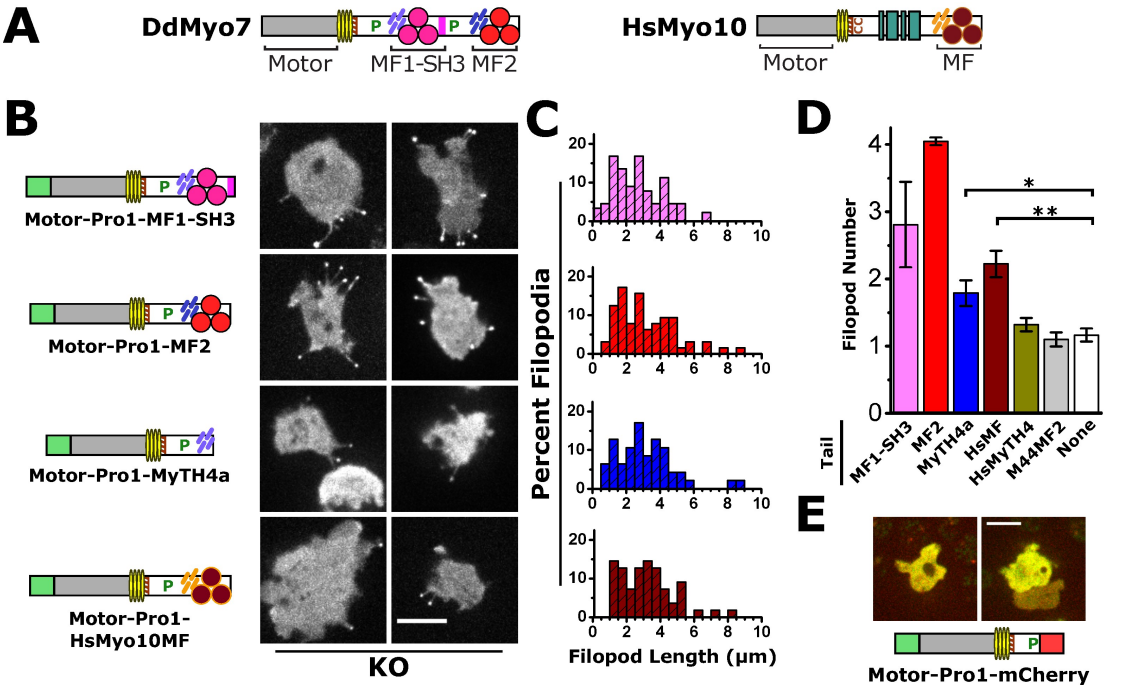


**Fig. 18. Conservation of the requirement for a single MyTH4-FERM domain for MF myosin filopod forming activity.**

(A) Domain structure of DdMyo7 and human Myo10.

(B) Representative images of cells with filopodia marked by the indicated fusion proteins. All mutants shown rescued filopod formation and strongly localized to filopod tips when expressed in *myo7* null (KO) cells. Scale, 10 µm.

(C) Histograms of filopod length in measured in KO cells expressing the indicated fusion proteins. Y-axis is percent of total (see also Table 8).

(D) Filopod number in KO cells expressing the motor-Pro1 fused to the indicated tail domains. Filopod number was defined as total filopodia during 10 s time lapse observation divided by number of cells with filopodia. Weighted mean filopod number is shown with SEM of 3-9 independent experiments. Multiple ANOVA analysis ($n$ = 10-50 cells) confirms significant increases in filopod formation for the MyTh4a (*, $p<.05$) and HsMyo10MF (**, $p<.01$) chimeras (see Table 8; MF1-SH3 and MF2 data excluded from ANOVA due to their much larger variance).

(E) Domain structure of motor-Pro1-mCherry fusion protein and confocal fluorescence images showing merged GFP and mCherry channels (scale 10 µm). The expressed protein is cytosolic, lacks membrane enrichment and does not support filopod formation.

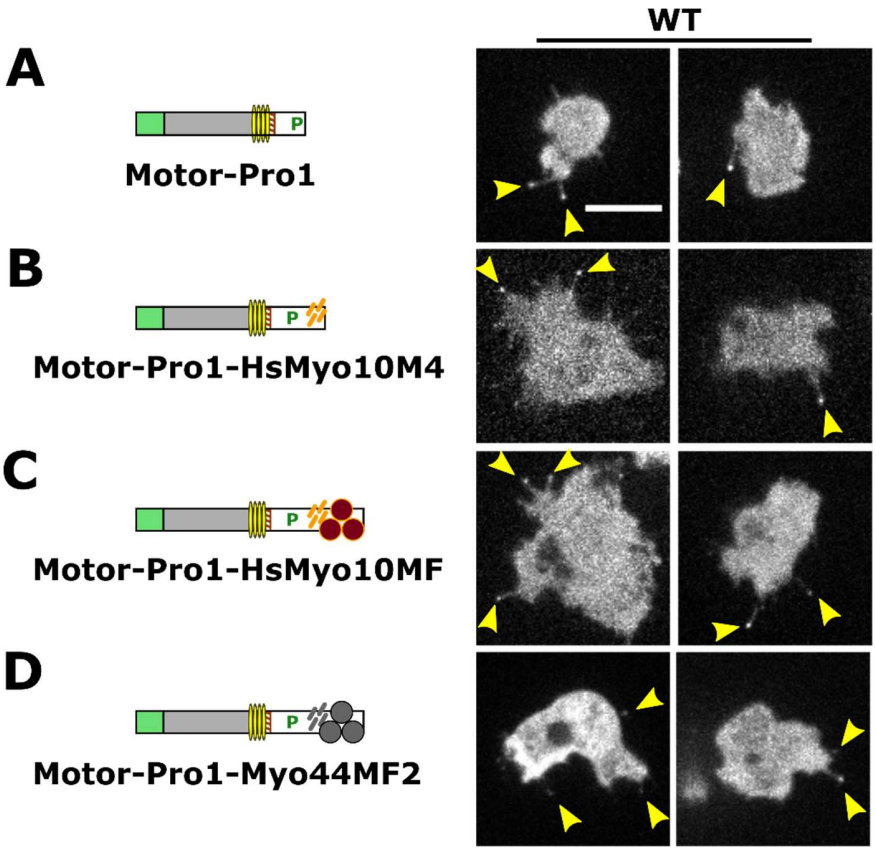


**Fig. 19. Localization of DdMyo7 mutants with chimeric tail domains in wild type cells.**

DdMyo7 mutants expressed in wild type (WT) cells were imaged by confocal microscopy. The domain organization of DdMyo7 mutants is shown on the left and fluorescence images on the right.

(A) GFP-tagged motor-Pro1 is shown. Note localization at filopodia tips (arrows).

(B) The equivalent proteins fused at the C-terminus with human Myo10 MyTH4 domain (HsMyo10M4), (C) human Myo10 MF domain (HsMyo10MF), or (D) Dictyostelium Myo44 MF2 domain. Scale, 10 µm. See also Fig. 18 and Table 8.

# 3 Biophysics of Myosin Function

The motor function of myosin is determined by its structure, chemical kinetics, and thermodynamics. The mechanochemical cycle of myosin converts the binding energy of ATP into mechanical work through conformational change in the converter subdomain and light-chain binding (lever arm) domain. Conformational changes are coupled to the enzymatic cycle, with ATP hydrolysis making the cycle essentially irreversible:

$$\mathrm{ATP}^{4-} + 2\mathrm{H_2O} \rightarrow \mathrm{HPO_4^{2-}} + \mathrm{ADP}^{3-} + \mathrm{H_3O^+} \qquad 3\text{-}1$$

Physiological studies are indispensable to decipher how molecular perturbations affect function at the cell, tissue or organism level, as demonstrated in the previous chapter. However, correct interpretation of physiological results requires carefully designed biophysical studies to understand the contribution of myosin at the molecular level. This chapter will briefly survey the field of myosin biophysics with a focus on fluorescence. Fluorescence spectroscopy methods are presented in Chapter 4, followed by a summary of progress toward *in vivo* myosin biosensors in Chapter 5.

## 3.1 Historical Overview

Striated muscles are highly ordered tissues that are ideally suited for anatomical or ultrastructural studies at every length scale, from low magnification optical microscopy to electron microscopy. Muscle has strong optical activity as a result of its linear ordering, providing high contrast in polarized light microscopy and birefringence measurements

(232, 233). It was appreciated as early as 1930 that the birefringence of actomyosin is a molecular property, not merely a consequence of muscle ultrastructure (234). The discovery of the ATPase activity of myosin by Engelhardt and others (235, 236) provided further evidence of mechanochemical coupling in muscle, and in 1944 it was found that addition of ATP to the actomyosin rigor complex induced myosin to dissociate from actin, increasing the observed birefringence consistent with the increased electric dipole moment of the bare actin filaments (237). This provided clear evidence that myosin enzymatic activity was coupled to actin binding.

The first detailed studies of muscle ultrastructure were performed by Hugh Huxley (238). In 1957 Huxley used electron microscopy, combined with careful interpretation of thin cross-sections of muscle, to show that striated muscle contains linear paracrystalline arrays of actin and myosin filaments along with repeating units of other proteins present in the sarcomere. Huxley had observed that muscle fibers produced coherent diffraction patterns in small-angle X-ray scattering studies in the early 1950's. Technical limitations hindered progress until 1967 when Huxley and Brown showed changes in the diffraction amplitude pattern correlated with formation of myosin-actin "cross-bridges" during muscle contraction (239).

## 3.2 Crystallography and Cryo-Electron Microscopy

Progress in understanding kinetics and mechanics of muscle myosin proceeded rapidly in the 1970's and 1980's yet structural progress was slow, albeit with advances in some

areas including proteolytic digestion and mapping with photoreactive nucleotide analogs. Myosin was first successfully crystallized by the Rayment group (240, 241). This structure showed nucleotide-free (i.e., post-powerstroke) skeletal myosin motor domain with a partially resolved light-chain binding domain. This was followed by a succession of *Dictyostelium* MhcA (DdMhcA) structures with a variety of nucleotide analogs mimicking intermediates in the mechanochemical cycle. However, for technical reasons, the *Dictyostelium* protein was truncated before the light-chain binding domain. The first clear picture of myosin in a pre-powerstroke conformation arrived from the Cohen group: smooth muscle myosin with bound ADP·$AlF_4$ (an ADP·$P_i$ analog) showing a 'bent' light-chain binding domain as predicted from mechanistic considerations (242).

The first crystallographic structures of myosin with fully resolved light-chains were produced by the Cohen group[1], showing scallop adductor muscle myosin in nucleotide-free (post-powerstroke), ADP, and ADP·$VO_4$ (pre-powerstroke) states (243, 244). These structures set scallop myosin as a reference point for modeling the lever arm rotation of myosins such as DdMhcA.

The actin-myosin complex has proven resistant to crystallization. Since the structural changes within myosin bound to actin are of great interest, the Holmes group made early attempts to model the complex with small-angle X-ray scattering data (245) and later with

[1] To date the only fully resolved myosin + light chain crystal structures are those of the Cohen group.

cryo-EM data at 14Å resolution (246). The first medium-resolution cryo-EM structure was produced by the Raunser group showing *Dictyostelium* Myo1E bound to actin-tropomyosin filaments at 8Å (247)[2]. This was followed recently by the structure of human non-muscle myosin 2C bound to actin-tropomyosin at 3.9Å (248). A forthcoming structure from the Alushin and Bryant groups shows Myosin VI bound to actin at 4.5Å (249). A current trend that shows great promise is the combination of available crystal structures with new, high-resolution cryo-EM structures to create a fully populated model of myosin's mechanochemical cycle (250).

While crystallography and electron microscopy have revealed myosin structures in atomic detail, including the structures of strongly-bound actin-myosin complexes, these methods share an inherent weakness: in computation of average structures, rare or short-lived intermediate structures may be lost. Furthermore, both techniques are severely limited in their ability to report structural dynamics. A complete understanding of how the structural transitions of myosin are regulated requires methods that observe myosin during its mechanochemical cycle. This has been best achieved with fluorescence spectroscopy as detailed next.

[2] An unnatural scenario since *Dictyostelium* lacks tropomyosin.

## 3.3 Fluorescence Spectroscopy

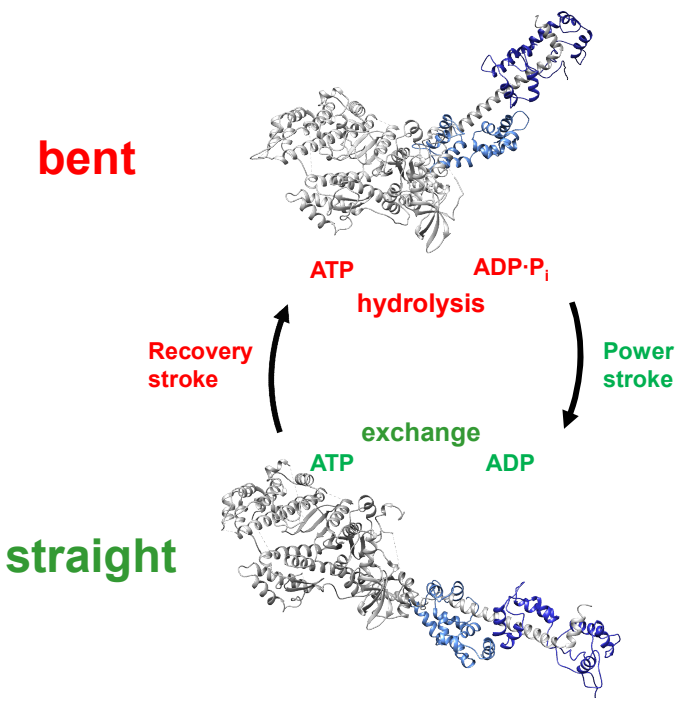


**Fig. 20. Structural Transitions in Myosin.**

Fluorescence methods have been applied to study myosin structure and kinetics in great depth (251). This section will focus on approaches to testing the correspondence of light-chain binding domain orientation and nucleotide state of the motor domain observed in static structures (5, 21). The light-chain binding domain is believed to rotate as a lever arm during the powerstroke (Fig. 20). A common approach to detecting this conformational change is to place a fluorescent donor probe on the motor domain and a fluorescent acceptor probe on the light-chain helix or light chains (Fig. 21). By choosing probes with overlapping donor emission and acceptor absorption spectra, and using site-directed attachments to create a spatial resonance overlap of the donor and acceptor electronic dipoles, the change in distance can be measured using the Förster equation as loss of donor fluorescence and/or appearance of acceptor fluorescence (252).

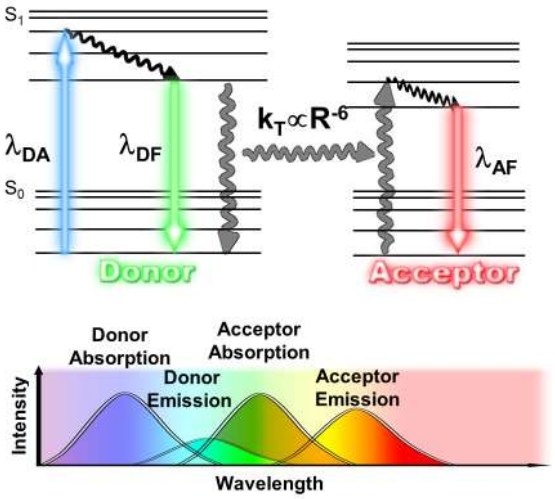


**Fig. 21. Förster Resonance Energy Transfer (FRET)**
(Top left) Energy levels of the donor molecule are shown: ground state ($S_0$) and electronically excited state ($S_1$). Following vibrational relaxation (~$10^{12}$ $s^{-1}$) the donor decays by fluorescence (~$10^9$ $s^{-1}$) or resonance energy transfer to the acceptor ground state (top right). FRET occurs when the donor emission and acceptor absorption bands overlap (bottom panel) and the probes are separated from spatial overlap of electron orbitals ($R$ > 2 nm) but close enough for resonance overlap proportional to $R^{-6}$.

In early example of this approach, the Sutoh group used truncated *Dictyostelium* MhcA motor domain expressed with N-terminal GFP and C-terminal BFP tags (253). The purified protein showed large FRET efficiency in the nucleotide-free (apo) state that decreased modestly with ADP and most strongly with ATP (relaxation). Although these results were promising, several challenges to reproducing and extending these results were identified (254), namely fluorescent protein photophysics, rotational dynamics, and photobleaching (photodepletion). These challenges arise in all fluorescent protein applications but will be examined using the example of the Sutoh study.

First, photophysical changes occurred in GFP when it was in contact with BFP, leading to excited state proton transfer to the donor that decreased the calculated FRET efficiency to 44% from its true value of 70%. This showed that although fluorescent proteins are generally resistant to environmental effects on fluorescence, it is essential to control for

intermolecular interactions that may affect energy transfer.

Second, rotational dynamics of fluorescent proteins (molecular weight ~ 26 kDa) are substantially slower (>10 ns) than the donor lifetime (2-5 ns) making the orientation of the donor and acceptor virtually static with respect to fluorescence. Thus it is necessary to model the restricted orientation distribution of the fluorescent protein (255–257) or establish that the orientation is isotropic (the best case scenario for current probes). The effect of the static isotropic distribution on calculated distance is easily corrected (258).

Finally, early generations of fluorescent protein such as BFP and YFP were highly prone to photobleaching (irreversible loss of fluorescence due to bond breaking). Current fluorescent proteins are more stable, and experimental design minimizes these effects (259).

Shih et al. took the approach of engineering a ‘Cys-lite’ version of DdMhcA, removing surface-reactive cysteine residues (260, 261). This permitted site-directed labeling with chemical dyes reactive with engineered surface cysteines. An Oregon Green donor was attached to the RLC and a tetramethylrhodamine acceptor was placed in the upper subdomain of the motor. Both dyes are environmentally insensitive, rotate rapidly due to their small size, and are relatively resistant to photobleaching; thus, the difficulties seen with fluorescent proteins were mostly avoided. The authors measured changes in the donor fluorescence lifetime using a frequency-domain method, but other methods are available such as time-domain lifetime measurement and spectral recording (Fig. 22). The average

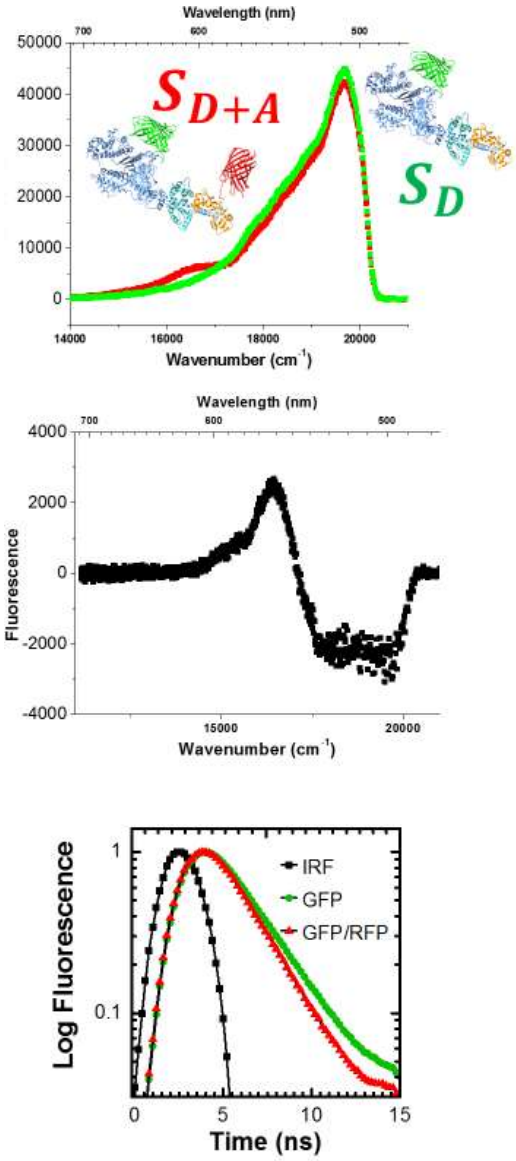


**Fig. 22. Comparison of Fluorescence Emission Spectrum and Lifetime.** (Top) Fluorescence spectra of GFP-MhcA ($S_D$) and GFP-MhcA+RLC-RFP ($S_{D+A}$) upon excitation of GFP; (Middle) Difference spectrum showing RFP sensitized emission; (Bottom) GFP donor or donor/acceptor (GFP/RFP) fluorescence lifetime measured by time-correlated single-photon counting (TCSPC). Instrument response function (IRF), black squares.

FRET efficiency increased from 16% (apo) to 36% (ATP) and 61% (ADP·$VO_4$). Since vanadate ion is thought to stabilize a pre-powerstroke conformation, the authors argued that the intermediate FRET value seen with ATP (relaxation) represented a mixture of pre- and post-powerstroke states.

Despite the early success of Shih et al.'s approach, technical limitations in protein production made reproduction of their approach virtually prohibitive (262). A hybrid approach was taken by the Thomas group using a Cys-lite, truncated MhcA motor domain with site-directed labeling of the relay helix, an internal helix that communicates changes in the nucleotide binding site to the converter subdomain. Analysis based on crystal structures predicted the C-terminal end of the helix would move nearly 1.5 nm during the powerstroke, in a 'bent-to-straight' transition

mirroring the straightening of the light-chain binding domain. Time-domain FRET studies confirmed this was the case, highlighting the role of phosphate release in gating the structural transition of myosin (263, 264) (20, 265).

All the approaches mentioned focus on fluorescence spectroscopy of myosin in purified solutions. While this is an essential step in validation of any biosensor, few attempts have been made to study myosin lever arm rotation in living cells; in a notable exception, the Uyeda group used spectral recording to measure force-dependent spectral changes in GFP (266, 267), but the artificial design of this sensor (a tandem dimer) limits its applicability.

Understanding myosin physiological function requires detailed knowledge of the spatial and temporal regulation leading to activation of myosin, as well as the effect of actin-myosin and myosin-cargo interactions on force generation, attachment and detachment. An ideal assay would measure both the biochemical and mechanical states of myosin in the cell, correlating the results to understand the mechanisms of regulation.

## 3.4 Biochemical and Mechanical Assays

Biochemical studies of myosin activity have long focused on kinetic measurements of ATPase activity (268), with maximum ATPase velocity $v_0$ related to total cycle time by:

$$v_0^{ATPase} = \frac{1}{t_{cycle}} \qquad 3\text{-}2$$

Mechanical activity of myosin can be measured using a method known as the unloaded

*in vitro* motility assay (unloaded because filaments in solution experience negligible drag). The assay measures the maximum velocity of actin filament translocation (269):

$$v_0^{motility} = \frac{d}{t_{strong}} \qquad 3\text{-}3$$

Where *d* is the distance travelled by the lever arm during the powerstroke and $t_{strong}$ is the time that myosin is strongly bound to actin. The distance *d* may be directly measured using optical trapping techniques or calculated from ATPase and motility data:

$$v = v_0 \frac{[\mathrm{ATP}]}{K_m + [\mathrm{ATP}]} \qquad 3\text{-}4$$

$$\text{Duty Ratio} \stackrel{\text{def}}{=} \frac{t_{strong}}{t_{cycle}} = \frac{K_m^{ATPase}}{K_m^{motility}} \qquad 3\text{-}5$$

$$d = v_0^{motility} \cdot t_{strong} = \text{Duty Ratio} \cdot \frac{v_0^{motility}}{v_0^{ATPase}} \qquad 3\text{-}6$$

Where Eq. 3-4 is the Michaelis-Menten equation for ATPase activity in the presence of saturating F-actin. The duty ratio is the fraction of myosin that is strongly bound to actin in the presence of saturating ATP and is defined in kinetic terms in Eq. 3-5 (270)[3]. The powerstroke distance *d* is given in Eq. 3-6; note that calculation of $t_{strong}$ is implicit.

More physiologically relevant quantities are the ensemble force and the power (272),

[3] Duty ratio of some myosins may be measured by fluorescence quenching of pyrene-actin (271)

i.e., the mechanical work performed by myosin per unit time, defined as

$$F_{ensemble} = N_{total} \cdot \text{Duty Ratio} \cdot f_{int} = N_{strong} \cdot f_{int} \quad 3\text{-}7$$

$$P_{int} = f_{int} \cdot v(T) \quad 3\text{-}8$$

$$P_{ensemble} = N_{strong} \cdot f_{int} \cdot v(T) \quad 3\text{-}9$$

Where $f_{int}$, the intrinsic force generated by myosin, is a molecular property related to the efficiency of the motor that is effectively constant (273–275). The velocity $v(T)$ is highly sensitive to the local tension $T$ applied to the cargo and/or the actin filament (6, 276) as well as the local concentrations of ATP and accessible binding sites on actin. This highlights the need to develop molecular tension sensors to detect the average local tension experienced by a myosin motor, a task that has not been convincingly attempted. The ensemble force (Eq. 3-7) does not require a molecular tension sensor as the force can be measured directly, without knowledge of the local velocity. Specifically, the ensemble force depends on the number of myosin molecules in the ensemble, $N_{total}$, and the fraction of strongly bound myosin molecules (the duty ratio). Since $N_{total}$ is readily estimated by imaging, design of cellular biosensors should focus on detection of the strongly-bound post-powerstroke state (duty ratio) to enable measurement of the myosin ensemble force.

Measuring the duty ratio of myosin motors requires a technique that can resolve structural conformations within an ensemble, either in solution with purified proteins or in a cell. Time-resolved FRET provides an avenue to use spectroscopy to directly measure the duty ratio, and with it the ensemble force generated by myosin. As a preliminary step to development of myosin biosensors, rapid high-precision time-domain fluorescence

lifetime methods were developed as described in Chapter 4. Preliminary application to a myosin 2 biosensor expressed in *Dictyostelium* is reported in Chapter 5.

# 4 Fluorescence Lifetime Plate Reader: Resolution and Precision Meet High-Throughput[1]

## 4.1 Chapter Summary

We describe a nanosecond time-resolved fluorescence spectrometer that acquires fluorescence decay waveforms from each well of a 384-well microplate in 3 minutes with signal-to-noise exceeding 400 using direct waveform recording. The instrument combines high-energy pulsed laser sources (5-10 kHz repetition rate) with a photomultiplier and high-speed digitizer (1 GHz) to record a fluorescence decay waveform after each pulse. Waveforms acquired from rhodamine or EDANS dyes in a 384-well plate gave lifetime measurements 5- to 25-fold more precise than the simultaneous intensity measurements. Lifetimes as short as 0.04 ns were acquired by interleaving with an effective sample rate of 5 GHz. Lifetime measurements resolved mixtures of single-exponential dyes with better than 1% accuracy. The fluorescence lifetime plate reader enables multiple-well fluorescence lifetime measurements with an acquisition time of 0.5 s per well, suitable for

[1] Reprinted from: Petersen KJ, Peterson KC, Muretta JM, Higgins SE, Gillispie GD, Thomas DD. 2014. Fluorescence lifetime plate reader: Resolution and precision meet high-throughput. *Review of Scientific Instruments*. 85(11):113101. PMCID: PMC4242087, with the permission of AIP Publishing. 

high-throughput fluorescence lifetime screening applications.

## 4.2 Introduction

Fluorescence spectroscopy provides exceptional sensitivity for biological assays, because the fluorescence emission signal is readily separated from excitation and background fluorescence wavelengths, but its precision is limited by the inherent variability of fluorescence intensity (277, 278). Intensity-based measurements are subject to noise due to uncertainty in optical path length or assay volume, light scatter from surfaces or contaminating particulates, differences in local concentration of fluorophores, or presence of interfering fluorescent compounds (279). Nanosecond time-resolved fluorescence measurements provide a means to improve assay resolution and precision, because the time-resolved signal is largely independent of intensity variations (280). The fluorescence lifetime (an observable related to the quantum yield) may be used to analyze fluorescence decay waveforms by methods including moment analysis (281), multi-exponential fitting (282, 283), or phasor analysis (284). Fluorescence lifetime detection is most useful in assays sensitive to probe environment, such as fluorescence quenching, resonance energy transfer, or intrinsic fluorescence (252). Lifetime-based assays have been used to measure macromolecular interactions (284, 285), distances (286, 20), and forces (287) as well as enzyme activity and ligand binding (288–290).

High-precision lifetime measurements are typically performed with time-correlated single-photon counting (TCSPC) (291), a digital method that employs low-intensity

excitation at the expense of long acquisition times (typically seconds or longer to obtain signal-to-noise ≥ 100). The alternative method of direct waveform recording (DWR) acquires analog fluorescence decays in response to high-intensity pulsed excitation (292). DWR dramatically reduces acquisition time from ~10 s to ~0.1 ms, without sacrificing accuracy or precision, by exciting many probe molecules with a single pulse and detecting thousands of emitted photons (292). We have demonstrated that this technology enables the acquisition of hundreds of high signal-to-noise waveforms with nanosecond time resolution and kHz repetition rate following stopped-flow (20, 293). We have developed a new instrument to enable high-throughput sample preparation and detection in a 384-well microplate format. Here we present a description of the NovaFluor Plate Reader that has already been employed in high-throughput studies (294, 295). We show here that fluorescence lifetime measurement in this instrument dramatically improves measurement precision relative to fluorescence intensity, without sacrificing throughput, in addition to its benefits for signal resolution, in a fluorescence lifetime plate reader.

## 4.3 Materials and Methods

### 4.3.1 Instrument

The NovaFluor plate reader (Fig. 23) was designed and built by Fluorescence Innovations, Inc. We performed 355 and 532 nm excitation with a 10-kHz pulse rate using an yttrium-aluminum-garnet microchip laser (JDS Uniphase) followed by a frequency multiplier and bandpass filter. We excited at 473 nm with a 5-kHz pulse rate using an FP2-473-3-5 microchip laser with LD-702 controller (Concepts Research Corporation). Excitation light passed through a neutral density filter and then through a pinhole in a collector mirror fixed beneath the moving stage. Fluorescence was gathered by the parabolic mirror for detection. Emission filters (470/20 nm band pass or 590/10 nm band pass) were placed before the detector, a H10270-20 photomultiplier tube (Hamamatsu) operating at 400 V except as noted. Detector current was converted to voltage at 50 Ω by a custom circuit board based on a 1 GHz analog transient waveform digitizer (ATWD version 3.1) (296). Motors driving the X-Y stage, shutter, neutral density and emission filters were controlled by a second custom board. All controllers were routed to USB using an RS-232 serial adapter. Instrument control and data acquisition were performed with custom software on a personal computer. We used an Ophir PD-10v2 power meter to calibrate neutral density filter position.

Solid dyes were dissolved to ~1 mM in spectroscopic grade ethanol and stored at -20 °C, except EDANS (5-((2-aminoethyl) amino) naphthalene-1-sulfonic acid) which was

dissolved in *N, N*-dimethyl-formamide. Working solutions were diluted to 1 μM (except as noted) in de-ionized water. Rhodamine B and 6G were excited at 473 nm, EDANS at 355 nm, and Rose Bengal at 532 nm. Fluorescence decays were acquired (**Fig. 24**) using a neutral density filter to adjust the peak signal to near 100 mV with 50-150 mV as an optimal range (1-3 mA peak output current of the PMT). We recorded decay waveforms with 640 samples at 0.2 ns resolution (128 ns total time). The signal delay was adjusted to allow at least 40 samples (8 ns) of pre-excitation data used to adjust the signal baseline.

### 4.3.2 Microplate Preparation

We loaded plates manually with a multichannel pipet (ThermoFisher) or automatically with a FlexDrop IV dispenser (PerkinElmer). We used well volumes of 50 or 100 μL in a 384-well glass-bottomed Greiner SensoPlate. Dye mixtures were dispensed in volumes with 5 μL increments. Plates were spun briefly (up to 300 rpm in Eppendorf rotor 5810R A-4-81) to remove air bubbles. The instrument response (IRF) was influenced by choice of laser, PMT voltage, and other factors and was acquired daily from a single well of de-ionized water with neutral density filter adjusted to a 100-mV peak signal.

### 4.3.3 Data Analysis

Analysis of total fluorescence and first moment was performed in Microsoft Excel or Matlab (MathWorks). Total fluorescence was calculated as $\sum_i F(t_i)$, where $F(t)$ was the signal intensity after baseline correction. Lifetime analysis used custom software to simulate exponential decays convolved with the measured IRF for fitting using nonlinear

least-squares (Levenberg-Marquardt algorithm.) For single dyes, a lifetime model was used:

$$F(t) = A \exp\left(-\frac{t-\Delta}{\tau}\right) \qquad 4\text{-}1$$

Where $A$ was the amplitude of fluorescence, $\tau$ was fluorescence lifetime, and $\Delta$ was a parameter accounting for time shift between the signal and the IRF.

Mixtures were averaged across replicate wells and fit to:

$$F_j(t) = C_j\{x_j A_1 \exp\,[-(t-\Delta)/\tau_1] + (1-x_j)\,A_2 \exp\,[-(t-\Delta)/\tau_2]\} \qquad 4\text{-}2$$

Where $x_j$was the mole fraction in the $j$-th mixture and $C_j$ was a scaling factor to account for intensity-dependent noise. Lifetimes $\tau_1, \tau_2$were globally constrained (283) to the values obtained for pure dye. Time shift $\Delta$ and amplitudes $A_1, A_2$ were globally fit. Amplitude terms reflected the combined effect of extinction coefficient and quantum yield in the two dyes and fraction $x$ represented the ratio of dye molecules. We found constraining the start ($x = 0$) and end fractions ($x = 1$) using single dyes improved fit accuracy.

Raw first moments were defined as $\sum_i t_i F(t_i)/\sum_i F(t_i)$ and adjusted using exponential depression (297) to suppress noise at longer time intervals. We used the raw first moment $\mu^0$ to calculate a depression function, $\exp(-t/\beta\mu^0)$. Larger $\beta$ values increased agreement of the moment and lifetime values, but decreased precision. We found

$\beta = 3$ was sufficiently small to maintain precision. The adjusted first moment

$$\mu = \frac{1+\beta}{\beta}\left[\frac{\sum_i t_{\mathrm{i}} \exp(-t_i/\beta\mu^0)\, F(t_i)}{\sum_i \exp(-t_i/\beta\mu^0)\, F(t_i)}\right] \qquad \text{4-3}$$

was calculated by assuming that $F(t)$ was an exponential function (Eq. 1). Integration of Eq. 3 by parts would then yield $\mu = \tau$ in an ideal case where the IRF is infinitely steep.

## 4.4 Experimental Results

The NovaFluor plate reader is a nanosecond time-resolved spectrometer that uses pulsed laser excitation, a high-speed digitizer and a photomultiplier tube (PMT) detector to record fluorescence decays from each well of a microplate. The digitizer read time is approximately 1 ms per waveform for a 5-kHz laser source (interleaving over 5 pulses) and the transport time is 0.3 s per well. Typical acquisitions were averaged across 200 successive waveforms giving an acquisition rate of 0.5 s per well or 3 min per 384-well plate. We used single-lifetime dyes to determine the precision and resolution of the plate reader and to measure its signal-to-noise performance.

### 4.4.1 Lifetime Compared with Intensity

We used water-soluble dyes with a variety of lifetimes to measure instrument performance (Fig. 25). First, we measured the instrument response function (IRF) in pure water. We then selected an appropriate emission filter and adjusted excitation power with a neutral density filter to give a peak signal of 50-150 mV. Total intensity was measured as the fluorescence decay integrated across all time points of the acquired waveform. Lifetime and moment were determined from the waveform (see Methods).

The plate reader acquired lifetime data with better than 1% precision for dye lifetimes of 1.6 ns and higher. Precision was measured as coefficient of variation (CV = SD/mean). Lifetime measurements were up to 25-fold more precise relative to the simultaneous

**Table 9. Comparison of Precision for Intensity, Lifetime and Moment Measurements.**

| | Intensity CV | Lifetime (ns) | Lifetime SD (ns) | Lifetime CV | Moment (ns) | Moment SD (ns) | Moment CV |
|---|---|---|---|---|---|---|---|
| Rose Bengal | 7.17% | 0.040 | 0.011 | 27.50% | 1.187 | 0.004 | 0.34% |
| Rhodamine B | 3.47% | 1.566 | 0.010 | 0.67% | 2.476 | 0.009 | 0.37% |
| Rhodamine 6G | 6.99% | 3.914 | 0.011 | 0.27% | 3.357 | 0.008 | 0.25% |
| EDANS | 2.74% | 12.684 | 0.028 | 0.11% | 10.197 | 0.014 | 0.14% |

**Dyes were dispensed in uniform volume in microplates to measure signal precision across wells. Lifetime precision (coefficient of variation, CV = SD/mean) is superior to intensity precision in all but the shortest lifetime dye. Further enhancement of precision is seen in the adjusted first moment.**

measurement of total intensity. The ultra-short lifetime dye Rose Bengal fit to a single lifetime (0.04 ns) with low precision, although the standard deviation (11 ps) was comparable to that of other dyes.

We measured the precision of lifetime detection by uniformly dispensing dye into 384-well plates and measuring the DWR signal using the plate reader (Fig. 25). We fit the decays to a single exponential lifetime model (Eq. 1). We found rhodamine B lifetime had 5-fold improved precision compared with total intensity, while the longer lifetime dyes rhodamine 6G and EDANS showed a 25-fold relative improvement in precision (Table 9). We would expect DWR to have better precision for lifetimes that are long relative to the IRF (2.8 ns FWHM), and this is consistent with our results. In most cases, we found that well-to-well precision improved when analyzing half of each plate (192 wells) due to systematic errors in volume of liquid dispensed.

We also analyzed waveforms using first moment, a more direct analysis than the lifetime model. We found the raw first moment had poor precision and was sensitive to

noise during the later fluorescence decay, even when we truncated the data. The adjusted first moment (Eq. 3) had greater precision than was seen in the fitted lifetimes. The absolute value of the moment differed from the value of lifetime and was affected by experimental conditions such as PMT voltage.

We examined variation between wells by comparing total intensity with lifetime and adjusted first moment (Fig. 26). Lifetime values for the dyes in Table 9 were mostly randomly distributed, showing weak correlation with intensity (Pearson's correlation coefficient $r$ took values $|r| \leq 0.5$). Rhodamine 6G showed a moderately strong correlation ($r = 0.87$) with intensity, although the coefficient of variation remained less than 1%. We hypothesize that these correlations reflect a small nonlinear response in the detector and/or digitizer.

### 4.4.2 Linearity of Detection

Direct waveform recording requires fluorescence emission to be linearly related to signal intensity, since intensity-dependent variations could distort the waveform and fitted lifetime (292). We varied excitation power and sample concentration to determine whether nonlinearity affected instrument performance. First, we tested linearity of the total intensity measurement by reducing the excitation power in calibrated steps and measuring intensity of the ultra-short lifetime dye Rose Bengal, finding excellent agreement (Fig. 27). We defined an arbitrary unit of fluorescence as the total intensity of a given waveform with a 100-mV peak signal.

Next, we tested how fluorescence intensity varied with concentration of the short lifetime dye rhodamine B over a 50-950 nM range (Fig. 28) (a)) and found the expected linear relationship with a root-mean-squared deviation of 1.8%. For this experiment, each dye concentration was dispensed in 16 replicate wells. CV of intensity was 2%-6% in each set of replicates, and CV of lifetime was 1.64% across all wells, varying from 2.08% at 50 nM to 0.87% at 950 nM.

We further analyzed the effect of signal intensity on apparent lifetime by plotting lifetime and intensity for each well (Fig. 29). Lifetime values were increasingly variable below 0.5 A.U., while the instrument provided good precision for fluorescence signals in the range 0.5-1.5 A.U. The apparent lifetime showed a moderate positive correlation with intensity ($r = 0.70$) despite the overall low CV (1.6%). This correlation had minimal impact on precision when intensity variation was due to experimental error alone. For example, the data in Fig. 26 span a range of ~1.0-1.2 A.U. with a lifetime CV of 0.7%. The lifetime of rhodamine B (1.6 ns) was short compared to the IRF (2.8 ns) and thus was more affected by instrument nonlinearity than were the longer lifetime dyes.

### 4.4.3 Signal Quality

The instrument response function (IRF) had a measured FWHM of 2.3 ns (full width at half maximum) with 355 nm excitation and 2.8 ns with 473 nm excitation (Fig. 24). In all experiments, we acquired waveforms at 1 GHz with the ATWD digitizer and increased the effective sample rate to 5 GHz by interleaving each cycle of 5 laser pulses (Fig. 30 (a)).

We calibrated a series of onboard pre-trigger delays in 0.2 ns steps so that the delay incremented with each laser pulse. We verified the delay calibration by recording 200 successive 5 GHz waveforms of a rhodamine B sample and extracting the 1 GHz waveforms. We then fit the time delay relative to the IRF for each waveform and calculated mean offset values (Fig. 30 (b)). The observed offsets had better than 5% accuracy over 6 months compared with calibrated values.

The ability to precisely acquire lifetime data depends on the experimental signal-to-noise ratio (SNR), typically measured at the peak of the fluorescence decay (280, 292). We acquired 1000 signal-averaged waveforms from a sample of rhodamine 6G to estimate instrument noise from the variation in a single well. We calculated the SNR waveform (Fig. 31 (a)) as the signal of one waveform divided by the standard deviation at each time point. Peak SNR was inversely related to the detector voltage. At the low PMT voltage (400 V, a detector gain of about 1000) SNR peaked at 580 and dropped to 360 at higher PMT voltage (500 V, a detector gain of about 5000). These values were far above the desired threshold for precise lifetime detection (SNR $\geq$ 100).

The maximum signal-to-noise ratio was affected by the PMT voltage and the number of cycles averaged (Fig. 31 (b)). In the absence of averaging, SNR ranged from 40 at 400 V acquisition to 90 at 500 V. Averaging over 200 cycles per acquisition increased SNR better than 6-fold. Experimental sources of variation between wells had a large effect on lifetime precision relative to instrumental sources. We found a 384-well plate of rhodamine 6G that showed substantial well-to-well variation in observed lifetime (CV 1.62%) with

200 cycles of averaging showed nearly equal precision with 50 cycles of averaging (CV 1.64%) despite the nearly 50% decrease in SNR per well. Pulse interleaving had a modest effect in the presence of experimental noise. Interleaved waveforms (5 GHz) of the short lifetime dye rhodamine B were more precise across wells (CV 0.59%) than the same waveforms without interleaving (1 GHz, CV 0.87%).

### 4.4.4 Resolution of Lifetimes

We tested the ability of the plate reader to resolve two dyes with similar lifetimes (1.6 ns for rhodamine B and 3.9 ns for rhodamine 6G) and overlapping emission spectra by mixing the dyes in 384-well plate, incrementing the volume of each dye by 5% in each column of wells to maintain a total concentration of 1 μM (Fig. 32). We averaged 16 replicate wells at each concentration and fit the relative fraction of dye using a two-component model (Eq. 2). The fit recovered the true fraction with high accuracy (root-mean-squared deviation (RMSD) = 0.74% relative to the predicted mole fractions). The two-component mixture required averaging of replicate wells as fit results showed high variability (RMSD 2% or greater). Variability decreased to 1.08% RMSD with 4 replicates and 0.74% with 16. This result demonstrates the NovaFluor plate reader can resolve changes in lifetime with high accuracy, a key requirement for lifetime-based assays.

## 4.5 Discussion

Direct waveform recording (DWR) enables fluorescence lifetime acquisition in a microplate with a signal-to-noise ratio (SNR) of 400 or better while maintaining acquisition rates of 0.5 s per well. The plate reader acquires waveforms with high precision across a range of lifetimes, from short (1.6 ns, rhodamine B) to long (12.7 ns, EDANS). While there is great interest in developing long lifetime probes to improve the resolution of lifetime assays (289), the high precision of DWR permits the use of short lifetime probes as well. The per-well precision of lifetime measurement is routinely near 10 ps allowing us to resolve small changes in lifetime with high precision. The width of the IRF (2.8 ns) was not a barrier to analysis of short lifetimes, although the ultra-short lifetime dye Rose Bengal was unsuitable.

Fluorescence lifetime has a key advantage in high-throughput screening assays because it directly resolves interfering fluorescence signals (298) that are present in most screening compound libraries (299). The use of multiple-exponential fits to resolve compound interference is firmly established (278). We have shown (Fig. 32) that the DWR plate reader resolves the relative fraction present in a two-component mixture with better than 1% accuracy over a 20-fold concentration range, making it resistant to compound interference.

Acquisition rate has been a key limitation in applying fluorescence lifetime to high-throughput screening. We can compare DWR with photon counting methods of lifetime

detection by comparing peak SNR in each. In photon counting (280), SNR increases as $\sqrt{N}$, while DWR measures SNR as signal/SD of successive waveforms (292). Photon counting applications have been optimized for a CV of 0.5% acquired in several hundred milliseconds (300). If we assume a single 4 ns lifetime and 0.2 ns bins, this measurement would have a peak channel photon count of about 5,000 corresponding to an SNR of 70. This is comparable to our performance with no signal averaging (Fig. 31) and at least 5-fold worse than our actual SNR performance in a 0.5 s acquisition. In another example (290) a 5 MHz TCSPC instrument acquired 10,000 peak channel photon counts in 3 s, an SNR of 100. Increasing SNR to 400 would require ~50 s acquisition in this example. DWR provides SNR of 400 or greater in 200 ms (200 cycles averaged), at least 100-fold faster when compared with TCSPC. The transport time of the microplate stage (0.3 s) limits our plate reader to a per-well acquisition time of 0.5 s (200 cycles averaged). With this limitation, the two methods are roughly comparable in speed.

Several factors affect the per-well acquisition time. Waveform averaging provides some protection against fluctuations in the fluorescence signal on the ms time scale, e.g., due to motion of contaminating particulates. We routinely average 200 waveforms per well. Averaging is not necessary as instrument noise is quite low (~0.5 mV or less) providing high SNR. Reducing the number of waveforms to 50 modestly improves the acquisition time to 0.35 s, but may harm resolution. Similarly, pulse interleaving may be disabled to increase acquisition rate at a cost of decreased resolution of lifetime components. We are currently pursuing a rapid scan mode to decrease acquisition time to

0.1 s per well. Early results show SNR comparable to data acquired with 50 cycles averaged, a 3.5-fold improvement in speed.

Cost is another limitation in high-throughput screening assays. We have used costly glass plates in this study, but have tested plastic plates (polystyrene or cyclic olefin polymer) finding their precision is comparable. Plastic plates generate autofluorescence that hinders lifetime resolution. Assays that do not require resolution of component mole fractions may therefore benefit from plastic plates. We have begun development of a top-read format plate reader that enables use of lower cost polypropylene plates. Early results show comparable precision to that presented here (CV of lifetime better than 0.5%).

Direct waveform recording relies on the linearity of the analog current generated by the PMT. While the total intensity signal of our instrument is linear with excitation power (Fig. 27) and concentration (Fig. 28), nonlinearity results in a correlation of apparent lifetime with intensity. The nonlinearity is likely due to physical limitations in the PMT at high peak output current (2 mA for a 100-mV signal). High intensity signals thus produce slightly longer lifetimes. The effect is small (~50 ps per fluorescence unit, Fig. 29). We find nonlinearity has negligible effect when intensity varies due to experimental error alone (Fig. 26) as per-well precision (~10 ps) becomes limiting. Assays requiring full dynamic range should consider the effect of nonlinearity on apparent lifetime. This effect is a subject of ongoing study.

Other approaches to improving resolution of fluorescence assays include

homogeneous time-resolved fluorescence (HTRF) using long-lived lanthanide probes (301) or development of ratiometric assays that exploit changes in emission spectra, for example the ratio of donor to acceptor emission in a FRET pair (302). Both techniques limit the choice of probes available and do not eliminate the issue of signal precision common to intensity-based measurements. For applications requiring greater sensitivity and rejection of signal interference, enzyme-coupled bioluminescence assays remain the gold standard (298, 303).

Fluorescence lifetime has been pursued for improvement of high-throughput screening assays for many years. The high precision of DWR has enabled development of new types of fluorescence assays including time-resolved transient kinetics (293) and the recently reported time-resolved flow cytometry measurement of single cells (304). The NovaFluor lifetime plate reader demonstrates that direct waveform recording achieves excellent signal-to-noise and per-well precision while providing fast acquisition rates suitable for drug screening and other high-throughput applications.

## 4.6 Acknowledgements

This work was supported by NIH grants to DDT (R37 AG26160, R21 AG042996, R01 AR032961). KJP was supported by NIH training grant T32 AR007612. The NovaFluor plate reader was developed by Fluorescence Innovations, Inc. Spectroscopy experiments were performed at the Biophysical Spectroscopy Center, University of Minnesota. Computational resources were provided by the Minnesota Supercomputing Institute.

## 4.7 Figures

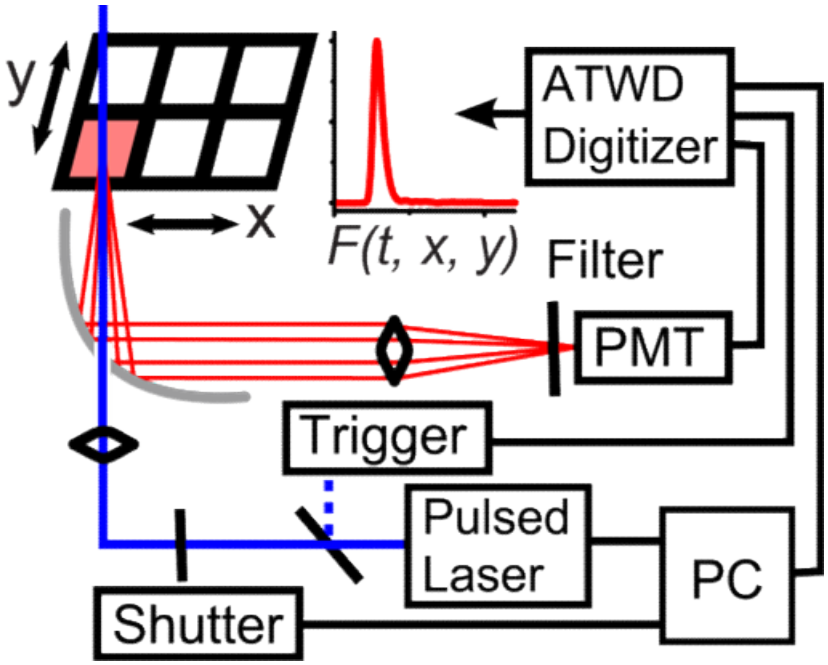


**Fig. 23. Fluorescence lifetime plate reader.**

The NovaFluor spectrometer uses an X-Y stage, pulsed laser, PMT and digitizer for direct waveform recording (DWR) of fluorescence lifetime decays. Excitation light is focused through a pinhole to the center of each well of a microplate. Fluorescence emission is collimated by a parabolic mirror and focused on the PMT. Fluorescence decays are digitized and acquired for lifetime or moment analysis.

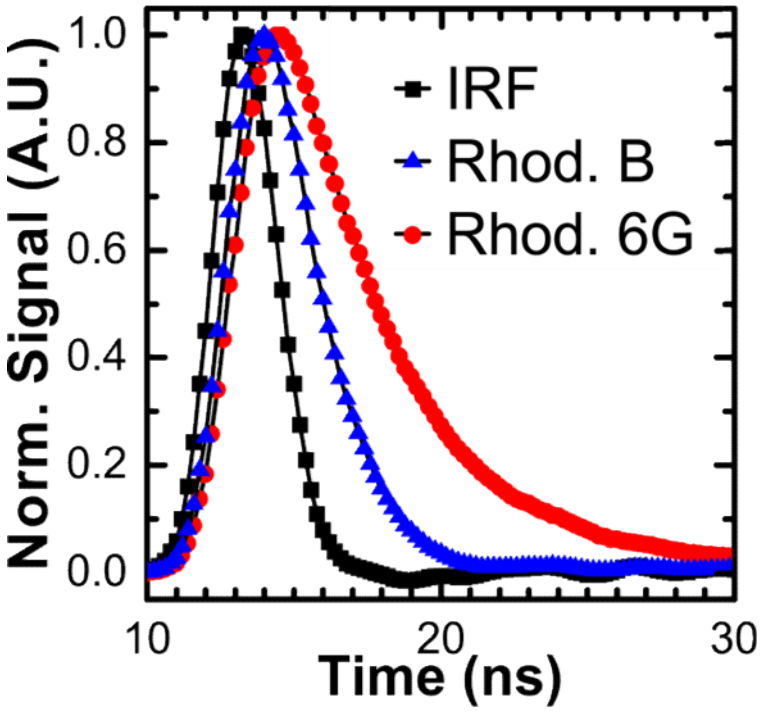


**Fig. 24. Direct Waveform Recording (DWR) of Fluorescence Decays.**

The instrument response function (IRF, black squares) acquired from scattering in water is shown with fluorescence decay waveforms for rhodamine B (blue triangles) and rhodamine 6G (red circles). Waveforms acquired by DWR at 400 V with 0.2 ns resolution. Signal does not start at time zero because pre-excitation data was used to adjust the Y-axis baseline for each normalized waveform.

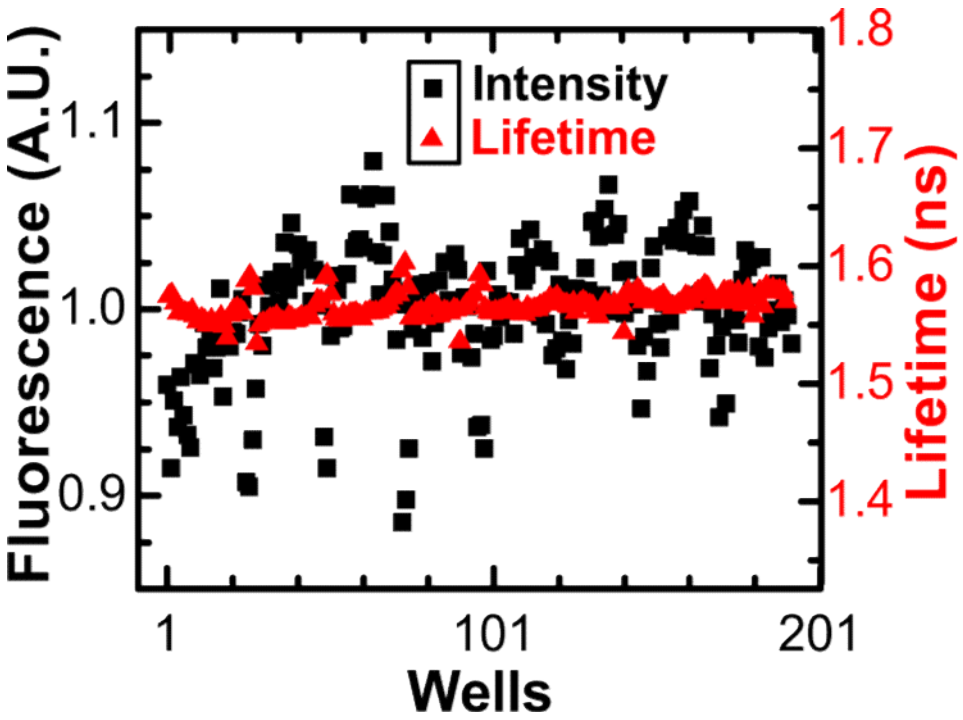


**Fig. 25. Fluorescence lifetime is more precise than fluorescence intensity.**

Intensity (black squares) and lifetime (red triangles) of rhodamine B (1 μM in water) were calculated from waveforms acquired in 192 wells of a 384-well microplate. Lifetime CV is 0.7% (coefficient of variation = SD/mean), 5-fold more precise than intensity CV (3.5%) for this short lifetime dye. Left axis is total intensity divided by mean and right axis is centered and scaled in proportion.

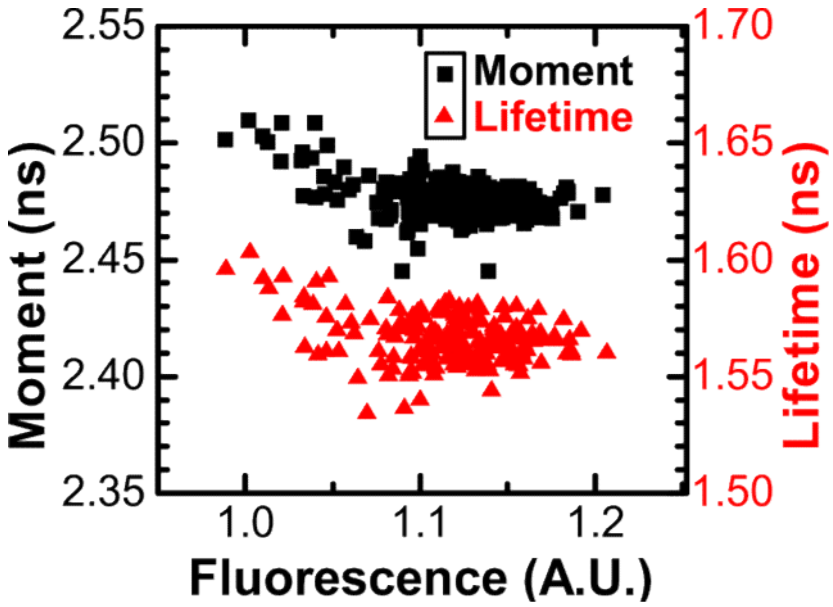


**Fig. 26. Lifetime and moment are precise across wells.**

Lifetime and adjusted moment of rhodamine B (1 μM in water) were calculated from the decay waveform in each well. CV was 0.67% (SD 10 ps) for lifetime and 0.22% (SD 9 ps) for moment. CV (coefficient of variation) = SD/mean. One fluorescence unit = total intensity given a peak signal of 100 mV.

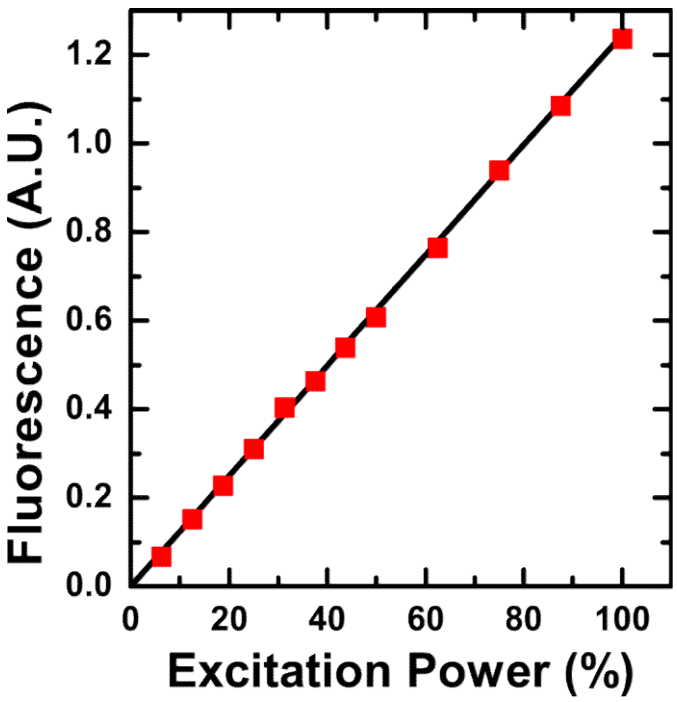


**Fig. 27. Linear dependence of fluorescence on excitation power.**

Incident power was varied by a neutral density filter to excite Rose Bengal (1 μM in water) in a single well. Total intensity (red squares) varied linearly ($r^2 > 0.999$; RMSD 0.90%). Black line is the predicted relationship, scaled to the unit intensity of a waveform at 100 mV peak signal.

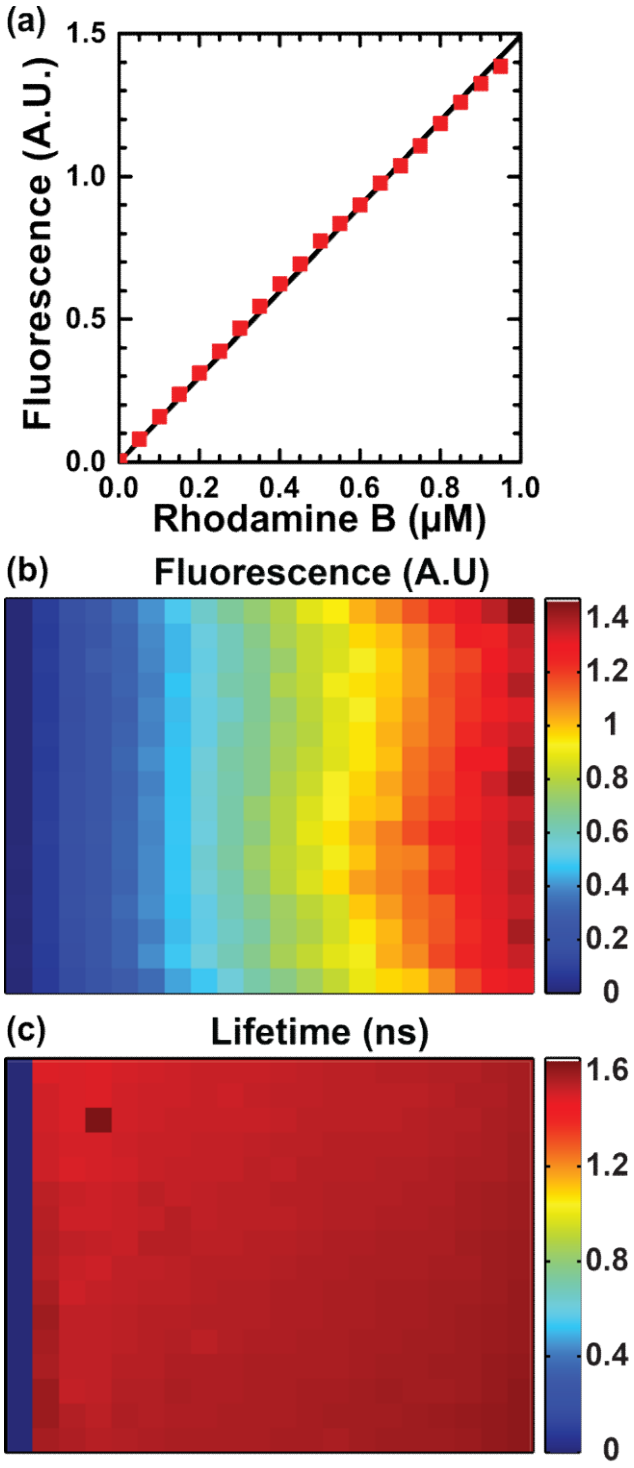


**Fig. 28. Fluorescence is proportional to intensity.**

(a) Fluorescence total intensity (red squares) of rhodamine B (0-950 μM in water) varies linearly with concentration ($r^2 > 0.999$; RMSD 1.8% relative to expected relationship shown in black line).

(b) Intensity map of plate shown in false color with dye concentration ranging from 0 (left column) to 950 μM (right column).

(c) Lifetime map of the same plate, with empty wells assigned a lifetime of zero.

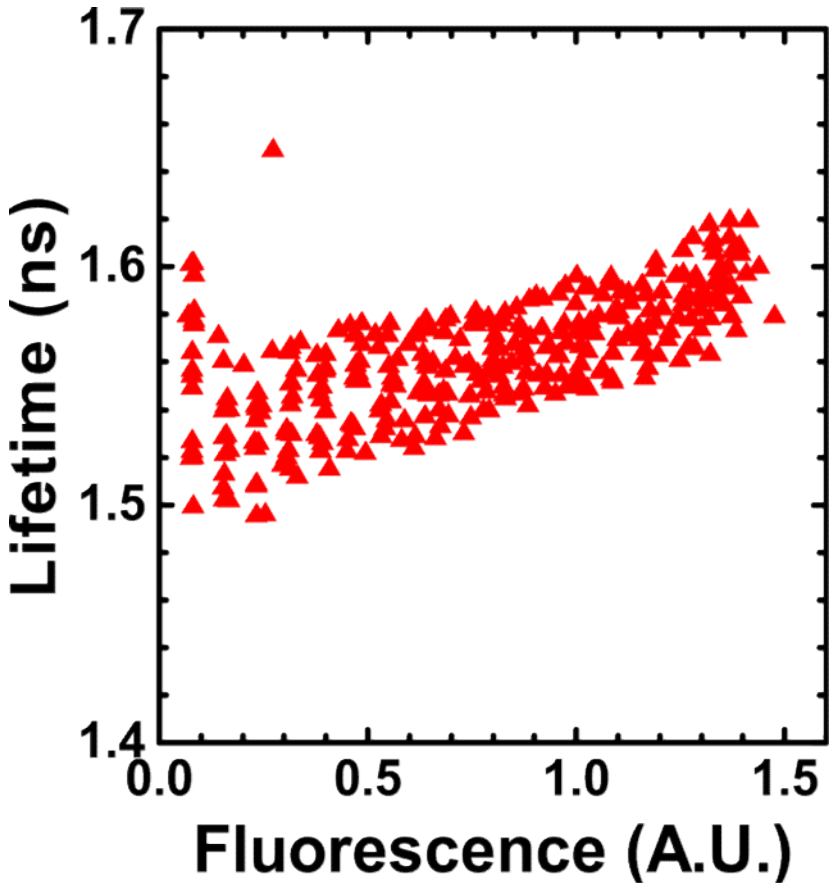


**Fig. 29. Distribution of apparent fluorescence lifetime and intensity.**

Fitted lifetimes (red triangles) were precise (1.6% CV) across a range of dye concentrations (50-950 μM rhodamine B in water). The apparent correlation of lifetime and intensity reflects detector nonlinearity. CV = coefficient of variation (SD/mean).

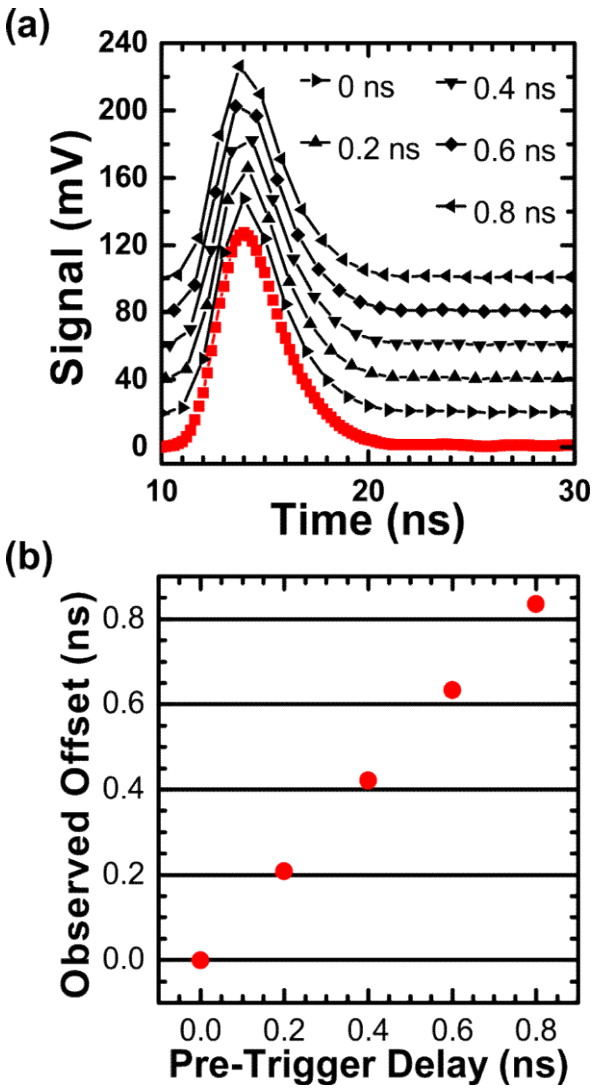


**Fig. 30. Pulse interleaving increases effective sampling rate.**

(a) The ATWD digitizer was calibrated to use a series of pre-trigger delays (black symbols: 0, 0.2, 0.4, 0.6 and 0.8 ns) on successive laser pulses. Each sequence of five 1-GHz acquisitions was combined into a single 5-GHz interleaved waveform (red squares).

(b) The true offsets (red circles) were measured by exponential fitting showing better than 5% agreement with calibrated values (X-axis), root-mean-squared deviation 2.8%.

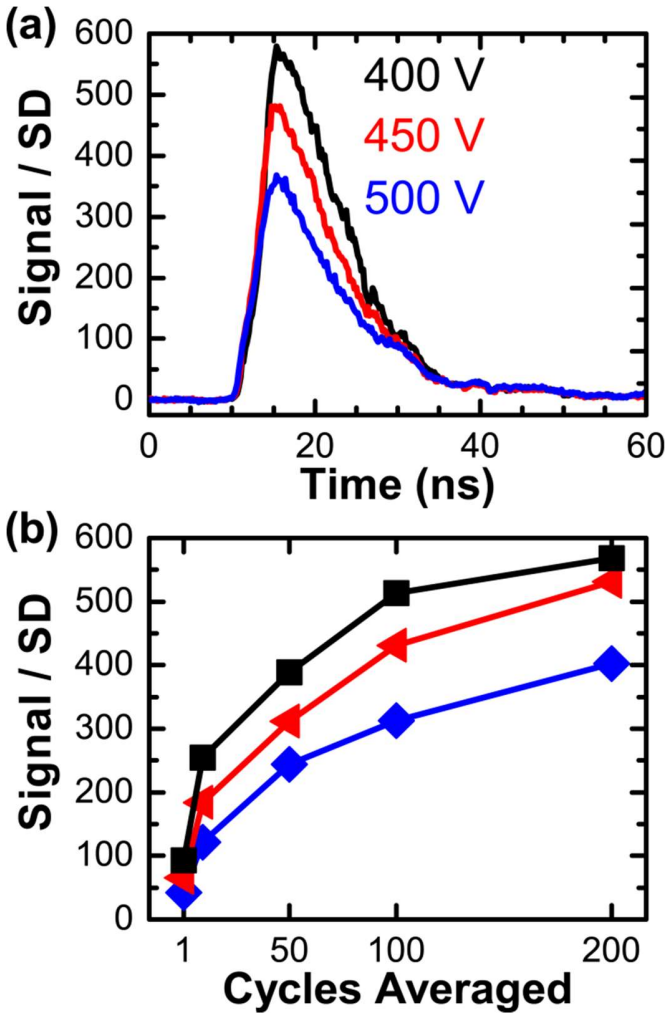


**Fig. 31. Direct waveform recording provides high SNR.** Signal-to-noise ratio (SNR, defined as signal/SD) was measured for 1000 successive acquisitions with 0.2 ns resolution. (a) SNR waveform of rhodamine 6G (1 μM in water) acquired with 200 cycle averaging of each waveform;

(b) Representative values of peak SNR of rhodamine 6G with varied number of cycles averaged. Peak SNR was highest (580) at low PMT voltage (400 V, black squares) and dropped to 360 at high PMT voltage (500 V, blue diamonds).

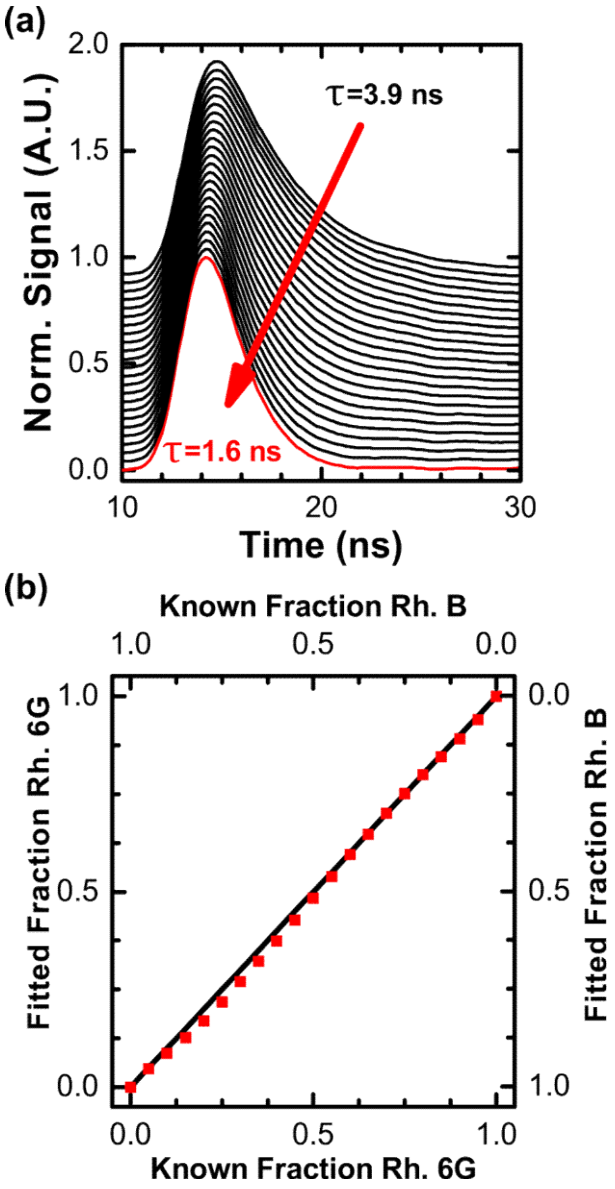


**Fig. 32. Fluorescence lifetime quantitatively resolves dye mixtures.** (a) Rhodamine 6G was mixed with rhodamine B in 5% volume steps (1 μM total, in water) for lifetime detection. (b) The mole fraction of rhodamine 6G was recovered with high accuracy by a two-component exponential fit (blue squares). Squared correlation coefficient $r^2 > 0.999$, root-mean-squared deviation 0.74% relative to the predicted relationship $x = y$ (black line).

# 5 Myosin Biosensors

Myosin motor activity is essential for its physiological function. A crucial measure of motor activity is the local ensemble force (see discussion, p.90) that is proportional to the number of available motors in the ensemble multiplied by their duty ratio, i.e., the number of strongly-bound, force-generating motors. A FRET biosensor strategy was pursued to resolve the strongly-bound state of myosin (Fig. 22). Time-domain fluorescence lifetime measurements can resolve multiple species with excellent precision (Fig. 32). The ability to express the sensor in cells without additional labeling was also a high priority.

*Dictyostelium* MhcA was tagged with a donor fluorescent protein at its N-terminus and RLC was fused with an acceptor fluorescent protein (Fig. 33). This design was predicted to show higher FRET in the pre-powerstroke, ATP-bound state and relatively lower FRET in the post-powerstroke, ADP-bound or apo states due to the motion of the lever arm and increased distance between the donor and acceptor molecules (Fig. 33C). Note that when actin is present, the pre-powerstroke states are associated with relaxation and the post-powerstroke states with rigor. The fluorescent MhcA and RLC were co-expressed in *mlcR*$^{-}$ cells (305) to prevent competition between endogenous and fluorescent RLC molecules. The fluorescent RLC rescued the *mlcR*$^{-}$ developmental phenotype indicating that its function was unharmed by fusion with the mRFP acceptor (Fig. 33D).

Finding that the two proteins were tolerated and expressed at high levels in *Dictyostelium,* cells expressing NowGFP-MhcA plus RLC-RFP-Δ93 or NowGFP-MhcA

plus WT RLC, were harvested ($5 \cdot 10^8$ cells each) in lysis buffer (50 mM HEPES, 2.5 mM EDTA, 1 mM DTT, pH 8.0) and lysed in 1% v/v Triton-X-100 (Anatrace).

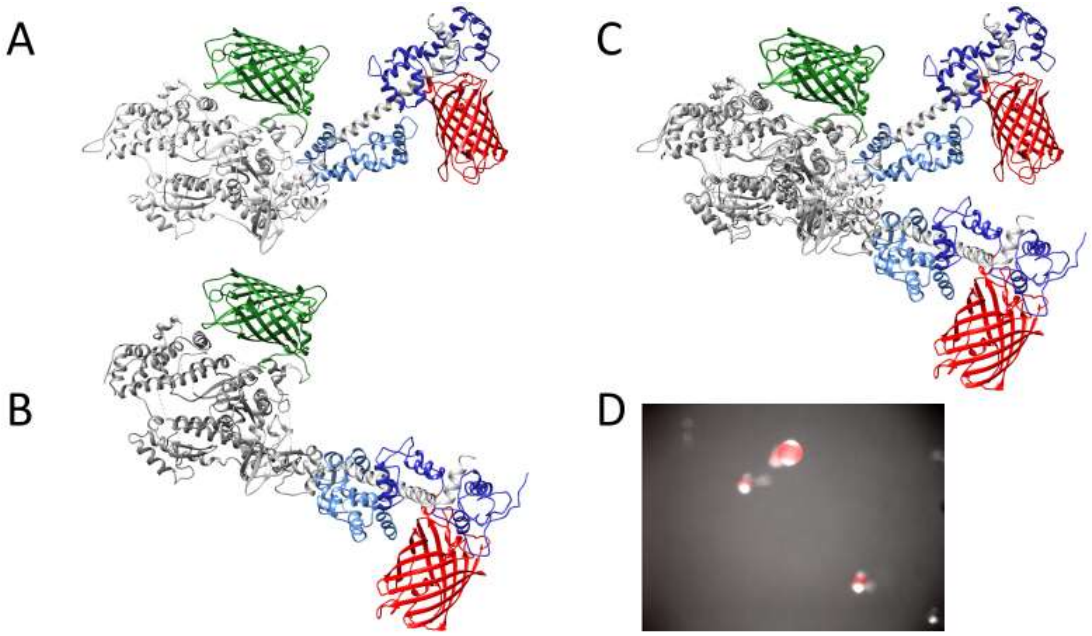


**Fig. 33. A *Dictyostelium* Myosin 2 FRET sensor.**

A fragment of DdMhcA encompassing the motor and light-chain binding domains (aa 1-821) with N-terminal 7xHis and NowGFP tags (306, 307) was co-expressed with RLC-RFP-Δ93 (mRFP inserted between EF2 and EF3 subdomains). (A) Ribbon model of the pre-powerstroke (bent, lever up) conformation modeled using PDB: 1DFL. Upper and lower actin binding sites are at left; (B) Model of the post-powerstroke (straight, lever down) conformation (PDB: 1DFK); (C) Superimposition showing lever arm rotation; (D) Brightfield micrograph of *mlcR*$^-$ fruiting body formation rescued with RLC-RFP- Δ93 (red fluorescence is overlaid).

Myosin was prepared by actin co-sedimentation and released with 20 mM MgATP (308). The partially purified myosin was dialyzed into assay buffer (10 mM Tris, 2 mM $MgCl_2$, pH 7.0) for fluorescence lifetime assays. Rabbit skeletal muscle actin was prepared as described (309) except ATP was omitted. F-actin was stabilized with equimolar phalloidin (Sigma-Aldrich).

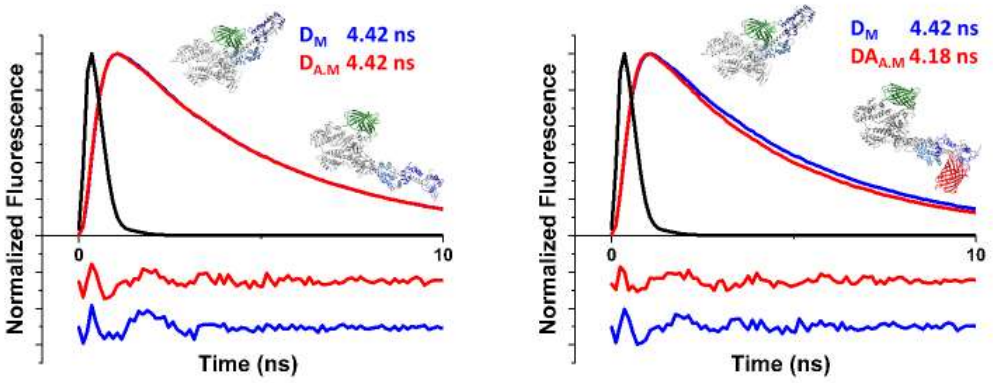


**Fig. 34. Time-domain Fluorescence of a *Dictyostelium* Myosin FRET Sensor.**

(Left) NowGFP-DdMhcA donor fluorescence is not affected by the presence ($D_{A.M}$) or absence ($D_M$) of 40 μM F-actin; (Right) Donor fluorescence ($DA_{A.M}$) is decreased in the presence of RLC-RFP-Δ93 acceptor. Intensity-weighted average lifetime was calculated from the 2-exponential decay model. Residual error (data minus fit) is plotted with 10-fold magnification below. IRF is plotted as the black curve.

Fluorescence lifetime was measured as described (292) using TCSPC detection maintaining at least 100,000 peak channel photon counts. The donor-only myosin (i.e., myosin co-purified with WT RLC) had a lifetime of 4.42 ns (Fig. 34). Mixing donor-only myosin with 40 μM F-actin did not alter the donor fluorescence. This concentration of actin was chosen to approximate the $K_m$ of ATPase activation. The concentration of myosin was not determined but was certainly less than 10 μM by comparison with purified fluorescent protein standards. Thus, actin was present in large excess to fully saturate myosin in rigor conditions.

Fluorescence lifetime of the donor+acceptor myosin was 4.18 ns in rigor (Fig. 34) corresponding to a FRET efficiency of 5% compared to the donor-only control. This change, though large compared to the experimental precision, was much less than predicted based on measurements in intact cells with at least 20% FRET efficiency. This discrepancy

could be due to bleaching of the acceptor during purification, nonspecific FRET in cells caused by excess unbound RLC, undesired intermolecular interactions with the acceptor, or dissociation of the RLC during purification. Bleaching is unlikely based on previous purification of GFP-MhcA with RFP-RLC (tagged at the N-terminus) that did not show a discrepancy between *in vivo* and *in vitro* FRET efficiency. Nonspecific FRET can be ruled out based on estimation of the minimum acceptor concentration required to affect the donor (310). Intermolecular interactions were ruled out by co-expression of the acceptor with soluble GFP or NowGFP donors, which did not significantly alter the *in vivo* donor lifetime. These results indicate that the RLC-RFP-Δ93 molecule dissociates from the light-chain binding domain during purification, perhaps because the fusion protein has a reduced binding affinity for myosin. Attempts to improve retention of the RLC by concentrating the sample 5-fold during purification or increasing intermolecular crowding with 2% w/v methylcellulose (311) did not alter the result.

Analysis of the fluorescence lifetime using a compartmental model (compartment 1 = donor-only; 2 = pre-powerstroke FRET distance; 3 = post-powerstroke FRET distance) found that the estimated donor-only fraction (apparently lacking the RLC acceptor) was 80%. The average lifetime of 4.18 ns can be interpreted as a mixture of 80% donor-only (4.42 ns) and 20% donor+acceptor molecules.

The *in vitro* fluorescence lifetime was analyzed in multiple biochemical conditions to validate the putative biosensor (Fig. 35). The excessively large donor-only fraction was controlled for using the compartmental model. Fluorescence amplitudes and lifetimes were

estimated from the donor-only fluorescence using a single exponential model. The Förster distance model (20) was then estimated, using two freely varying distance parameters. Mole fraction parameters were also freely varied for compartments 1 & 2.

Approximately 75% of nucleotide-free myosin (apo, M) populated the pre-powerstroke distance, shifting to 100% in M.ATP. Nucleotide-free myosin bound to 40 μM F-actin (A.M) strongly favored the rigor conformation with only 25% remaining at the lever-up distance. A.M.ATP had an intermediate value, consistent with a mixture of weakly bound or detached (M.ATP) and strongly bound (A.M) myosin. The results clearly resolve the rigor (A.M) state from the apo ($p$ = .0009), the detached ATP ($p$ = .0006), and relaxation conditions ($p$ = .001).

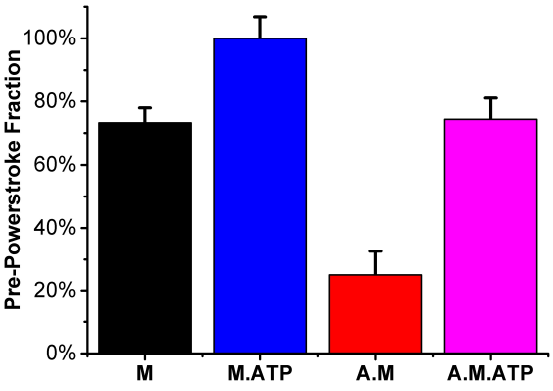


**Fig. 35. Motion of Myosin Light-Chain Binding Domain Reported by FRET.**
Conformation of the myosin FRET sensor was modeled as a distribution of two distances: pre-powerstroke and post-powerstroke. M, myosin (apo); M.ATP, myosin plus 1 mM MgATP; A.M; myosin plus 40 μM F-actin (rigor); A.M.ATP, relaxation. Note that because the true distances are not defined, the values of 0% and 100% are arbitrary. Standard error bars are estimated from the fit.

The pre-powerstroke fraction in the apo state was different from rigor and most closely resembled the relaxation condition. This unexpected result suggests that the myosin recovery stroke (reverse powerstroke) may be thermodynamically favorable even in the absence of ATP. This result contrasts with previous reports using a Cys-lite DdMhcA

sensor (260, 262). Future work will need to resolve this discrepancy perhaps with comparative measurements using varied labeling strategies to rule out effects of probe orientation (e.g., by circular permutation of the fluorescent protein structure). This result also demonstrates the importance of using a true rigor condition (A.M) to calibrate myosin biosensors rather than relying solely on detached states of myosin.

# 6 Conclusions and Future Directions

This work has focused on the cell biology of an unconventional myosin, DdMyo7, and biophysical methods for studying a conventional myosin, DdMhcA. The concerted application of molecular and cellular biophysics will be essential to discover how myosin motor proteins are activated for force generation within the cell and the specific mechanisms by which local tension generation and tension sensing by myosins impact their diverse physiological functions.

## 6.1 Amoebozoan Myosin 7: A Model Filopodial Myosin

Filopodia are commonly defined as dynamic cellular protrusions containing actin and the actin-bundling protein fascin. Fascin is required for filopodia formation in human cells. The recent identification of fascin in filopodia of *Salpingoeca rosetta*[1], a choanoflagellate, suggests that the role of fascin in filopodia predates the evolution of animals (196, 198). The conserved animal proteins Dia2 and VASP are associated with filopodia and localize to their tips but are not essential for their formation (183, 312, 313). Myosin 10 is essential for filopodia formation in humans, but is lost in some invertebrates such as *Drosophila melanogaster,* raising the possibility that the filopodial functions of Myosin 10 can be

[1] Identified as *Proterospongia* sp. in older literature but since reclassified.

replaced by other MyTH4-FERM myosins such as Myosin 15 (314).

**Table 10. Comparison of Filopodial Myosins**

| Feature | Metazoa (Myo10) | Amoebozoa (DdMyo7) |
|---|---|---|
| Fascin essential for filopodia | Yes (198) | Fascin is not present |
| VASP essential for filopodia | No (183, 312) | Yes (115) |
| Actin filament length | Long (≥ 500 nm) (315) | Short, 100-200 nm (187) |
| Effect of ΔFERM1 | Domain is not present in Myo10 | No strong effect; possibly shorter filopodia |
| Effect of ΔFERM2 | Increased extension velocity (219) | Decreased extension velocity |
| Effect of K/RxxK/R motif | Motif is not present in Myo10 | Negatively regulates filopod formation (208, 211) |
| Effect of PIP3 binding | Activation (210, 316, 317) | Not required for activation |
| Effect of talin binding | Myo10 lacks proline-rich regions involved in talin binding | Stabilizes talin in cytosol and promotes cell adhesion (161, 164) |
| Effect of Motor/Lever arm expression | Induces microspikes and/or filopodia (205, 318, 319) | Does not induce microspikes or filopodia |
| Effect of Tail expression | Headless variant weakly localizes to membrane (320) | Headless mutant strongly localizes to membrane/cortex |
| Motor/Lever arm/MyTH4 is essential for filopodia | Yes (112, 114, 212) | |

Conservation of actin-based filopodia, as well as key proteins essential for filopodia, suggests that the molecular mechanism(s) of filopodia formation have also been conserved as a core function in migratory cells including animals, choanoflagellates and amoebae. The Amoebozoa branched from the fungal/animal lineage (Opisthokonta) prior to the evolution of fascin and Myo10, yet amoebae produce abundant dynamic filopodia with MF myosin at their tips. There is no protein equivalent to fascin in amoebozoan filopodia as

the known actin-bundling proteins appear to function redundantly. DdMyo7 is essential for filopodia formation like Myo10, but in most other respects resembles the holozoan Myo7 or has unique features (Table 10). Chapter 2 shows that the DdMyo7 motor domain is unable to localize to filopodia without its lever arm (IQ motifs and SAH) and a conserved post-lever arm region (aa 1021-1115) (Fig. 36). The MyTH4-FERM domain is essential for localization to the actin cortex/membrane region and for full rescue of filopodia formation. A mutant protein containing only the first MyTH4 domain induced filopodia with low frequency, in contrast to the Myo10 ΔFERM mutant (retaining MyTH4) that can induce dorsal filopodia in HeLa cells at virtually the same frequency as full length Myo10 (112). In *myo7*$^{-}$ cells expressing DdMyo7 chimeras, the Myo10 MF domain partially rescued filopodia formation while the Myo10 MyTH4 domain did not, suggesting that in Amoebozoa the FERM domain plays a direct role in promoting filopodia initiation while in animals the MyTH4 domain is sufficient. This would be consistent with specialization of the Myo10 FERM domain for interaction with membrane proteins such as the netrin receptor and β-integrins (100, 192) and perhaps also a reduced role for actin-binding by the FERM domain in fascin-based filopodia. Future studies must determine the specific molecular function of the MyTH4 domain in Myo10 and DdMyo7, which may represent a core conserved mechanism of filopodia formation in animals and Amoebozoa. It will also be interesting to test whether these motors are capable of bundling or clustering actin filaments, either through their motor domains, actin-binding sites on the FERM domains, or both. Changes in local actin filament organization may be keys to understanding the function of filopodial MF myosins.

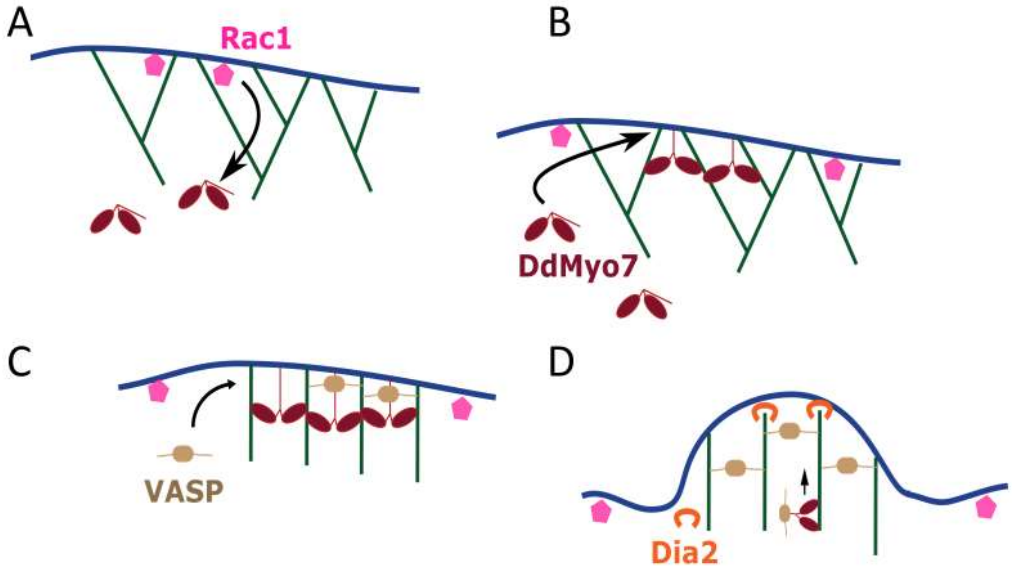


**Fig. 37. Proposed Model of Filopod Initiation in *Dictyostelium*.**

(A) Membrane-bound Rac1 activates DdMyo7 in the cytosol; (B) Activated DdMyo7 associates with the plasma membrane via its tail domain; (C) Membrane-bound DdMyo7 juxtaposes actin barbed ends and/or recruits VASP to barbed ends; (D) VASP increases the local density of free barbed ends through its anti-capping and bundling activities, possibly assisted by recruitment of formin Dia2. The filopodium begins to extend as growing actin filaments push against the plasma membrane.

Current models of filopodia initiation focus on the convergence of actin filament barbed ends, the 'convergent elongation' model (205, 321, 322). Motor activity of MF myosins is involved in filopodia initiation yet the mechanical role of the motor is unclear (323). The ability of MF domains to bind actin filaments suggests a model in which local tension generation by MF myosin pulls on actin filament 'cargo' bound to the FERM domain (Fig. 37). As the MF myosin moves toward the barbed end of its track, it would progressively recruit and orient cargo filaments in the direction of travel. DdMyo7 provides an excellent system to test this model since the interaction of DdMyo7 FERM domains with actin has been characterized (324) and DdMyo7 FERM domains appear to play a stronger role in initiating filopodia than does the Myo10 FERM. Initiation of fascin-based

filopodia might occur through multiple paths including FERM-independent and VASP-independent mechanisms, neither of which prevail in *Dictyostelium.* Thus, DdMyo7 is a natural model for an MF myosin-dependent mechanism of filopodia initiation.

## 6.2 Myosin Biosensors: Combining Structure and Dynamics

Looking forward, the primary consideration for Myosin 2 biosensors is the development of assays measuring the fraction of strongly-bound heads in relaxation, resolving the M.ATP and A.M.ATP states, since myosin will be ATP-saturated in most physiologically relevant contexts. This is currently feasible although sensitivity will be greatly improved by reducing the donor-only fraction and associated uncertainty in the model fit. Furthermore, the two-distance model is likely to be an oversimplification given evidence that the conformation and dynamics of myosin are altered in weakly-bound states compared to detached states (262, 325). It will be helpful to pursue *in vitro* experiments at saturating ATP over a range of actin concentrations, thereby varying the fraction of weakly-bound myosin, to further characterize the structure of these states.

Finally, while optimization of myosin biosensors for low-duty ratio conventional myosins such as DdMhcA is an immediate goal, it should be noted that high-duty ratio motors such as Myo7, Myo10, and potentially DdMyo7, have a distinct advantage in FRET biosensor design because the strongly-bound state is dominant in actively cycling motors.

# References


1. Doering C, Ermentrout B, Oster G (1995) Rotary DNA motors. *Biophys J* 69(6):2256–2267.

2. Stewart AG, Laming EM, Sobti M, Stock D (2014) Rotary ATPases — dynamic molecular machines. *Current Opinion in Structural Biology* 25:40–48.

3. Bardy SL, Ng SYM, Jarrell KF (2003) Prokaryotic motility structures. *Microbiology* 149(2):295–304.

4. Itoh T, et al. (2005) Dynamin and the actin cytoskeleton cooperatively regulate plasma membrane invagination by BAR and F-BAR proteins. *Dev Cell* 9(6):791–804.

5. Sweeney HL, Houdusse A (2010) Structural and functional insights into the myosin motor mechanism. *Annu Rev Biophys* 39(1):539–557.

6. Bloemink MJ, Geeves MA (2011) Shaking the myosin family tree: Biochemical kinetics defines four types of myosin motor. *Sem Cell Dev Biol* 22(9):961–967.

7. Carter AP, Diamant AG, Urnavicius L (2016) How dynein and dynactin transport cargos: a structural perspective. *Curr Opin Struct Biol* 37:62–70.

8. Roberts AJ, Kon T, Knight PJ, Sutoh K, Burgess SA (2013) Functions and mechanics of dynein motor proteins. *Nat Rev Mol Cell Biol* 14(11):713–726.

9. Lawrence CJ, et al. (2004) A standardized kinesin nomenclature. *J Cell Biol* 167(1):19–22.

10. Verhey KJ, Cochran JC, Walczak CE (2015) The Kinesin Superfamily. *Kinesins and Cancer*, ed Kozielski F (Springer Netherlands), pp 1–26.

11. Vale RD (1996) Switches, latches, and amplifiers: common themes of G proteins and molecular motors. *J Cell Biol* 135(2):291–302.

12. Leipe DD, Wolf YI, Koonin EV, Aravind L (2002) Classification and evolution of P-loop GTPases and related ATPases. *J Mol Biol* 317(1):41–72.

13. Welch CM (2011) Rho GTPase dynamics in the regulation of cellular signaling and

migration. Available at: https://cdr.lib.unc.edu/record/uuid:96f023f7-536f-4d2c-857d-b4f3ec1d2aba.

14. Wennerberg K, Rossman KL, Der CJ (2005) The Ras superfamily at a glance. *J Cell Sci* 118(5):843–846.

15. Burridge K, Wennerberg K (2004) Rho and Rac take center stage. *Cell* 116(2):167–179.

16. Verhey KJ, Kaul N, Soppina V (2011) Kinesin assembly and movement in cells. *Annu Rev Biophys* 40(1):267–288.

17. Cianfrocco MA, DeSantis ME, Leschziner AE, Reck-Peterson SL (2015) Mechanism and regulation of cytoplasmic dynein. *Annu Rev Cell Dev Biol* 31(1):83–108.

18. Vicente JJ, Wordeman L (2015) Mitosis, microtubule dynamics and the evolution of kinesins. *Exp Cell Res* 334(1):61–69.

19. Mountain V, Compton DA (2000) Dissecting the role of molecular motors in the mitotic spindle. *Anat Rec* 261(1):14–24.

20. Muretta JM, Petersen KJ, Thomas DD (2013) Direct real-time detection of the actin-activated power stroke within the myosin catalytic domain. *PNAS* 110(18):7211–7216.

21. Houdusse A, Sweeney HL (2016) How myosin generates force on actin filaments. *Trends Biochem Sci*. doi:10.1016/j.tibs.2016.09.006.

22. Kull FJ, Endow SA (2013) Force generation by kinesin and myosin cytoskeletal motor proteins. *J Cell Sci* 126(1):9–19.

23. Lorenz M, Holmes KC (2010) The actin-myosin interface. *PNAS* 107(28):12529–12534.

24. Goodson HV, Hawse WF (2002) Molecular evolution of the actin family. *J Cell Sci* 115(13):2619–2622.

25. Spang A, et al. (2015) Complex archaea that bridge the gap between prokaryotes and eukaryotes. *Nature* 521(7551):173–179.

26. Ettema TJG, Lindås A-C, Bernander R (2011) An actin-based cytoskeleton in archaea. *Molecular Microbiology* 80(4):1052–1061.

27. Richards TA, Cavalier-Smith T (2005) Myosin domain evolution and the primary divergence of eukaryotes. *Nature* 436(7054):1113–1118.

28. Foth BJ, Goedecke MC, Soldati D (2006) New insights into myosin evolution and classification. *PNAS* 103(10):3681–3686.

29. Odronitz F, Kollmar M (2007) Drawing the tree of eukaryotic life based on the analysis of 2,269 manually annotated myosins from 328 species. *Genome Biol* 8(9):1–23.

30. Bezanilla M, Horton AC, Sevener HC, Quatrano RS (2003) Phylogenetic analysis of new plant myosin sequences. *J Mol Evol* 57(2):229–239.

31. Peremyslov VV, et al. (2011) Expression, splicing, and evolution of the myosin gene family in plants. *Plant Physiol* 155(3):1191–1204.

32. Yokota E, Shimmen T (2011) Plant Myosins. *The Plant Cytoskeleton*, Advances in Plant Biology., ed Liu B (Springer New York), pp 33–56.

33. Aurrecoechea C, et al. (2009) GiardiaDB and TrichDB: integrated genomic resources for the eukaryotic protist pathogens *Giardia lamblia* and *Trichomonas vaginalis*. *Nucl Acids Res* 37(suppl 1):D526–D530.

34. Moon A, Drubin DG (1995) The ADF/cofilin proteins: Stimulus-responsive modulators of actin dynamics. *Mol Biol Cell* 6(11):1423–1431.

35. Paunola E, Mattila PK, Lappalainen P (2002) WH2 domain: a small, versatile adapter for actin monomers. *FEBS Letters* 513(1):92–97.

36. Su H, Wang T, Dong H, Ren H (2007) The villin/gelsolin/fragmin superfamily proteins in plants. *J Integr Plant Biol* 49(8):1183–1191.

37. Eckert C, Goretzki A, Faberova M, Kollmar M (2012) Conservation and divergence between cytoplasmic and muscle-specific actin capping proteins: insights from the crystal structure of cytoplasmic Cap32/34 from *Dictyostelium discoideum*. *BMC Structural Biology* 12:12.

38. Thompson ME, Heimsath EG, Gauvin TJ, Higgs HN, Kull FJ (2012) FMNL3 FH2-actin structure gives insight into formin-mediated actin nucleation and elongation. *NatStructMolBiol* 20:111–118.

39. Boczkowska M, Rebowski G, Kast DJ, Dominguez R (2014) Structural analysis of the transitional state of Arp2/3 complex activation by two actin-bound WCAs. *Nat*

*Commun* 5:3308.

40. Machesky LM, Insall RH (1998) Scar1 and the related Wiskott–Aldrich syndrome protein, WASP, regulate the actin cytoskeleton through the Arp2/3 complex. *Curr Biol* 8(25):1347–1356.

41. Szymanski DB (2005) Breaking the WAVE complex: the point of *Arabidopsis* trichomes. *Curr Opin Plant Biol* 8(1):103–112.

42. Veltman DM, King JS, Machesky LM, Insall RH (2012) SCAR knockouts in *Dictyostelium*: WASP assumes SCAR's position and upstream regulators in pseudopods. *J Cell Biol* 198(4):501–508.

43. Chen Z, et al. (2010) Structure and control of the actin regulatory WAVE complex. *Nature* 468(7323):533–538.

44. Buday L, Wunderlich L, Tamás P (2002) The Nck family of adapter proteins: Regulators of actin cytoskeleton. *Cell Signal* 14(9):723–731.

45. Padrick SB, et al. (2008) Hierarchical regulation of WASP/WAVE proteins. *Mol Cell* 32(3):426–438.

46. Tanaka-Takiguchi Y, et al. (2004) The elongation and contraction of actin bundles are induced by double-headed myosins in a motor concentration-dependent manner. *J Mol Biol* 341(2):467–476.

47. Desjardins PR, Burkman JM, Shrager JB, Allmond LA, Stedman HH (2002) Evolutionary implications of three novel members of the human sarcomeric myosin heavy chain gene family. *Mol Biol Evol* 19(4):375–393.

48. Rossi AC, Mammucari C, Argentini C, Reggiani C, Schiaffino S (2010) Two novel/ancient myosins in mammalian skeletal muscles: MYH14/7b and MYH15 are expressed in extraocular muscles and muscle spindles. *J Physiol* 588(Pt 2):353–364.

49. van Rooij E, et al. (2009) A family of microRNAs encoded by myosin genes governs myosin expression and muscle performance. *Dev Cell* 17(5):662–673.

50. Warkman AS, et al. (2012) Developmental expression and cardiac transcriptional regulation of Myh7b, a third myosin heavy chain in the vertebrate heart. *Cytoskeleton* 69(5):324–335.

51. Warkman AS, et al. (2012) Correction: Developmental expression and cardiac transcriptional regulation of Myh7b, a third myosin heavy chain in the vertebrate

heart. *Cytoskeleton* 69(12):1086–1086.

52. Steinmetz PRH, et al. (2012) Independent evolution of striated muscles in cnidarians and bilaterians. *Nature* 487(7406):231–234.

53. Brunet T, et al. (2016) The evolutionary origin of bilaterian smooth and striated myocytes. *bioRxiv*:064881.

54. Cheney RE, Riley MA, Mooseker MS (1993) Phylogenetic analysis of the myosin superfamily. *Cell Motil Cytoskeleton* 24(4):215–223.

55. OOta S, Saitou N (1999) Phylogenetic relationship of muscle tissues deduced from superimposition of gene trees. *Mol Biol Evol* 16(6):856–867.

56. Heissler SM, Sellers JR (2014) Myosin light chains: Teaching old dogs new tricks. *BioArchitecture* 4(6):169–188.

57. McIntosh BB, Ostap EM (2016) Myosin-I molecular motors at a glance. *J Cell Sci* 129(14):2689–2695.

58. Ebrahim S, et al. (2016) Stereocilia-staircase spacing is influenced by myosin III motors and their cargos espin-1 and espin-like. *Nat Commun* 7. doi:10.1038/ncomms10833.

59. Merritt RC, et al. (2012) Myosin IIIB uses an actin-binding motif in its espin-1 cargo to reach the tips of actin protrusions. *Curr Biol* 22(4):320–325.

60. Provance DW, et al. (2004) Chemical-genetic inhibition of a sensitized mutant myosin Vb demonstrates a role in peripheral-pericentriolar membrane traffic. *PNAS* 101(7):1868–1873.

61. Sladewski TE, Krementsova EB, Trybus KM (2016) Myosin Vc is specialized for transport on a secretory superhighway. *Curr Biol* 26(16):2202–2207.

62. Langford GM (2002) Myosin-V, a versatile motor for short-range vesicle transport. *Traffic* 3(12):859–865.

63. Mukherjea M, et al. (2014) Myosin VI must dimerize and deploy its unusual lever arm in order to perform its cellular roles. *Cell Rep* 8(5):1522–1532.

64. El-Amraoui A, Petit C (2005) Usher I syndrome: unravelling the mechanisms that underlie the cohesion of the growing hair bundle in inner ear sensory cells. *J Cell Sci* 118(20):4593–4603.

65. Crawley SW, Mooseker MS, Tyska MJ (2014) Shaping the intestinal brush border. *J Cell Biol* 207(4):441–451.

66. Sahly I, et al. (2012) Localization of Usher 1 proteins to the photoreceptor calyceal processes, which are absent from mice. *J Cell Biol* 199(2):381–399.

67. Omelchenko T, Hall A (2012) Myosin-IXa regulates collective epithelial cell migration by targeting RhoGAP activity to cell-cell junctions. *Curr Biol* 22(4):278–288.

68. Kong R, et al. (2015) Myo9b is a key player in SLIT/ROBO-mediated lung tumor suppression. *J Clin Invest* 125(12):4407–4420.

69. Courson DS, Cheney RE (2015) Myosin-X and disease. *Exp Cell Res* 334(1):10–15.

70. Li A, et al. (2010) The actin-bundling protein fascin stabilizes actin in invadopodia and potentiates protrusive invasion. *Curr Biol* 20(4):339–345.

71. McMichael BK, Cheney RE, Lee BS (2010) Myosin X regulates sealing zone patterning in osteoclasts through linkage of podosomes and microtubules. *J Biol Chem* 285(13):9506–9515.

72. Jacquemet G, Hamidi H, Ivaska J (2015) Filopodia in cell adhesion, 3D migration and cancer cell invasion. *Curr Opin Cell Biol* 36:23–31.

73. Manor U, et al. (2011) Regulation of stereocilia length by myosin XVa and whirlin depends on the actin-regulatory protein Eps8. *Curr Biol* 21(2):167–172.

74. Boger ET, Sellers JR, Friedman TB (2001) Human myosin XVBP is a transcribed pseudogene. *J Muscle Res Cell Motil* 22(5):477–483.

75. Yokoyama K, et al. (2011) NYAP: a phosphoprotein family that links PI3K to WAVE1 signalling in neurons. *EMBO J* 30(23):4739–4754.

76. Cameron RS, et al. (2007) Myosin16b: The COOH-tail region directs localization to the nucleus and overexpression delays S-phase progression. *Cell Motil Cytoskeleton* 64(1):19–48.

77. Billington N, et al. (2015) Myosin 18A coassembles with nonmuscle myosin 2 to form mixed bipolar filaments. *Curr Biol* 25(7):942–948.

78. Ajima R, et al. (2008) Deficiency of Myo18B in mice results in embryonic lethality with cardiac myofibrillar aberrations. *Genes to Cells* 13(10):987–999.

79. Ajima R, et al. (2007) HOMER2 binds MYO18B and enhances its activity to suppress anchorage independent growth. *Biochem Biophys Res Commun* 356(4):851–856.

80. Alazami AM, et al. (2015) A novel syndrome of Klippel-Feil anomaly, myopathy, and characteristic facies is linked to a null mutation in MYO18B. *J Med Genet* 52(6):400–404.

81. Malfatti E, et al. (2015) A premature stop codon in MYO18B is associated with severe nemaline myopathy with cardiomyopathy. *J Neuromuscul Dis* 2(3):219–227.

82. Shneyer BI, Ušaj M, Henn A (2016) Myo19 is an outer mitochondrial membrane motor and effector of starvation-induced filopodia. *J Cell Sci* 129(3):543–556.

83. Singh R, Schilde C, Schaap P (2016) A core phylogeny of Dictyostelia inferred from genomes representative of the eight major and minor taxonomic divisions of the group. *BMC Evolutionary Biology* 16:251.

84. Fey P, Kowal AS, Gaudet P, Pilcher KE, Chisholm RL (2007) Protocols for growth and development of *Dictyostelium discoideum*. *Nat Protoc* 2(6):1307–1316.

85. Adl SM, et al. (2012) The revised classification of eukaryotes. *J Eukaryot Microbiol* 59(5):429–514.

86. Erratum (2013) *J Eukaryot Microbiol* 60(3):321–321.

87. Kriebel PW, Barr VA, Rericha EC, Zhang G, Parent CA (2008) Collective cell migration requires vesicular trafficking for chemoattractant delivery at the trailing edge. *J Cell Biol* 183(5):949–961.

88. Kriebel PW (2009) Vesicle trafficking and protein synthesis, target adenylyl cyclase A to the back of migrating cells, localizing the release of chemoattractant to the trailing edge. Dissertation (THE GEORGE WASHINGTON UNIVERSITY). Available at: http://gradworks.umi.com/33/37/3337313.html [Accessed May 3, 2014].

89. Loomis WF (2014) Cell signaling during development of *Dictyostelium*. *Dev Biol* 391(1):1–16.

90. Sucgang R, Weijer CJ, Siegert F, Franke J, Kessin RH (1997) Null mutations of the *Dictyostelium* cyclic nucleotide phosphodiesterase gene block chemotactic cell movement in developing aggregates. *Dev Biol* 192(1):181–192.

91. Turing AM (1952) The chemical basis of morphogenesis. *Phil Trans R Soc Lond B* 237(641):37–72.

92. Cai H, Devreotes PN (2011) Moving in the right direction: How eukaryotic cells migrate along chemical gradients. *Seminars in Cell & Developmental Biology* 22:834–841.

93. Raper KB (1940) Pseudoplasmodium formation and organization in *Dictyostelium discoideum*. *J Elisha Mitchell Sci Soc* 56:241–282.

94. Bonner JT, Savage LJ (1947) Evidence for the formation of cell aggregates by chemotaxis in the development of the slime mold *Dictyostelium discoideum*. *J Exp Zool* 106(1):1–26.

95. Dickinson DJ, Nelson WJ, Weis WI (2011) A polarized epithelium organized by β- and α-catenin predates cadherin and Metazoan origins. *Science* 331(6022):1336–1339.

96. Horowitz JA, Hammer JA (1990) A new *Acanthamoeba* myosin heavy chain: Cloning of the gene and immunological identification of the polypeptide. *J Biol Chem* 265(33):20646–20652.

97. Breshears LM, Wessels D, Soll DR, Titus MA (2010) An unconventional myosin required for cell polarization and chemotaxis. *PNAS* 107(15):6918–6923.

98. Breshears LM (2009) An unconventional myosin is necessary for chemotaxis in *Dictyostellium discoideum*. Ph.D. (University of Minnesota, United States -- Minnesota). Available at: http://purl.umn.edu/54107 [Accessed November 19, 2012].

99. Geissler H, Ullmann R, Soldati T (2000) The tail domain of Myosin M catalyses nucleotide exchange on Rac1 GTPases and can induce actin-driven surface protrusions. *Traffic* 1(5):399–410.

100. Wei Z, Yan J, Lu Q, Pan L, Zhang M (2011) Cargo recognition mechanism of myosin X revealed by the structure of its tail MyTH4-FERM tandem in complex with the DCC P3 domain. *PNAS* 108(9):3572–3577.

101. Gotesman M, Hosein RE, Gavin RH (2011) MyTH4, independent of its companion FERM domain, affects the organization of an intramacronuclear microtubule array and is involved in elongation of the macronucleus in *Tetrahymena thermophila*. *Cytoskeleton* 68(4):220–236.

102. Planelles-Herrero VJ, et al. (2016) Myosin MyTH4-FERM structures highlight important principles of convergent evolution. *PNAS* 113(21):E2906–E2915.

103. Chishti AH, et al. (1998) The FERM domain: a unique module involved in the linkage of cytoplasmic proteins to the membrane. *Trends in Biochemical Sciences* 23(8):281–282.

104. Lee H-S, et al. (2004) Characterization of an actin-binding site within the talin FERM domain. *Journal of Molecular Biology* 343(3):771–784.

105. Buschmann H, et al. (2015) *Arabidopsis* KCBP interacts with AIR9 but stays in the cortical division zone throughout mitosis via its MyTH4-FERM domain. *J Cell Sci* 128(11):2033–2046.

106. Huang X, Cheng H-J, Tessier-Lavigne M, Jin Y (2002) MAX-1, a novel PH/MyTH4/FERM domain cytoplasmic protein implicated in netrin-mediated axon repulsion. *Neuron* 34(4):563–576.

107. Weck ML, Crawley SW, Stone CR, Tyska MJ (2016) Myosin-7b promotes distal tip localization of the intermicrovillar adhesion complex. *Current Biology*. doi:10.1016/j.cub.2016.08.014.

108. Bahloul A, et al. (2010) Cadherin-23, myosin VIIa and harmonin, encoded by Usher syndrome type I genes, form a ternary complex and interact with membrane phospholipids. *Hum Mol Genet* 19(18):3557–3565.

109. Pi X, et al. (2007) Sequential roles for myosin-X in BMP6-dependent filopodial extension, migration, and activation of BMP receptors. *J Cell Biol* 179(7):1569–1582.

110. Zhu X-J, et al. (2007) Myosin X regulates netrin receptors and functions in axonal path-finding. *Nat Cell Biol* 9(2):184–192.

111. Almagro S, et al. (2010) The motor protein Myosin-X transports VE-cadherin along filopodia to allow the formation of early endothelial cell-cell contacts. *Mol Cell Biol* 30(7):1703–1717.

112. Bohil AB, Robertson BW, Cheney RE (2006) Myosin-X is a molecular motor that functions in filopodia formation. *Proceedings of the National Academy of Sciences* 103(33):12411–12416.

113. Bohil AB (2006) Myosin-X is a molecular motor central to filopodia formation, adhesion, and signaling. Ph.D. (The University of North Carolina at Chapel Hill,

United States -- North Carolina). Available at: https://cdr.lib.unc.edu/record/uuid:714f60ea-06c0-4ac8-a435-19bdf144c1dd [Accessed February 15, 2016].

114. Tuxworth RI, et al. (2001) A role for myosin VII in dynamic cell adhesion. *Current Biology* 11(5):318–329.

115. Han Y-H, et al. (2002) Requirement of a vasodilator-stimulated phosphoprotein family member for cell adhesion, the formation of filopodia, and chemotaxis in *Dictyostelium*. *J Biol Chem* 277(51):49877–49887.

116. Petersen KJ, et al. (2016) MyTH4-FERM myosins have an ancient and conserved role in filopod formation. *PNAS*:201615392.

117. Heid PJ, Geiger J, Wessels D, Voss E, Soll DR (2005) Computer-assisted analysis of filopod formation and the role of myosin II heavy chain phosphorylation in *Dictyostelium*. *J Cell Sci* 118(10):2225–2237.

118. Sabry JH, Moores SL, Ryan S, Zang J-H, Spudich JA (1997) Myosin heavy chain phosphorylation sites regulate myosin localization during cytokinesis in live cells. *Mol Biol Cell* 8(12):2605–2615.

119. Bosgraaf L, van Haastert PJM (2006) The regulation of myosin II in *Dictyostelium*. *European Journal of Cell Biology* 85(9–10):969–979.

120. Jung G, Remmert K, Wu X, Volosky JM, Hammer JA (2001) The *Dictyostelium* CARMIL protein links capping protein and the Arp2/3 complex to type I myosins through their SH3 domains. *The Journal of Cell Biology* 153(7):1479–1498.

121. Brzeska H, Guag J, Preston GM, Titus MA, Korn ED (2012) Molecular basis of dynamic relocalization of *Dictyostelium* Myosin IB. *J Biol Chem* 287(18):14923–14936.

122. Brzeska H, Pridham K, Chery G, Titus MA, Korn ED (2014) The association of Myosin IB with actin waves in *Dictyostelium* requires both the plasma membrane-binding site and actin-binding region in the myosin tail. *PLoS ONE* 9(4):e94306.

123. Morita Y, Jung G, Hammer, JA III, Fukui, Y (1996) Localization of *Dictyostelium* MyoB and MyoD to filopodia and cell-cell contact sites using isoform-specific antibodies. *Eur J Cell Biol* 71(4):371–379.

124. Novak KD, Titus MA (1997) Myosin I overexpression impairs cell migration. *J Cell Biol* 136(3):633–647.

125. Wessels D, Murray J, Jung G, Hammer JA, Soll DR (1991) Myosin IB null mutants of *Dictyostelium* exhibit abnormalities in motility. *Cell Motil Cytoskeleton* 20(4):301–315.

126. Dai J, Ping Ting-Beall H, Hochmuth RM, Sheetz MP, Titus MA (1999) Myosin I contributes to the generation of resting cortical tension. *Biophysical Journal* 77(2):1168–1176.

127. Neuhaus EM, Soldati T (2000) A myosin I is involved in membrane recycling from early endosomes. *The Journal of Cell Biology* 150(5):1013–1026.

128. Brzeska H, Koech H, Pridham KJ, Korn ED, Titus MA (2016) Selective localization of Myosin-I proteins in macropinosomes and actin waves. *Cytoskeleton* 73(2):68–82.

129. Jung G, Wu X, Hammer JA (1996) *Dictyostelium* mutants lacking multiple classic myosin I isoforms reveal combinations of shared and distinct functions. *J Cell Biol* 133(2):305–323.

130. Chen C-L, Wang Y, Sesaki H, Iijima M (2012) Myosin I links PIP3 signaling to remodeling of the actin cytoskeleton in chemotaxis. *Sci Signal* 5(209):ra10.

131. Schirenbeck A, Bretschneider T, Arasada R, Schleicher M, Faix J (2005) The Diaphanous-related formin dDia2 is required for the formation and maintenance of filopodia. *Nat Cell Biol* 7(6):619–625.

132. Breitsprecher D, et al. (2008) Clustering of VASP actively drives processive, WH2 domain-mediated actin filament elongation. *EMBO J* 27(22):2943–2954.

133. Lin W-H, Nelson SE, Hollingsworth RJ, Chung CY (2010) Functional roles of VASP phosphorylation in the regulation of chemotaxis and osmotic stress response. *Cytoskeleton* 67(4):259–271.

134. Schirenbeck A, et al. (2006) The bundling activity of vasodilator-stimulated phosphoprotein is required for filopodium formation. *PNAS* 103(20):7694–7699.

135. Seastone DJ, et al. (2001) The WASp-like protein Scar regulates macropinocytosis, phagocytosis and endosomal membrane flow in *Dictyostelium*. *Journal of Cell Science* 114(14):2673–2683.

136. Steffen A, et al. (2006) Filopodia formation in the absence of functional Wave- and Arp2/3-complexes. *Mol Biol Cell* 17(6):2581–2591.

137. Breitsprecher D, et al. (2011) Molecular mechanism of Ena/VASP-mediated actin-filament elongation. *EMBO J* 30(3):456–467.

138. Myers SA, Leeper LR, Chung CY (2006) WASP-interacting protein is important for actin filament elongation and prompt pseudopod formation in response to a dynamic chemoattractant gradient. *Mol Biol Cell* 17(10):4564–4575.

139. Myers SA, Han JW, Lee Y, Firtel RA, Chung CY (2005) A *Dictyostelium* homologue of WASP is required for polarized F-actin assembly during chemotaxis. *Mol Biol Cell* 16(5):2191–2206.

140. Pfannes EKB, Theves M, Wegner C, Beta C (2012) Impact of the carbazole derivative wiskostatin on mechanical stability and dynamics of motile cells. *J Muscle Res Cell Motil* 33(2):95–106.

141. Pfannes EKB (2012) Probing the regulatory mechanisms of the actomyosin system in motile cells. Dissertation (Universität Potsdam). Available at: https://publishup.uni-potsdam.de/opus4-ubp/frontdoor/index/index/docId/5597 [Accessed November 28, 2016].

142. Dumontier M, Hocht P, Mintert U, Faix J (2000) Rac1 GTPases control filopodia formation, cell motility, endocytosis, cytokinesis and development in *Dictyostelium*. *J Cell Sci* 113(12):2253–2265.

143. Filić V, Marinović M, Faix J, Weber I (2012) A dual role for Rac1 GTPases in the regulation of cell motility. *J Cell Sci* 125(2):387–398.

144. Mondal S, et al. (2010) Regulation of the actin cytoskeleton by an interaction of IQGAP related protein GAPA with filamin and cortexillin I. *PLOS ONE* 5(11):e15440.

145. Han JW, Leeper L, Rivero F, Chung CY (2006) Role of RacC for the regulation of WASP and phosphatidylinositol 3-kinase during chemotaxis of *Dictyostelium*. *J Biol Chem* 281(46):35224–35234.

146. Somesh BP, et al. (2006) RacG regulates morphology, phagocytosis, and chemotaxis. *Eukaryotic Cell* 5(10):1648–1663.

147. Somesh BP, Neffgen C, Iijima M, Devreotes P, Rivero F (2006) *Dictyostelium* RacH regulates endocytic vesicular trafficking and is required for localization of vacuolin. *Traffic* 7(9):1194–1212.

148. Pakes NK, et al. (2012) The Rac GEF ZizB regulates development, cell motility and

cytokinesis in *Dictyostelium*. *J Cell Sci* 125(10):2457–2465.

149. Heath RJW, Insall RH (2008) *Dictyostelium* MEGAPs: F-BAR domain proteins that regulate motility and membrane tubulation in contractile vacuoles. *Journal of Cell Science* 121(7):1054–1064.

150. Chen C-F, Katz ER (2000) Mediation of cell-substratum adhesion by RasG in *Dictyostelium*. *J Cell Biochem* 79(1):139–149.

151. Tuxworth RI, et al. (1997) *Dictyostelium* RasG is required for normal motility and cytokinesis, but not growth. *J Cell Biol* 138(3):605–614.

152. Faix J, et al. (1998) The IQGAP-related protein DGAP1 interacts with Rac and is involved in the modulation of the F-actin cytoskeleton and control of cell motility. *Journal of Cell Science* 111(20):3059–3071.

153. Dias M, et al. (2013) *Dictyostelium* ACAP-A is an ArfGAP involved in cytokinesis, cell migration and actin cytoskeleton dynamics. *J Cell Sci* 126(3):756–766.

154. Chen P-W, Randazzo PA, Parent CA (2010) ACAP-A/B are ArfGAP homologs in *Dictyostelium* involved in sporulation but not in chemotaxis. *PLoS ONE* 5(1):e8624.

155. Garcia R, Nguyen L, Brazill D (2013) *Dictyostelium discoideum* SecG interprets cAMP-mediated chemotactic signals to influence actin organization. *Cytoskeleton*. doi:10.1002/cm.21107.

156. Jeon TJ, Lee D-J, Merlot S, Weeks G, Firtel RA (2007) Rap1 controls cell adhesion and cell motility through the regulation of myosin II. *J Cell Biol* 176(7):1021–1033.

157. Mun H, Jeon TJ (2012) Regulation of actin cytoskeleton by Rap1 binding to RacGEF1. *Mol Cells* 34(1):71–76.

158. Plak K, et al. (2013) GxcC connects Rap and Rac signaling during *Dictyostelium* development. *BMC Cell Biology* 14(1):6.

159. Plak K, Pots H, van Haastert PJM, Kortholt A (2016) Direct Interaction between TalinB and Rap1 is necessary for adhesion of *Dictyostelium* cells. *BMC Cell Biology* 17:1.

160. Mun H, Lee M-R, Jeon TJ (2014) RapGAP9 regulation of the morphogenesis and development in *Dictyostelium*. *Biochem Biophys Res Commun* 446(2):428–433.

161. Galdeen SA, Stephens S, Thomas DD, Titus MA (2007) Talin influences the

dynamics of the myosin VII-membrane interaction. *Mol Biol Cell* 18(10):4074–4084.

162. Kreitmeier M, Gerisch G, Heizer C, Müller-Taubenberger A (1995) A talin homologue of *Dictyostelium* rapidly assembles at the leading edge of cells in response to chemoattractant. *J Cell Biol* 129(1):179–188.

163. Niewöhner J, Weber I, Maniak M, Müller-Taubenberger A, Gerisch G (1997) Talin-null cells of *Dictyostelium* are strongly defective in adhesion to particle and substrate surfaces and slightly impaired in cytokinesis. *J Cell Biol* 138(2):349–361.

164. Tuxworth RI, Stephens S, Ryan ZC, Titus MA (2005) Identification of a myosin VII-talin complex. *J Biol Chem* 280(28):26557–26564.

165. Bukharova T, et al. (2005) Paxillin is required for cell-substrate adhesion, cell sorting and slug migration during *Dictyostelium* development. *J Cell Sci* 118(18):4295–4310.

166. Nagasaki A, Kanada M, Uyeda TQ (2009) Cell adhesion molecules regulate contractile ring-independent cytokinesis in Dictyostelium discoideum. *Cell Res* 19(2):236–246.

167. Pribic J, Garcia R, Kong M, Brazill D (2011) Paxillin and Phospholipase D interact to regulate actin-based processes in *Dictyostelium discoideum*. *Eukaryotic Cell* 10(7):977–984.

168. Patel H, et al. (2008) The multi-FERM-domain-containing protein FrmA is required for turnover of paxillin-adhesion sites during cell migration of *Dictyostelium*. *Journal of Cell Science* 121(8):1159–1164.

169. Fechheimer M (1987) The *Dictyostelium discoideum* 30,000-dalton protein is an actin filament-bundling protein that is selectively present in filopodia. *J Cell Biol* 104(6):1539–1551.

170. Fechheimer M, Ingalls HM, Furukawa R, Luna EJ (1994) Association of the *Dictyostelium* 30 kDa actin bundling protein with contact regions. *J Cell Sci* 107(9):2393–2401.

171. Kim M-K, Kim J-H, Kim J-S, Kang S-O (2015) Structure of the 34 kDa F-actin-bundling protein ABP34 from *Dictyostelium discoideum*. *Acta Crystallographica Section D Biological Crystallography* 71(9):1835–1849.

172. Pikzack C, Prassler J, Furukawa R, Fechheimer M, Rivero F (2005) Role of calcium-

dependent actin-bundling proteins: Characterization of *Dictyostelium* mutants lacking fimbrin and the 34-kilodalton protein. *Cell Motil Cytoskeleton* 62(4):210–231.

173. Rivero F, Furukawa R, Noegel AA, Fechheimer M (1996) *Dictyostelium discoideum* cells lacking the 34,000-dalton actin-binding protein can grow, locomote, and develop, but exhibit defects in regulation of cell structure and movement: a case of partial redundancy. *J Cell Biol* 135(4):965–980.

174. Demma M, Warren V, Hock R, Dharmawardhane S, Condeelis J (1990) Isolation of an abundant 50,000-dalton actin filament bundling protein from *Dictyostelium* amoebae. *J Biol Chem* 265(4):2286–2291.

175. Dharmawardhane S, Demma M, Yang F, Condeelis J (1991) Compartmentalization and actin binding properties of ABP-50: The elongation factor-1 alpha of *Dictyostelium*. *Cell Motility and the Cytoskeleton* 20(4):279–288.

176. Yang F, Demma M, Warren V, Dharmawardhane S, Condeelis J (1990) Identification of an actin-binding protein from *Dictyostelium* as elongation factor 1a. *Nature* 347(6292):494–496.

177. Machesky LM, Atkinson SJ, Ampe C, Vandekerckhove J, Pollard TD (1994) Purification of a cortical complex containing two unconventional actins from *Acanthamoeba* by affinity chromatography on profilin-agarose. *J Cell Biol* 127(1):107–115.

178. Vandekerckhove J, et al. (1990) The covalent structure of *Acanthamoeba* actobindin. *J Biol Chem* 265(22):12801–12805.

179. Hug C, et al. (1995) Capping protein levels influence actin assembly and cell motility in *Dictyostelium*. *Cell* 81(4):591–600.

180. Garcia M, Ray S, Brown I, Irom J, Brazill D (2014) PakD, a putative p21-activated protein kinase in *Dictyostelium discoideum*, regulates actin. *Eukaryotic Cell* 13(1):119–126.

181. Gebbie L, et al. (2004) Phg2, a kinase involved in adhesion and focal site modeling in *Dictyostelium*. *Mol Biol Cell* 15(8):3915–3925.

182. Kortholt A, et al. (2006) Characterization of the GbpD-activated Rap1 pathway regulating adhesion and cell polarity in *Dictyostelium discoideum*. *J Biol Chem* 281(33):23367–23376.

183. Mattila PK, Lappalainen P (2008) Filopodia: Molecular architecture and cellular functions. *Nat Rev Mol Cell Biol* 9(6):446–454.

184. Ostap EM, et al. (2003) Dynamic localization of Myosin-I to endocytic structures in *Acanthamoeba*. *Cell Motil Cytoskeleton* 54(1):29–40.

185. Eilken HM, Adams RH (2010) Dynamics of endothelial cell behavior in sprouting angiogenesis. *Current Opinion in Cell Biology* 22(5):617–625.

186. Mortimer D, Fothergill T, Pujic Z, Richards LJ, Goodhill GJ (2008) Growth cone chemotaxis. *Trends in Neurosciences* 31(2):90–98.

187. Medalia O, et al. (2007) Organization of actin networks in intact filopodia. *Current Biology* 17(1):79–84.

188. Mellor H (2010) The role of formins in filopodia formation. *Biochimica et Biophysica Acta (BBA) - Molecular Cell Research* 1803(2):191–200.

189. Gerdes H-H, Rustom A, Wang X (2013) Tunneling nanotubes, an emerging intercellular communication route in development. *Mechanisms of Development* 130(6–8):381–387.

190. Kornberg TB, Roy S (2014) Cytonemes as specialized signaling filopodia. *Development* 141(4):729–736.

191. Ziv NE, Smith SJ (1996) Evidence for a role of dendritic filopodia in synaptogenesis and spine formation. *Neuron* 17(1):91–102.

192. Zhang H, et al. (2004) Myosin-X provides a motor-based link between integrins and the cytoskeleton. *Nat Cell Biol* 6(6):523–531.

193. Arjonen A, et al. (2014) Mutant p53–associated Myosin-X upregulation promotes breast cancer invasion and metastasis. *J Clin Invest* 124(3):1069–1082.

194. Cao R, et al. (2014) Elevated expression of myosin X in tumours contributes to breast cancer aggressiveness and metastasis. *Br J Cancer* 111(3):539–550.

195. Shibue T, Brooks MW, Inan MF, Reinhardt F, Weinberg RA (2012) The outgrowth of micrometastases is enabled by the formation of filopodium-like protrusions. *Cancer Discovery* 2(8):706–721.

196. Sebé-Pedrós A, et al. (2013) Insights into the origin of Metazoan filopodia and microvilli. *Mol Biol Evol* 30(9):2013–2023.

197. Cavalier-Smith T, et al. (2014) Multigene eukaryote phylogeny reveals the likely protozoan ancestors of opisthokonts (animals, fungi, choanozoans) and Amoebozoa. *Molecular Phylogenetics and Evolution* 81:71–85.

198. Vignjevic D, et al. (2006) Role of fascin in filopodial protrusion. *J Cell Biol* 174(6):863–875.

199. Furukawa R, Fechheimer M (1997) The structure, function, and assembly of actin filament bundles. *International Review of Cytology* 175:29–90.

200. Knight PJ, et al. (2005) The predicted coiled-coil domain of myosin 10 forms a novel elongated domain that lengthens the head. *J Biol Chem* 280(41):34702–34708.

201. Kerber ML, Cheney RE (2011) Myosin-X: A MyTH-FERM myosin at the tips of filopodia. *J Cell Sci* 124(22):3733–3741.

202. Sebé-Pedrós A, Grau-Bové X, Richards TA, Ruiz-Trillo I (2014) Evolution and classification of myosins, a paneukaryotic whole genome approach. *Genome Biol Evol*:evu013.

203. Heidel AJ, et al. (2011) Phylogeny-wide analysis of social amoeba genomes highlights ancient origins for complex intercellular communication. *Genome Res* 21(11):1882–1891.

204. Liu K, et al. (2012) SATé-II: Very fast and accurate simultaneous estimation of multiple sequence alignments and phylogenetic trees. *Syst Biol* 61(1):90–106.

205. Tokuo H, Mabuchi K, Ikebe M (2007) The motor activity of Myosin-X promotes actin fiber convergence at the cell periphery to initiate filopodia formation. *J Cell Biol* 179(2):229–238.

206. Wu L, Pan L, Wei Z, Zhang M (2011) Structure of MyTH4-FERM domains in myosin VIIa tail bound to cargo. *Science* 331(6018):757–760.

207. Weber I, Wallraff E, Albrecht R, Gerisch G (1995) Motility and substratum adhesion of *Dictyostelium* wild-type and cytoskeletal mutant cells: a study by RICM/bright-field double-view image analysis. *J Cell Sci* 108(4):1519–1530.

208. Sakai T, et al. (2015) Structure and regulation of the movement of human myosin VIIA. *Journal of Biological Chemistry* 290(28):17587–17598.

209. Umeki N, et al. (2009) The tail binds to the head–neck domain, inhibiting ATPase activity of myosin VIIA. *PNAS* 106(21):8483–8488.

210. Umeki N, et al. (2011) Phospholipid-dependent regulation of the motor activity of myosin X. *Nat Struct Mol Biol* 18(7):783–788.

211. Yang Y, et al. (2009) A FERM domain autoregulates *Drosophila* myosin 7a activity. *PNAS* 106(11):4189–4194.

212. Berg JS, Cheney RE (2002) Myosin-X is an unconventional myosin that undergoes intrafilopodial motility. *Nat Cell Biol* 4(3):246–250.

213. Lu Q, Ye F, Wei Z, Wen Z, Zhang M (2012) Antiparallel coiled-coil–mediated dimerization of myosin X. *PNAS* 109(43):17388–17393.

214. Crawley SW, et al. (2014) Intestinal brush border assembly driven by protocadherin-based intermicrovillar adhesion. *Cell* 157(2):433–446.

215. Belyantseva IA, et al. (2005) Myosin-XVa is required for tip localization of whirlin and differential elongation of hair-cell stereocilia. *Nature cell biology* 7(2):148–156.

216. Probst FJ, et al. (1998) Correction of deafness in *shaker-2* mice by an unconventional myosin in a BAC transgene. *Science* 280(5368):1444–1447.

217. Force A, et al. (1999) Preservation of duplicate genes by complementary, degenerative mutations. *Genetics* 151(4):1531–1545.

218. Prince VE, Pickett FB (2002) Splitting pairs: the diverging fates of duplicated genes. *Nat Rev Genet* 3(11):827–837.

219. Watanabe TM, Tokuo H, Gonda K, Higuchi H, Ikebe M (2010) Myosin-X induces filopodia by multiple elongation mechanism. *J Biol Chem* 285(25):19605–19614.

220. Sakai T, Umeki N, Ikebe R, Ikebe M (2011) Cargo binding activates myosin VIIA motor function in cells. *PNAS* 108(17):7028–7033.

221. Levi S, Polyakov M, Egelhoff TT (2000) Green fluorescent protein and epitope tag fusion vectors for *Dictyostelium discoideum*. *Plasmid* 44(3):231–238.

222. Knetsch MLW, Tsiavaliaris G, Zimmermann S, Rühl U, Manstein DJ (2002) Expression vectors for studying cytoskeletal proteins in *Dictyostelium discoideum*. *J Muscle Res Cell Motil* 23(7–8):605–611.

223. Odronitz F, Kollmar M (2006) Pfarao: a web application for protein family analysis customized for cytoskeletal and motor proteins (CyMoBase). *BMC Genomics* 7(1):300.

224. Nordberg H, et al. (2014) The genome portal of the Department of Energy Joint Genome Institute: 2014 updates. *Nucleic Acids Res* 42(Database issue):D26–D31.

225. Schaap P, et al. (2016) The *Physarum polycephalum* genome reveals extensive use of prokaryotic two-component and Metazoan-type tyrosine kinase signaling. *Genome Biol Evol* 8(1):109–125.

226. Edgar RC (2004) MUSCLE: Multiple sequence alignment with high accuracy and high throughput. *Nucl Acids Res* 32(5):1792–1797.

227. Faix J, Breitsprecher D, Stradal TEB, Rottner K (2009) Filopodia: Complex models for simple rods. *The International Journal of Biochemistry & Cell Biology* 41(8–9):1656–1664.

228. Schindelin J, et al. (2012) Fiji: An open-source platform for biological-image analysis. *Nat Meth* 9(7):676–682.

229. Sezgin M, Sankur B (2004) Survey over image thresholding techniques and quantitative performance evaluation. *J Electron Imaging* 13(1):146–168.

230. Joanes DN, Gill CA (1998) Comparing measures of sample skewness and kurtosis. *Journal of the Royal Statistical Society: Series D (The Statistician)* 47(1):183–189.

231. Price MN, Dehal PS, Arkin AP (2010) FastTree 2 – approximately maximum-likelihood trees for large alignments. *PLoS ONE* 5(3):e9490.

232. Haskell RC, Carlson FD, Blank PS (1989) Form birefringence of muscle. *Biophysical Journal* 56(2):401–413.

233. Huxley HE, Hanson J (1957) Quantitative studies on the structure of cross-striated myofibrils. *Biochimica et Biophysica Acta* 23:229–249.

234. von Muralt AL, Edsall JT (1930) Studies in the physical chemistry of muscle globulin III. The anisotropy of myosin and the angle of isocline. *Journal of Biological Chemistry* 89(1):315–350.

235. Engelhardt WA, Ljubimowa MN (1939) Myosine and adenosinetriphosphatase. *Nature* 144:668–669.

236. Albert Szent-Györgyi (1951) *Chemistry of muscular contraction* (Academic Press, New York). 2d ed., and enl..

237. Dainty M, et al. (1944) Studies on the anomalous viscosity and flow-birefringence

of protein solutions III. Changes in these properties of myosin solutions in relation to adenosinetriphosphate and muscular contraction. *J Gen Physiol* 27(4):355–399.

238. Huxley HE (1957) The double array of filaments in cross-striated muscle. *J Biophys Biochem Cytol* 3(5):631–648.

239. Huxley HE, Brown W (1967) The low-angle X-ray diagram of vertebrate striated muscle and its behaviour during contraction and rigor. *Journal of molecular biology* 30(2):383–IN16.

240. Rayment I, et al. (1993) Three-dimensional structure of myosin subfragment-1: A molecular motor. *Science* 261(5117):50–58.

241. Rayment I, et al. (1993) Structure of the actin-myosin complex and its implications for muscle contraction. *Science* 261(5117):58–65.

242. Dominguez R, Freyzon Y, Trybus KM, Cohen C (1998) Crystal structure of a vertebrate smooth muscle myosin motor domain and its complex with the essential light chain: visualization of the pre-power stroke state. *Cell* 94(5):559–571.

243. Houdusse A, Kalabokis VN, Himmel D, Szent-Györgyi AG, Cohen C (1999) Atomic structure of scallop myosin subfragment S1 complexed with MgADP. *Cell* 97(4):459–470.

244. Houdusse A, Szent-Györgyi AG, Cohen C (2000) Three conformational states of scallop myosin S1. *PNAS* 97(21):11238–11243.

245. Lorenz M, Popp D, Holmes KC (1993) Refinement of the F-actin model against X-ray fiber diffraction data by the use of a directed mutation algorithm. *Journal of Molecular Biology* 234(3):826–836.

246. Holmes KC, Angert I, Kull FJ, Jahn W, Schroeder RR (2003) Electron cryo-microscopy shows how strong binding of myosin to actin releases nucleotide. *Nature* 425(6956):423–427.

247. Behrmann E, et al. (2012) Structure of the rigor actin-tropomyosin-myosin complex. *Cell* 150(2):327–338.

248. von der Ecken J, Heissler SM, Pathan-Chhatbar S, Manstein DJ, Raunser S (2016) Cryo-EM structure of a human cytoplasmic actomyosin complex at near-atomic resolution. *Nature* 534(7609):724–728.

249. Kim LY, Gurel PS, Omabegho T, Bryant Z, Alushin GM (2016) High-resolution

structural insight into the myosin VI-F-actin interface. *Biophysical Journal* 110(3):22a.

250. Wulf SF, et al. (2016) Force-producing ADP state of myosin bound to actin. *PNAS*:201516598.

251. Toseland CP, Fili N eds. (2014) *Fluorescent methods for molecular motors* (Springer, Basel).

252. Lakowicz JR (2006) *Principles of fluorescence spectroscopy* (Springer, New York). 3rd ed.

253. Suzuki Y, Yasunaga T, Ohkura R, Wakabayashi T, Sutoh K (1998) Swing of the lever arm of a myosin motor at the isomerization and phosphate-release steps. *Nature* 396(6709):380–383.

254. Zeng W, et al. (2006) Resonance energy transfer between green fluorescent protein variants: Complexities revealed with myosin fusion proteins. *Biochemistry* 45(35):10482–10491.

255. Dale RE, Eisinger J (1974) Intramolecular distances determined by energy transfer. Dependence on orientational freedom of donor and acceptor. *Biopolymers* 13(8):1573–1605.

256. Dale RE, Eisinger J, Blumberg WE (1979) The orientational freedom of molecular probes. The orientation factor in intramolecular energy transfer. *Biophysical Journal* 26(2):161–193.

257. Dale RE, Eisinger J, Blumberg WE (1980) Correction. *Biophysical Journal* 30(2):365.

258. Vogel SS, van der Meer BW, Blank PS (2014) Estimating the distance separating fluorescent protein FRET pairs. *Methods* 66(2):131–138.

259. Scott BL, Hoppe AD (2015) Optimizing fluorescent protein trios for 3-Way FRET imaging of protein interactions in living cells. *Sci Rep* 5. doi:10.1038/srep10270.

260. Shih WM, Gryczynski Z, Lakowicz JR, Spudich JA (2000) A FRET-based sensor reveals large ATP hydrolysis–induced conformational changes and three distinct states of the molecular motor myosin. *Cell* 102(5):683–694.

261. Shih WM, Spudich JA (2001) The myosin relay helix to converter interface remains intact throughout the actomyosin ATPase cycle. *J Biol Chem* 276(22):19491–19494.

262. Kast DJE (2010) Phosphorylation-induced structural changes in smooth muscle myosin. Ph.D. (University of Minnesota, United States -- Minnesota). Available at: http://purl.umn.edu/94937 [Accessed March 4, 2013].

263. Agafonov RV, Nesmelov YE, Titus MA, Thomas DD (2008) Muscle and nonmuscle myosins probed by a spin label at equivalent sites in the force-generating domain. *Proc Natl Acad Sci USA* 105(36):13397–13402.

264. Agafonov RV, et al. (2009) Structural dynamics of the myosin relay helix by time-resolved EPR and FRET. *PNAS* 106(51):21625–21630.

265. Muretta JM, Rohde JA, Johnsrud DO, Cornea S, Thomas DD (2015) Direct real-time detection of the structural and biochemical events in the myosin power stroke. *PNAS* 112(46):14272–14277.

266. Iwai S, Uyeda TQP (2008) Visualizing myosin–actin interaction with a genetically-encoded fluorescent strain sensor. *PNAS* 105(44):16882–16887.

267. Iwai S, Uyeda TQP (2010) Myosin-actin interaction in *Dictyostelium* cells revealed by GFP-based strain sensor and validated linear spectral unmixing. *Cytometry Part A* 77A(8):743–750.

268. De La Cruz EM, Michael Ostap E (2009) Kinetic and equilibrium analysis of the myosin ATPase. *Methods in Enzymology*, Biothermodynamics, Part A., eds Johnson ML, Holt JM, Ackers GK (Academic Press), pp 157–192.

269. Uyeda TQP, Kron SJ, Spudich JA (1990) Myosin step size: Estimation from slow sliding movement of actin over low densities of heavy meromyosin. *Journal of Molecular Biology* 214(3):699–710.

270. Homma K, Ikebe M (2005) Myosin X is a high duty ratio motor. *J Biol Chem* 280(32):29381–29391.

271. Henn A, De La Cruz EM (2005) Vertebrate myosin VIIb is a high duty ratio motor adapted for generating and maintaining tension. *J Biol Chem* 280(47):39665–39676.

272. Spudich JA, et al. (2016) Effects of hypertrophic and dilated cardiomyopathy mutations on power output by human β-cardiac myosin. *Journal of Experimental Biology* 219(2):161–167.

273. Greenberg MJ, Moore JR (2010) The molecular basis of frictional loads in the *in vitro* motility assay with applications to the study of the loaded mechanochemistry of molecular motors. *Cytoskeleton* 67(5):273–285.

274. Sommese RF, et al. (2013) Molecular consequences of the R453C hypertrophic cardiomyopathy mutation on human β-cardiac myosin motor function. *PNAS* 110(31):12607–12612.

275. Aksel T, Choe Yu E, Sutton S, Ruppel KM, Spudich JA (2015) Ensemble force changes that result from human cardiac myosin mutations and a small-molecule effector. *Cell Reports*. doi:10.1016/j.celrep.2015.04.006.

276. Greenberg MJ, Arpağ G, Tüzel E, Ostap EM (2016) A perspective on the role of myosins as mechanosensors. *Biophysical Journal* 110(12):2568–2576.

277. Gribbon P, Sewing A (2003) Fluorescence readouts in HTS: no gain without pain? *Drug Discovery Today* 8(22):1035–1043.

278. Gakamsky DM, Dennis RB, Smith SD (2011) Use of fluorescence lifetime technology to provide efficient protection from false hits in screening applications. *Anal Biochem* 409(1):89–97.

279. Thorne N, Auld DS, Inglese J (2010) Apparent activity in high-throughput screening: origins of compound-dependent assay interference. *Current Opinion in Chemical Biology* 14(3):315–324.

280. Moger J, Gribbon P, Sewing A, Winlove CP (2006) The application of fluorescence lifetime readouts in high-throughput screening. *J Biomol Screen* 11(7):765–772.

281. Isenberg I, Dyson RD (1969) The analysis of fluorescence decay by a method of moments. *Biophysical Journal* 9(11):1337–1350.

282. Knutson JR, Beechem JM, Brand L (1983) Simultaneous analysis of multiple fluorescence decay curves: A global approach. *Chemical Physics Letters* 102(6):501–507.

283. Beechem JM (1992) Global analysis of biochemical and biophysical data. *Numerical Computer Methods*, Methods in Enzymology., pp 37–54.

284. Jameson DM, Vetromile CM, James NG (2013) Investigations of protein–protein interactions using time-resolved fluorescence and phasors. *Methods* 59(3):278–286.

285. Dong X, Thomas DD (2014) Time-resolved FRET reveals the structural mechanism of SERCA–PLB regulation. *Biochemical and Biophysical Research Communications*. doi:10.1016/j.bbrc.2014.04.166.

286. Kast D, Espinoza-Fonseca LM, Yi C, Thomas DD (2010) Phosphorylation-induced

structural changes in smooth muscle myosin regulatory light chain. *PNAS* 107(18):8207–8212.

287. Grashoff C, et al. (2010) Measuring mechanical tension across vinculin reveals regulation of focal adhesion dynamics. *Nature* 466(7303):263–266.

288. Lebakken CS, Kang HC, Vogel KW (2007) A fluorescence lifetime–based binding assay to characterize kinase inhibitors. *J Biomol Screen* 12(6):828–841.

289. Maltman BA, et al. (2010) 9-Aminoacridine peptide derivatives as versatile reporter systems for use in fluorescence lifetime assays. *Chemical Communications* 46(37):6929.

290. Paterson MJ, et al. (2010) A fluorescence lifetime-based assay for serine and threonine kinases that is suitable for high-throughput screening. *Anal Biochem* 402(1):54–64.

291. Becker W (2012) *The BH TCSPC Handbook* (Becker & Hickl GmbH, Berlin). 5th Ed.

292. Muretta JM, et al. (2010) High-performance time-resolved fluorescence by direct waveform recording. *Review of Scientific Instruments* 81(10):103101–103108.

293. Nesmelov YE, et al. (2011) Structural kinetics of myosin by transient time-resolved FRET. *PNAS*. doi:10.1073/pnas.1012320108.

294. Cornea RL, et al. (2012) High-throughput FRET assay yields allosteric SERCA activators. *J Biomol Screen* 18(1):97–107.

295. Gruber SJ, et al. (2014) Discovery of enzyme modulators via high-throughput time-resolved FRET in living cells. *J Biomol Screen* 19(2):215–222.

296. Kleinfelder S (2003) Advanced transient waveform digitizers. *Proceedings of SPIE* 4858:316–326.

297. Isenberg I, Dyson RD, Hanson R (1973) Studies on the Analysis of Fluorescence Decay Data by the Method of Moments. *Biophysical Journal* 13(10):1090–1115.

298. Acker MG, Auld DS (2014) Considerations for the design and reporting of enzyme assays in high-throughput screening applications. *Perspectives in Science* 1(1–6):56–73.

299. Simeonov A, et al. (2008) Fluorescence spectroscopic profiling of compound

libraries. *J Med Chem* 51(8):2363–2371.

300. Pritz S, Doering K, Woelcke J, Hassiepen U (2011) Fluorescence lifetime assays: current advances and applications in drug discovery. *Expert Opin Drug Discov* 6(6):663–670.

301. Degorce F, et al. (2009) HTRF: A technology tailored for drug discovery - a review of theoretical aspects and recent applications. *Curr Chem Genomics* 3:22–32.

302. Meng F, Sachs F (2012) Orientation-based FRET sensor for real-time imaging of cellular forces. *J Cell Sci* 125(3):743–750.

303. Inglese J, et al. (2007) High-throughput screening assays for the identification of chemical probes. *Nat Chem Biol* 3(8):466–479.

304. Li W, Vacca G, Castillo M, Houston KD, Houston JP (2014) Fluorescence lifetime excitation cytometry by kinetic dithering. *Electrophoresis*. doi:10.1002/elps.201300618.

305. Chen P, Ostrow BD, Tafuri SR, Chisholm RL (1994) Targeted disruption of the *Dictyostelium* RMLC gene produces cells defective in cytokinesis and development. *J Cell Biol* 127(6):1933–1944.

306. Sarkisyan KS, et al. (2015) Green fluorescent protein with anionic tryptophan-based chromophore and long fluorescence lifetime. *Biophysical Journal* 109(2):380–389.

307. Abraham BG, et al. (2015) Fluorescent protein based FRET pairs with improved dynamic range for fluorescence lifetime measurements. *PLoS ONE* 10(8):e0134436.

308. Manstein DJ, Hunt DM (1995) Overexpression of myosin motor domains in *Dictyostelium*: screening of transformants and purification of the affinity tagged protein. *J Muscle Res Cell Motil* 16(3):325–332.

309. Prochniewicz E, Zhang Q, Janmey PA, Thomas DD (1996) Cooperativity in F-actin: Binding of gelsolin at the barbed end affects structure and dynamics of the whole filament. *Journal of Molecular Biology* 260(5):756–766.

310. Thomas DD, Carlsen WF, Stryer L (1978) Fluorescence energy transfer in the rapid-diffusion limit. *PNAS* 75(12):5746–5750.

311. Kim YC, Best RB, Mittal J (2010) Macromolecular crowding effects on protein–protein binding affinity and specificity. *The Journal of Chemical Physics* 133(20):205101.

312. Dent EW, et al. (2007) Filopodia are required for cortical neurite initiation. *Nat Cell Biol* 9(12):1347–1359.

313. Barzik M, McClain LM, Gupton SL, Gertler FB (2014) Ena/VASP regulates mDia2-initiated filopodial length, dynamics, and function. *Mol Biol Cell* 25(17):2604–2619.

314. Liu R, et al. (2008) Sisyphus, the *Drosophila* Myosin XV homolog, traffics within filopodia transporting key sensory and adhesion cargos. *Development* 135(1):53–63.

315. Aramaki S, Mayanagi K, Jin M, Aoyama K, Yasunaga T (2016) Filopodia formation by crosslinking of F-actin with fascin in two different binding manners. *Cytoskeleton* 73(7):365–374.

316. Plantard L, et al. (2010) PtdIns(3,4,5)P3 is a regulator of Myosin-X localization and filopodia formation. *J Cell Sci* 123(20):3525–3534.

317. Lu Q, Yu J, Yan J, Wei Z, Zhang M (2011) Structural basis of the myosin X PH1N-PH2-PH1C tandem as a specific and acute cellular PI(3,4,5)P3 sensor. *Mol Biol Cell* 22(22):4268–4278.

318. Kerber ML, et al. (2009) A novel form of motility in filopodia revealed by imaging Myosin-X at the single-molecule level. *Curr Biol* 19(11):967–973.

319. Kerber M (2011) The role of Myosin-X in a putative system of intrafilopodial transport. Ph.D. (The University of North Carolina at Chapel Hill, United States -- North Carolina). Available at: https://cdr.lib.unc.edu/record/uuid:41916247-5659-4b8e-9cc6-761cb88265a7 [Accessed March 3, 2016].

320. Sousa AD, Berg JS, Robertson BW, Meeker RB, Cheney RE (2006) Myo10 in brain: developmental regulation, identification of a headless isoform and dynamics in neurons. *J Cell Sci* 119(1):184–194.

321. Svitkina TM, et al. (2003) Mechanism of filopodia initiation by reorganization of a dendritic network. *J Cell Biol* 160(3):409–421.

322. Yang C, Svitkina T (2011) Filopodia initiation. *Cell Adhesion & Migration* 5(5):402–408.

323. Weck ML, Grega-Larson NE, Tyska MJ (2017) MyTH4-FERM myosins in the assembly and maintenance of actin-based protrusions. *Current Opinion in Cell Biology*. doi:10.1016/j.ceb.2016.10.002.

324. Moen RJ, Johnsrud DO, Thomas DD, Titus MA (2011) Characterization of a myosin

VII MyTH/FERM domain. *Journal of Molecular Biology* 413(1):17–23.

325. Berger CL, Thomas DD (1994) Rotational dynamics of actin-bound intermediates of the myosin adenosine triphosphatase cycle in myofibrils. *Biophys J* 67(1):250–261.

# Appendix

## John Wiley and Sons License Terms and Conditions

Nov 27, 2016

---

This Agreement between Karl J Petersen ("You") and John Wiley and Sons ("John Wiley and Sons") consists of your license details and the terms and conditions provided by John Wiley and Sons and Copyright Clearance Center.

| | |
|---|---|
| License Number | 3997160588549 |
| License date | Nov 27, 2016 |
| Licensed Content Publisher | John Wiley and Sons |
| Licensed Content Publication | Journal of Eukaryotic Microbiology |
| Licensed Content Title | The Revised Classification of Eukaryotes |
| Licensed Content Author | Sina M. Adl,Alastair G. B. Simpson,Christopher E. Lane,Julius Lukeš,David Bass,Samuel S. Bowser,Matthew W. Brown,Fabien Burki,Micah Dunthorn,Vladimir Hampl,Aaron Heiss,Mona Hoppenrath,Enrique Lara,Line le Gall,Denis H. Lynn,Hilary McManus,Edward A. D. Mitchell,Sharon E. Mozley-Stanridge,Laura W. Parfrey,Jan Pawlowski,Sonja Rueckert,Laura Shadwick,Conrad L. Schoch,Alexey Smirnov,Frederick W. Spiegel |
| Licensed Content Date | Sep 28, 2012 |
| Licensed Content Pages | 86 |
| Type of use | Dissertation/Thesis |
| Requestor type | University/Academic |
| Format | Print and electronic |
| Portion | Figure/table |

| | |
|---|---|
| Number of figures/tables | 1 |
| Original Wiley figure/table number(s) | Figure 1 |
| Will you be translating? | No |
| Title of your thesis / dissertation | Structure-Function Analysis of Motor Proteins in vivo: Insights from Conventional and Unconventional Myosins |
| Expected completion date | Dec 2016 |
| Expected size (number of pages) | 150 |
| Requestor Location | Karl J Petersen<br><br>715 University Av SE #203<br><br>MINNEAPOLIS, MN 55414<br><br>United States<br><br>Attn: Karl J Petersen |
| Publisher Tax ID | EU826007151 |
| Billing Type | Invoice |
| Billing Address | Karl J Petersen<br><br>715 University Av SE #203<br><br>MINNEAPOLIS, MN 55414<br><br>United States<br><br>Attn: Karl J Petersen |
| Total | 0.00 USD |

Terms and Conditions

## Terms and Conditions

- The materials you have requested permission to reproduce or reuse (the "Wiley Materials") are protected by copyright.

- You are hereby granted a personal, non-exclusive, non-sub licensable (on a stand-alone basis), non-transferable, worldwide, limited license to reproduce the Wiley Materials for the purpose specified in the licensing process. This license, **and any CONTENT (PDF or image file) purchased as part of your order,** is for a one-time use only and limited to any maximum distribution number specified in the license. The first instance of republication or reuse granted by this license must be completed within two years of the date of the grant of this license (although copies prepared before the end date may be distributed thereafter). The Wiley Materials shall not be used in any other manner or for any other purpose, beyond what is granted in the license. Permission is granted subject to an appropriate acknowledgement given to the author, title of the material/book/journal and the publisher. You shall also duplicate the copyright notice that appears in the Wiley publication in your use of the Wiley Material. Permission is also granted on the understanding that nowhere in the text is a previously published source acknowledged for all or part of this Wiley Material. Any third party content is expressly excluded from this permission.

- With respect to the Wiley Materials, all rights are reserved. Except as expressly granted by the terms of the license, no part of the Wiley Materials may be copied, modified, adapted (except for minor reformatting required by the new Publication), translated, reproduced, transferred or distributed, in any form or by any means, and no derivative works may be made based on the Wiley Materials without the prior permission of the respective copyright owner.**For STM Signatory Publishers clearing permission under the terms of the STM Permissions Guidelines only, the terms of the license are extended to include subsequent editions and for editions in other languages, provided such editions are for the work as a whole in situ and does not involve the separate exploitation of the permitted figures or extracts,** You may not alter, remove or suppress in any manner any copyright, trademark or other notices displayed by the Wiley Materials. You may not license, rent, sell, loan, lease, pledge, offer as security, transfer or assign the Wiley Materials on a stand-alone basis, or any of the rights granted to you hereunder to any other person.

- The Wiley Materials and all of the intellectual property rights therein shall at all times remain the exclusive property of John Wiley & Sons Inc, the Wiley Companies, or their respective licensors, and your interest therein is only that of having possession of and the right to reproduce the Wiley Materials

pursuant to Section 2 herein during the continuance of this Agreement. You agree that you own no right, title or interest in or to the Wiley Materials or any of the intellectual property rights therein. You shall have no rights hereunder other than the license as provided for above in Section 2. No right, license or interest to any trademark, trade name, service mark or other branding ("Marks") of WILEY or its licensors is granted hereunder, and you agree that you shall not assert any such right, license or interest with respect thereto

- NEITHER WILEY NOR ITS LICENSORS MAKES ANY WARRANTY OR REPRESENTATION OF ANY KIND TO YOU OR ANY THIRD PARTY, EXPRESS, IMPLIED OR STATUTORY, WITH RESPECT TO THE MATERIALS OR THE ACCURACY OF ANY INFORMATION CONTAINED IN THE MATERIALS, INCLUDING, WITHOUT LIMITATION, ANY IMPLIED WARRANTY OF MERCHANTABILITY, ACCURACY, SATISFACTORY QUALITY, FITNESS FOR A PARTICULAR PURPOSE, USABILITY, INTEGRATION OR NON-INFRINGEMENT AND ALL SUCH WARRANTIES ARE HEREBY EXCLUDED BY WILEY AND ITS LICENSORS AND WAIVED BY YOU.

- WILEY shall have the right to terminate this Agreement immediately upon breach of this Agreement by you.

- You shall indemnify, defend and hold harmless WILEY, its Licensors and their respective directors, officers, agents and employees, from and against any actual or threatened claims, demands, causes of action or proceedings arising from any breach of this Agreement by you.

- IN NO EVENT SHALL WILEY OR ITS LICENSORS BE LIABLE TO YOU OR ANY OTHER PARTY OR ANY OTHER PERSON OR ENTITY FOR ANY SPECIAL, CONSEQUENTIAL, INCIDENTAL, INDIRECT, EXEMPLARY OR PUNITIVE DAMAGES, HOWEVER CAUSED, ARISING OUT OF OR IN CONNECTION WITH THE DOWNLOADING, PROVISIONING, VIEWING OR USE OF THE MATERIALS REGARDLESS OF THE FORM OF ACTION, WHETHER FOR BREACH OF CONTRACT, BREACH OF WARRANTY, TORT, NEGLIGENCE, INFRINGEMENT OR OTHERWISE (INCLUDING, WITHOUT LIMITATION, DAMAGES BASED ON LOSS OF PROFITS, DATA, FILES, USE, BUSINESS OPPORTUNITY OR CLAIMS OF THIRD PARTIES), AND WHETHER OR NOT THE PARTY HAS BEEN ADVISED OF THE POSSIBILITY OF SUCH DAMAGES. THIS LIMITATION SHALL APPLY NOTWITHSTANDING ANY FAILURE OF ESSENTIAL PURPOSE OF ANY LIMITED REMEDY PROVIDED HEREIN.

- Should any provision of this Agreement be held by a court of competent jurisdiction to be illegal, invalid, or unenforceable, that provision shall be deemed amended to achieve as nearly as possible the same economic effect as the original provision, and the legality, validity and enforceability of the remaining provisions of this Agreement shall not be affected or impaired thereby.

- The failure of either party to enforce any term or condition of this Agreement shall not constitute a waiver of either party's right to enforce each and every term and condition of this Agreement. No breach under this agreement shall be deemed waived or excused by either party unless such waiver or consent is in writing signed by the party granting such waiver or consent. The waiver by or consent of a party to a breach of any provision of this Agreement shall not operate or be construed as a waiver of or consent to any other or subsequent breach by such other party.

- This Agreement may not be assigned (including by operation of law or otherwise) by you without WILEY's prior written consent.

- Any fee required for this permission shall be non-refundable after thirty (30) days from receipt by the CCC.

- These terms and conditions together with CCC's Billing and Payment terms and conditions (which are incorporated herein) form the entire agreement between you and WILEY concerning this licensing transaction and (in the absence of fraud) supersedes all prior agreements and representations of the parties, oral or written. This Agreement may not be amended except in writing signed by both parties. This Agreement shall be binding upon and inure to the benefit of the parties' successors, legal representatives, and authorized assigns.

- In the event of any conflict between your obligations established by these terms and conditions and those established by CCC's Billing and Payment terms and conditions, these terms and conditions shall prevail.

- WILEY expressly reserves all rights not specifically granted in the combination of (i) the license details provided by you and accepted in the course of this licensing transaction, (ii) these terms and conditions and (iii) CCC's Billing and Payment terms and conditions.

- This Agreement will be void if the Type of Use, Format, Circulation, or Requestor Type was misrepresented during the licensing process.

- This Agreement shall be governed by and construed in accordance with the laws of the State of New York, USA, without regards to such state's conflict of law rules. Any legal action, suit or proceeding arising out of or relating to these Terms and Conditions or the breach thereof shall be instituted in a court of competent jurisdiction in New York County in the State of New York in the United States of America and each party hereby consents and submits to the personal jurisdiction of such court, waives any objection to venue in such court and consents to service of process by registered or certified mail, return receipt requested, at the last known address of such party.

## WILEY OPEN ACCESS TERMS AND CONDITIONS

Wiley Publishes Open Access Articles in fully Open Access Journals and in Subscription journals offering Online Open. Although most of the fully Open Access journals publish open access articles under the terms of the Creative Commons Attribution (CC BY) License only, the subscription journals and a few of the Open Access Journals offer a choice of Creative Commons Licenses. The license type is clearly identified on the article.

### The Creative Commons Attribution License

The Creative Commons Attribution License (CC-BY) allows users to copy, distribute and transmit an article, adapt the article and make commercial use of the article. The CC-BY license permits commercial and non-

### Creative Commons Attribution Non-Commercial License

The Creative Commons Attribution Non-Commercial (CC-BY-NC)License permits use, distribution and reproduction in any medium, provided the original work is properly cited and is not used for commercial purposes.(see below)

### Creative Commons Attribution-Non-Commercial-NoDerivs License

The Creative Commons Attribution Non-Commercial-NoDerivs License (CC-BY-NC-ND) permits use, distribution and reproduction in any medium, provided the original work is properly cited, is not used for commercial purposes and no modifications or adaptations are made. (see below)

### Use by commercial "for-profit" organizations

## National Academy of Sciences

From: PNAS Permissions <PNASPermissions@nas.edu>

Sent: Monday, November 28, 2016 14:23

To: Karl Petersen

Subject: RE: request to reprint article in a thesis

Thank you for your message. Authors do not need to obtain permission for the following uses of material they have published in PNAS: (1) to use their original figures or tables in their future works; (2) to make copies of their papers for their own personal use, including classroom use, or for the personal use of colleagues, provided those copies are not for sale and are not distributed in a systematic way; (3) to include their papers as part of their dissertations; or (4) to use all or part of their articles in printed compilations of their own works.

Please cite the original PNAS article in full when re-using the material. Because this material published after 2008, a copyright note is not needed. Feel free to contact us with any additional questions you might have.

Best regards,

Kay McLaughlin for

Diane Sullenberger

Executive Editor

PNAS

# AIP Publishing LLC License Terms and Conditions

| | |
|---|---|
| License Number | 3994430236943 |
| License date | Nov 22, 2016 |
| Licensed Content Publisher | AIP Publishing LLC |
| Licensed Content Publication | Review of Scientific Instruments |
| Licensed Content Title | Fluorescence lifetime plate reader: Resolution and precision meet high-throughput |
| Licensed Content Author | Karl J. Petersen, Kurt C. Peterson, Joseph M. Muretta, et al. |
| Licensed Content Date | Nov 5, 2014 |
| Licensed Content Volume Number | 85 |
| Licensed Content Issue Number | 11 |
| Type of Use | Thesis/Dissertation |
| Requestor type | Author (original article) |
| Format | Print and electronic |
| Portion | Excerpt (> 800 words) |
| Will you be translating? | No |
| Title of your thesis / dissertation | Structure-Function Analysis of Motor Proteins in vivo: Insights from Conventional and Unconventional Myosins |
| Expected completion date | Dec 2016 |
| Estimated size (number of pages) | 150 |
| Requestor Location | Karl J Petersen<br>715 University Av SE #203<br><br>MINNEAPOLIS, MN 55414<br>United States<br>Attn: Karl J Petersen |
| Billing Type | Invoice |

| | |
|---|---|
| Billing Address | Karl J Petersen<br>715 University Av SE #203<br><br>MINNEAPOLIS, MN 55414<br>United States<br>Attn: Karl J Petersen |
| Total | 0.00 USD |

This Agreement between Karl J Petersen ("You") and AIP Publishing LLC ("AIP Publishing LLC") consists of your license details and the terms and conditions provided by AIP Publishing LLC and Copyright Clearance Center.

## Terms and Conditions

AIP Publishing LLC -- Terms and Conditions: Permissions Uses

AIP Publishing hereby grants to you the non-exclusive right and license to use and/or distribute the Material according to the use specified in your order, on a one-time basis, for the specified term, with a maximum distribution equal to the number that you have ordered. Any links or other content accompanying the Material are not the subject of this license.

1. You agree to include the following copyright and permission notice with the reproduction of the Material: "Reprinted from [FULL CITATION], with the permission of AIP Publishing." For an article, the credit line and permission notice must be printed on the first page of the article or book chapter. For photographs, covers, or tables, the notice may appear with the Material, in a footnote, or in the reference list.
2. If you have licensed reuse of a figure, photograph, cover, or table, it is your responsibility to ensure that the material is original to AIP Publishing and does not contain the copyright of another entity, and that the copyright notice of the figure, photograph, cover, or table does not indicate that it was reprinted by AIP Publishing, with permission, from another source. Under no circumstances does AIP Publishing purport or intend to grant permission to reuse material to which it does not hold appropriate rights.

You may not alter or modify the Material in any manner. You may translate the Material into another language only if you have licensed translation rights. You may not use the Material for promotional purposes.

3. The foregoing license shall not take effect unless and until AIP Publishing or its agent, Copyright Clearance Center, receives the Payment in accordance with Copyright Clearance Center Billing and Payment Terms and Conditions, which are incorporated herein by reference.
4. AIP Publishing or Copyright Clearance Center may, within two business days of granting this license, revoke the license for any reason whatsoever, with a full refund payable to you. Should you violate the terms of this license at any time, AIP Publishing, or Copyright Clearance Center may revoke the license with no refund to you. Notice of such revocation will be made using the contact information provided by you. Failure to receive such notice will not nullify the revocation.
5. AIP Publishing makes no representations or warranties with respect to the Material. You agree to indemnify and hold harmless AIP Publishing, and their officers, directors, employees or agents from and against any and all claims arising out of your use of the Material other than as specifically authorized herein.
6. The permission granted herein is personal to you and is not transferable or assignable without the prior written permission of AIP Publishing. This license may not be amended except in a writing signed by the party to be charged.
7. If purchase orders, acknowledgments or check endorsements are issued on any forms containing terms and conditions which are inconsistent with these provisions, such inconsistent terms and conditions shall be of no force and effect. This document, including the CCC Billing and Payment Terms and Conditions, shall be the entire agreement between the parties relating to the subject matter hereof.

This Agreement shall be governed by and construed in accordance with the laws of the State of New York. Both parties hereby submit to the jurisdiction of the courts of New York County for purposes of resolving any disputes that may arise hereunder.